Series in BioEngineering

Gaetano Valenza
Enzo Pasquale Scilingo

Autonomic Nervous System Dynamics for Mood and Emotional-State Recognition

Significant Advances in Data Acquisition, Signal Processing and Classification

Springer

Series in BioEngineering

For further volumes:
www.springer.com/series/10358

Gaetano Valenza • Enzo Pasquale Scilingo

Autonomic Nervous System Dynamics for Mood and Emotional-State Recognition

Significant Advances in Data Acquisition, Signal Processing and Classification

Springer

Gaetano Valenza
Bioengineering and Robotics Research Center "E. Piaggio"
University of Pisa
Pisa, Italy

Enzo Pasquale Scilingo
Bioengineering and Robotics Research Center "E. Piaggio"
University of Pisa
Pisa, Italy

ISSN 2196-8861
ISSN 2196-887X (electronic)
Series in BioEngineering
ISBN 978-3-319-02638-1
ISBN 978-3-319-02639-8 (eBook)
DOI 10.1007/978-3-319-02639-8
Springer Cham Heidelberg New York Dordrecht London

Library of Congress Control Number: 2013951995

Printed on acid-free paper

Springer is part of Springer Science+Business Media (www.springer.com)

Dedicated to my beloved parents, Francesco and Carmen
G.V.

Dedicated to my loves, Laura and Emma
E.P.S.

Foreword

This book fervently presents a wide collection of methodological and applicative studies related to the assessment of autonomic nervous system (ANS) dynamics in healthy subjects and patients with mood disorders. Indeed, the high technical content makes the book quite attractive to anyone interested in mathematics, applied physics, electronics, statistics and, most especially, in signal processing.

Firstly, the authors amply review and discuss every aspect that concerns emotions and mood recognition, emphasizing experimental set-up, procedures, and interpretation of the results, and allowing physicians and clinical psychologists to take full advantage of this monograph. Secondly, I am glad that the book emphasizes the probabilistic approach based on point-process models, which I have been studying in-depth during the last decade, in order to instantaneously assess ANS linear and nonlinear dynamics. Here the authors present a novel extension of the point process mathematical framework as characterized through analysis of heartbeat series, thus providing a wide range of novel ANS markers that can be used for modeling and classification. Remarkably, the book is also a unique contribution to the study of ANS nonlinear dynamics. Thirdly, although the emphasis of this work is on advanced signal processing techniques, it contains critical points regarding the development of wearable systems for ANS monitoring. I like the authors' philosophy to "sensorize" everyday clothes such as gloves, t-shirts, and hats to make the recording process as non-invasive, effective and comfortable as possible.

I know the authors personally and I did not expect anything less from this book. I think that they can be confident that there will be many grateful readers who will have gained a broader perspective how the study of ANS dynamics can be integrated within the fields of biomedical engineering for affective computing and psychophysiology. I do recommend the book for the active research scientists and PhD students interested in such interdisciplinary approaches.

Harvard Medical School
Boston, MA, USA
August 2013

Riccardo Barbieri

Preface

The book reports on recent advances in studying autonomic nervous system (ANS) dynamics for the assessment of mood and emotional states. We will illustrate several concepts, some of which are currently sparse over different manuscripts, in order to bring out a clear breakthrough in the field of affective computing, mood assessment, biomedical engineering, biomedical signal processing, and data acquisition. The aim is to describe some personalized methodologies able to characterize the affective state of a subject by means of the analysis of a wide spectrum of peripheral biosignals such as Heart Rate Variability, Electrodermal Response, Respiration Activity, Eye gaze information.

These methodologies will be presented with applications on actual data gathered from healthy subjects as well as patients affected by mood disorders, although the reported advances can also be applied to several other (clinical) fields. Starting form a psychological description of how-to-elicit an emotion (including models of emotions, affective stimuli etc.), concepts will move to the neuro-physiology of emotions, explaining the physiological bases of emotion recognition through non-invasive monitoring of the ANS. Afterwards, advanced methodologies of biomedical signal processing will be thoroughly described pointing out the crucial role of ANS nonlinear dynamics. Then, the book will emphasize a probabilistic framework based on point-processes able to instantaneously assess the ANS control on the linear and the nonlinear cardiovascular dynamics. Concerning the signal acquisition, novel wearable monitoring systems will be described in further sections along with experimental procedures on healthy subjects and patients with bipolar disorders. The high technical content and all the proposed pioneering approaches make this monograph of large interest. Several professionals such as biomedical engineers as well as physiologists, neuroscientists, etc. could benefit from the content of this book.

Pisa, Italy
August 2013

Gaetano Valenza
Enzo Pasquale Scilingo

Acknowledgements

We would like to acknowledge all the people who contributed to data acquisition and analysis. In particular, we would like to express our deepest and sincere gratitude to Dr. Antonio Lanatá, Dr. Riccardo Barbieri, Dr. Luca Citi, Dr. Rita Paradiso, Dr. Paolo Allegrini, Prof. Danilo De Rossi, Dr. Claudio Gentili, and Prof. Dr. Gilles Bertschy.

Contents

Acronyms

AIC	Akaike Information Criterion
ANS	Autonomic Nervous System
ApEn	Approximate Entropy
AR	Auto-Regressive
AUC	Area Under the Curve
BRS	Baroreflex Sensitivity
CI	Confidence Interval
CMA	Circumplex Model of Affect
CNS	Central Nervous System
CR	Cardio-Respiratory
CRS	Cardio-Respiratory Synchrogram
CV	Clustering/Voting
DCT	Discrete Cosine Transform
DFA	Detrended Fluctuation Analysis
DLE	Dominant Lyapunov Exponent
DMMRSP	Difference between Maximum and Minimum of the RSP signal
ECG	Electrocardiogram
EDR	ElectroDermal Response
EEG	ElectroEncephaloGram
EGT	Eye Gaze Tracker
FIR	Finite Impulse Response
k-NN	k-Nearest Neighborhood
KS	Kolmogorov–Smirnov
HATCAM	Head-mounted eye tracking system
HF	High Frequency
HH	High Frequency–High Frequency
HOS	High Order Spectra
HR	Heart Rate
HRV	Heart Rate Variability
IADS	International Affective Digital Sounds system
IAPS	International Affective Picture System

IG	Inverse-Gaussian
IMS	Bauer internal mood scale
IRF	Impulse Response Function
IRF	Infrared
LF	Low Frequency
LL	Low Frequency–Low Frequency
LH	Low Frequency–High Frequency
LSq	Least Square
NN	Normal-to-Normal
MAF	Moving Average Filter
MAR	Movement Artifact Removal
MAXRSP	Maximum of the RSP signal
MBI	Mean of Bispectral Invariants
MDNV	Mean of Derivative for Negative Values of the EDR signal
MFD	Mean of the First Derivative of the RSP signal
MINRSP	Minimum of the RSP signal
MLP	Multi-Layer Perceptron
MMB	Mean Magnitude of the Bispectrum
MNN	Mean value of the NN intervals
MSE	Multiscale Entropy
MSD	Mean of the Second Derivative of the RSP signal
NAR	Nonlinear Autoregressive
NARI	Nonlinear Autoregressive Integrative
NBE	Normalized Bispectral Entropy
NBSE	Normalized Bispectral Squared Entropy
PEB	Phase Entropy of the Bispectrum
PCA	Principal Component Analysis
PHQ	Patient Health Questionnaire
pNN50	Probability of the successive differences of intervals which differ by more than 50 ms
PNSDAS	Proportion of Negative Samples in the Derivative vs All Samples of the EDR signal
POMS	Profile of Mood States
PSD	Power Spectral Density
PSYCHE	Personalized monitoring SYstems for Care in mental HEalth
QDC	Quadratic Discriminant Classifier
QIDS	Quick Inventory of Depressive Symptomatology
RMSSD	Root Mean Square of Successive Differences of intervals
ROI	Region Of Interest
RP	Recurrence Plot
RQA	Recurrence Quantification Analysis
RSA	Respiratory Sinus Arrhythmia
RSP	ReSPiration activity
RSPR	ReSPiration Rate
SampEn	Sample Entropy

SCL	Skin Conductance Level
SCR	Skin Conductance Response
SDBA	Standard Deviation of the Breathing Amplitude
SDFD	Standard Deviation of the First Derivative of the RSP signal
SDNN	Standard Deviation of the NN intervals
SDSD	Standard Deviation of the Second Derivative of the RSP signal
SDNN	Standard Deviation of the NN intervals
SEM	Standard Error of the Mean
SNR	Signal-to-Noise-Ratio
SVM	Support Vector Machine
TAT	Thematic Apperception Test
TINN	Triangular Index of the NN intervals
USART	Universal Synchronous Asynchronous Receiver Transmitter
VBI	Variance of Bispectral Invariants
VLF	Very Low Frequency
YMS	Young Mania Scale

Part I
Introductory Remarks and State of the Art

This first part of the book is going to emphasize some introductory remarks and describe the current state of the art related to the study of autonomic nervous system (ANS) dynamics for mood and emotional-state recognition. Mood assessment is intended as long-lasting state and is performed monitoring patients with mental disorders such as bipolar disorders. Several pragmatic issues such as emotional and mood state modeling and elicitation will be pointed out introducing also physiological and mathematical motivations to the study of ANS nonlinear dynamics.

Chapter 1
Introduction to Advances in Autonomic Nervous System Dynamics for Mood and Emotional-State Recognition

Emotions are important psychological conditions that reflect several human states, such as pleasant or unpleasant feelings, human relationships, process and results of action. They are present in all mental processes, and any human activity (even psycho-pathological) is accompanied by emotional experiences. Many research works have shown that emotional processing can have primacy over cognition [1]. The famous naturalist Darwin stated that emotions emerged in the course of evolution as the means by which living creatures determine the significance of certain conditions to meet their urgent needs [2]. They are the most important factors in the regulation of cognition. In addition, several works have shown how emotion regulation is an essential feature of mental health. In particular, it has been highlighted how emotion and its regulation have an important role in various aspects of normal functioning. For example, as it will be pointed-out later, emotions become dys-regulated in major depressive episodes, and some theoretical views of depression are based on emotion changes which have implications in assessment, treatment, and prevention of the pathology [3]. Moreover, it has been shown that a strong relationship exists between emotion and anxiety [4] as well as brain damages of emotional processing areas and decision-making process [5].

Changes in emotional states often reflect facial, vocal, and gestural modifications in order to communicate, sometimes unconsciously, personal feelings to other people. Such changes can be generalized across cultures, e.g. nonverbal emotional, or can be culture-specific [6].

The automatic *emotion recognition* is one of the most important applications in neuroscience and, often, is identified within the so-called *affective computing* field. Mainly, such a technical field refers to the engineering approaches able to link physiological patterns to different emotions. Recently, a review on affective computing was written by Calvo et al. [7] and reports on emotion theories as well as on affect detection systems using physiological and speech signals (also reviewed in [8]), face expression and movement analysis. Since alteration of mood strongly affects the normal emotional process, emotion recognition is also an ambitious objective in the field of mood disorder psychopathology.

G. Valenza, E.P. Scilingo, *Autonomic Nervous System Dynamics for Mood and Emotional-State Recognition*, Series in BioEngineering,
DOI 10.1007/978-3-319-02639-8_1,

In the last decade, several efforts have been spent to obtain a reliable methodology to automatically identify the emotional/mood state of a subject, starting from the analysis of facial expressions, behavioral correlates, and physiological signals. Several computational methods for emotion recognition based on variables associated with the Central Nervous System (CNS), e.g. the Electroencephalogram (EEG), have been recently proposed [9–15]. These methods are justified by the fact that human emotions originate in the cerebral cortex involving several areas for their regulation and feeling. The prefrontal cortex and amygdala, in fact, represent the core of two specific pathways. Affective elicitations longer than 6 seconds allow the prefrontal cortex to modulate bottom up inputs and produce appropriate cognitive responses [16]. Stimuli briefly presented access the fast route of emotion recognition via the amygdala. Of note, it has been found that also the visual cortex is involved in emotional reactions to different classes of stimuli [17]. Dysfunctions on these CNS recruitment circuits lead to pathological effects [18–20] such as anhedonia, i.e. the loss of pleasure or interest in previously rewarding stimuli, which is a core feature of major depression and other serious mood disorders.

A wider class of affective computing studies are related to changes of the Autonomic Nervous System (ANS) activity as elicited by a specific emotional state. Monitoring physiological variables linked to ANS activity, in fact, can be easily performed through wearable systems, e.g. sensorized t-shirts [21] or gloves [22, 23]. Moreover, ANS dynamics is thought to be less sensitive to artifacts than EEG. In addition, the human vagus nerve is anatomically linked to the cranial nerves that regulate social engagement via facial expression and vocalization. Experimental evidences over the past two decades show that respiration activity (RSP), electrodermal response (EDR), and especially Heart Rate Variability (HRV) analysis, in both the time and frequency domain, can provide a unique, noninvasive assessment of autonomic functions [24, 25] and cardiobvascular dynamics [26–28]. Given such evidences,

this book aims at performing a breakthrough investigation on methodological and theoretical aspects of ANS signals as source of reliable and effective markers for mood state recognition and assessment of emotional responses.

Motivations and Impacts Primary impacts of this book are in the field of affective computing and all those applications that use emotion recognition systems. The methodology and the rationale behind the reported studies, in fact, are able to assess the personal cognitive association to positive and negative emotions with very satisfactory results.

From a physiological perspective, this book confirms the inherent non-linearties of the autonomic and cardiovascular systems (e.g. the nonlinear neural signaling on the sinoatrial node [29]) through several experimental results in both healthy subjects and patients.

Major achievements have impacts also in mood disorders psycho-pathology diagnosis and treatment. Since mood disorders produce an altered emotional response,

the innovative wearable monitoring systems and the methodologies applied along could make a continuous evaluation of possible disorders.

Moreover, advances methodologies based on stochastic point-process model was devised for the instantaneous assessment of the cardiovascular system extracting a novel set of dynamic signatures, based on the dynamical spectrum, bispectrum and trispectrum, able to characterize the wide range of cardiovascular responses under different physiological conditions [30]. Therefore, such novel instantaneous nonlinear features could provide better assessment and improved reliability of other different kinds of physiological responses and pathologies.

Book Contributions and Perspectives In this book, the overall input-output ANS response is first presented in order to implement an effective automatic emotion recognition system [31]. For this purpose, biosignals such as HRV and RSP, and EDR contribute to the assessment. Emotions are elicited in agreement with a bi-dimensional spatial localization of affective states, i.e. arousal and valence dimensions. Specifically, thirty-five healthy volunteers underwent a passive emotional elicitation protocol through the presentation of a set of emotional pictures gathered from the International Affective Picture System (IAPS), categorized in 5 levels of arousal and 5 levels of valence, including the neutral one. This outcome allows allocating 25 different affective regions in the arousal-valence space, known as Circumplex Model of Affect (CMA). Commonly-used monovariate analyses are applied in order to extract features from standard and from nonlinear methods of analysis. The arousal and valence multiclass recognition are performed by processing the extracted feature sets through a Bayesian decision theory based classifier which uses a Quadratic Discriminant Classifier (QDC). The comparative analysis shows that the use of nonlinear system-derived approaches gives pivotal quantitative markers to evaluate the dynamics and predicability of ANS changes. Specifically, when nonlinearly extracted features are embedded in the mentioned affective computing system along with the linearly derived ones, the percentages of successful recognition dramatically increases (accuracy $> 90\%$ for both arousal and valence classes) [31]. These findings simply confirm the important role played by nonlinear and non-stationary dynamics in many physiological processes [32]. This behavior, in fact, can be the result of a nonlinear frequency modulation or multi-feedback interactions among the involved biological processes. For instance, on the human cardiovascular system, a nonlinear frequency modulation of the heart primary pacemaker (sino-atrial node) through ANS signaling [33] and hormonal control [29] has been demonstrated.

These interactions can carry out several coupling mechanisms such as biofeedback for system regulation and synchronizations such as the respiratory sinus arrhythmia (RSA) [34] and baroreflex sensitivity (BRS) [35]. Accordingly, the phase synchronization between breathing patterns and heart rate is investigated during the mentioned IAPS passive affective elicitation [36]. Results demonstrate that respiratory and cardiac systems adapt their rhythms in response to an external emotional stimulation. In particular, when a strong affective event occurs, the Cardio-Respiratory (CR) system becomes more synchronized (reasonably due to

the sympathetic and parasympathetic signaling activity). The phase synchronization is quantified by applying a bivariate analysis relying on the concept of phase synchronization of chaotic oscillators, i.e. the Cardio-Respiratory Synchrogram (CRS) [37]. This technique allows for the estimation of the synchronization ratio $m : n$ as the attendance of n heartbeats in each m respiratory cycles. A clearly increased synchronization is observed during the presentation of images with significant arousal content with respect to the neutral ones while no statistical difference has been found among sessions with slightly different arousal content. Accordingly, the arousal affective stimulation increases the coupling between the two considered systems [36].

Moreover, using the same data gathered from healthy subjects, another all-inclusive methodology able to robustly discern the elicited 5 levels of arousal and 5 levels of valence, including a neutral state is proposed. According to the mentioned previous findings [31, 36], the crucial roles of monovariate and bivariate measures of ANS-signs such as HRV, RSP and EDR were jointed in order to obtain a more effective and reliable emotion recognition system [38].

Moreover, in order to find theoretical foundations of emotional elicitation and to bring benefits to other model-based emotion recognition systems, a model of CR coupling during sympathetic elicitation using a theoretical nonlinear model has been developed [38]. Note that this model is a simple adaptation of the theories of weakly coupled oscillators [39–41] with external driving. The CR synchronization was already studied under anesthesia [42, 43], exercise [44] or aging [45], where particular emphasis was pointed out for the occurrences of transitions between synchronization regimes. Therefore, the theoretical idea behind the proposed model is that the CR system is comprised of weakly coupled self-sustained oscillators that, when exposed to an external perturbation (i.e., sympathetic activation), becomes synchronized and less sensible to input variations. This hypothesis is experimentally proved by other findings relating the Dominant Lyapunov Exponent and the Approximate Entropy [46] to nonlinear dynamics of the HRV, showing a clear switching mechanism between regular and complex dynamics when switching from neutral to arousal elicitation.

Despite the great achievements and novelty of the hereby proposed emotion recognition systems, such methods require relatively long-time series of multivariate records (tens of seconds or minutes). Reducing such a dimensionality would bring beneficial results to both computational and operational equipment costs. Moreover, they are unable to provide accurate characterizations in short-time series (less than 10 seconds of image presentation) and to track very fast stimulus-response changes. To overcome these limitations, a novel personalized probabilistic framework able to characterize the emotional state of a subject through the analysis and modeling of heartbeat dynamics is also proposed. Due to the intrinsic nonlinearity and non-stationarity of the RR interval series detected from the Electrocardiogram (ECG), a specific point-process nonlinear autoregressive model is devised for such an instantaneous identification [47]. Features from the instantaneous spectrum and bispectrum of the equivalent nonlinear input-output model were extracted and given as input to a classification algorithm. By taking advantage of the standard subdivision in low frequency and high frequency ranges of HRV in the bispectral domain, this

method introduces novel nonlinear indices of heartbeat dynamics directly related to higher order interactions between faster (vagal) and slower (sympatho-vagal) heartbeat variations, thus offering a new perspectives into more complex autonomic dynamics. Results on the short-time emotion recognition reported first-rate correct identification of personal predefined levels of arousal, valence and self-emotional state, with recognition accuracies as high as 90%. Remarkably, this approach represents the first achievement for an instantaneous and personalized assessment of short-term emotional responses, achieved by using only heartbeat dynamics. Focusing on the pure mathematical formulation, model improvements in terms of goodness-of-fit and feature estimation are given by the use of the Laguerre expansion of the input-output Volterra kernels [47–53].

The clinical applicative scenario concerns patients suffering from *bipolar disorders* [54–56]. Such patients are characterized by a series of both depressive and maniacal or hypo-maniacal episodes. Although common and expensive to treat, the clinical assessment of bipolar disorder is still ill-defined.

Since the current literature reports on several correlations between mood disorders and dysfunctions involving the ANS, one objective was to develop a novel and reliable mood recognition system based on a pervasive, wearable and personalized monitoring system using ANS-related biosignals. The ANS monitoring platform used in this study is the core sensing developed in the frame of a European project PSYCHE (Personalized monitoring systems for care in mental health) [54]. It is comprised of a comfortable sensorized t-shirt that can acquire the inter-beat interval time series, the heart rate, and the respiratory dynamics. Two main experimental protocols are presented in order to study ANS changes in bipolar patients: a long-term monitoring during the day through the night, and a short-term monitoring including an affective elicitation. In the latter case, the EDR was acquired along [55]. In both cases, bipolar patients were followed for a period of 90 days during which up to six monitoring sessions and psychophysical evaluations were performed for each patient. Specific signal processing techniques and artificial intelligence algorithms were applied to analyze more than 120 hours of data. Concerning the long-term analysis, a classification accuracy of about 97% was achieved for the intra-subject analysis. Such an accuracy was found in distinguishing relatively good affective balance state (euthymia) from severe clinical states (severe depression and mixed state) and is lower in distinguishing euthymia from the milder states (accuracy up to 88%). Concerning the short-term study, very satisfactory results were obtained also for the inter-subject analysis. In this case, distinguished performances are reported for the analysis of EDR (using EDR deconvolutive analysis) and HRV (using nonlinear point-process models) [57]. Therefore, evidences about the correlation between mood disorders and ANS dysfunctions were found and the obtained results are promising for an effective biosignal-based mood recognition [54–57].

In this book,

> besides signal processing methods and computational models, achievements related to the hardware development of novel wearable systems for ANS monitoring are reported as well.

Mainly, they are related to a textile-based fabric glove able to acquire the EDR [22, 23] and an Eye Gaze Tracker (EGT) able to acquire also the pupil size variation [58, 59]. More specifically, the glove [22, 23] is endowed with integrated textile electrodes placed at the fingertips and was successful applied to discriminate affective states. The textile electrodes were characterized in terms of voltage-current characteristics and trans-surface electric impedance [22, 60]. Moreover, signal quality of EDRs acquired simultaneously from textile and standard electrodes was comparatively evaluated. The EGT system proposed, HATCAM, is a new wearable and wireless eye tracking system comprised of only one lightweight camera able to capture, by means of a mirror, the eyes of the subject and the scene in front of him, simultaneously. The proposed wearable and wireless EGT is able to robustly enable eye tracking and pupil area detection. HATCAM is used to investigate whether the eye tracking and pupil size variation can provide useful cues to discriminate emotional states induced by viewing images at different arousal content [58, 59].

Chapter 2
Emotions and Mood States: Modeling, Elicitation, and Classification

Common experience suggests that emotions cannot be reduced to single word definitions. Researchers exploring the subjective experience of emotions have pointed out that emotions are highly intercorrelated both within and between the subjects reporting them [61, 62]. For example, subjects rarely describe feeling a specific positive emotion without also claiming to feel other positive emotions [63]. This high variability in expression and definition of emotions implies that the development of an automatic emotion recognition system is a very challenging task.

In this chapter, three crucial issues are addressed: modeling, elicitation and classification of emotions. Moreover, the role of the Autonomic Nervous System (ANS) patterns is emphasized along with the related nonlinear dynamics.

2.1 Modeling Emotions

In the literature, several approaches for modeling emotions have been proposed. Discrete, dimensional, appraisal, and dynamical models are the most interesting, and in addition, they are not exclusive from each other.

In *discrete models*, emotions can be seen as the result of a selective adaptation that ensures survival [64]. This survival concept could be illustrated by the following relation: danger $\Rightarrow$ fear $\Rightarrow$ escape $\Rightarrow$ survival. The result of this selection is a small set of basic, innate and universal emotions. For instance, Ekman proposed 6 basic emotions which are identified on the basis of facial expressions: anger, disgust, fear, joy, sadness and surprise [65, 66]. Besides, in the literature other discrete models have been proposed which include more or less basic emotions, usually from 2 to 10 ([67–69]). These emotions are called primary emotions as opposed to secondary emotions which result from a combination of the primary ones (e.g. contempt = anger + disgust). Nevertheless, this model can be insufficient to describe mixed emotions which necessarily require much more than one word to be expressed, and in addition there are some controversies in the assumption of universality of basic emotions (Darwinian hypothesis [64]). What seems true is that emotions are universally expressed (e.g. facial expressions [70]) but dependent on semantic attributions.

G. Valenza, E.P. Scilingo, *Autonomic Nervous System Dynamics for Mood and Emotional-State Recognition*, Series in BioEngineering,
DOI 10.1007/978-3-319-02639-8_2,

It shows that inter-cultural differences, e.g. difference between Asian and occidental people, are more important than intra-cultural differences, e.g. between genders, and that no significant differences between primary and secondary emotions exist. From an evolutionary point of view, basic emotions may be the first emotions infants could experience [71]. See Ortony et al. [72], for basic emotion categories defined over the years.

Unlike discrete models, *dimensional models* consider a continuous multidimensional space where each dimension stands for a fundamental property common to all emotions. This kind of model has already been used by Wilhelm Wundt [73]. Over the years, a large number of dimensions has been proposed [74–79]. Two of the most accepted dimensions were described by Russel [80]: valence (i.e. pleasure, positive versus negative affect), and arousal (low versus high level of activation). These dimensions were derived from a valence, arousal, and dominance space developed by Russell and Mehrabian [81], in which dominance represents the degree of control over the emotion.

Appraisal models are based on the evaluation of current, remembered or imagined circumstances. At the heart of appraisal theory is the idea that the particular judgments made about the environment and ourselves causes different emotions. The situational appraisals appear to be highly dependent on motives and goals. In other words, how we feel depends on what is important to us, indeed all our appraisals are connected to what we want and, therefore, to how we feel. For example, frustration results from a goal which is not achieved. This model was introduced by Arnold [82] and has been developed and refined by Frijda [83], Ortony et al. by developing the OCC model [84], Scherer with the Component Process Theory [85] and the derived one by Lisetti and Gmytrasiewicz [86]. The appraisal process can be thought of having a continuous as well as a categorical nature. Roseman's (1996) model shows that appraisal information can vary continuously but categorical boundaries determine which emotion will occur. To solve the problem between categorical and continuous appraisal order, it may be a good idea to place discrete emotional categories (i.e. happiness, sadness, etc.) while continuous models represent the varieties, styles, and levels of these already defined distinct emotions [87].

Finally, the *dynamical model* approach considers emotions as a dynamical process. This model starts from an evolutionary perspective and characterizes emotion in terms of response tendencies. In the dynamics perspective emotion is a regulable system and the capability of understanding its rules is essential. According to a process model of emotion regulation, emotion may be regulated at five points in the emotion generative process: selection of the situation, modification of the situation, deployment of attention, change of cognitions, and modulation of responses. It may be useful to take into account concepts like mood and personality (see Egges et al. for an implemented model [88]).

In all the studies presented in this book, a common dimensional model which uses multiple dimensions to categorize emotions, the Circumplex Model of Affects (CMA) [89] is adopted. This model interprets emotional mechanisms underlying affects as a continuum of highly interrelated and often ambiguous states. They are distributed on a Cartesian system of axes; each axis represents a neurophysiological

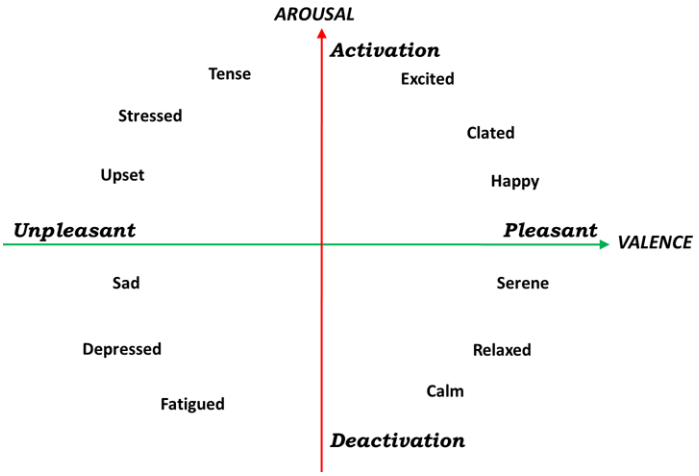

Fig. 2.1 A graphical representation of the circumplex model of affect with the *horizontal axis* representing the valence dimension and the *vertical axis* representing the arousal or activation dimension (adapted from [31])

pathway by which emotion is being processed. In many cases, by using factor analysis and multidimensional scaling of a wide set of psychometric assessments and self-reports on emotional states, it is possible to use a more simplified bi-dimensional model. In particular, in the CMA used in the reported experiments the two dimensions are conceptualized by the terms of valence and arousal, which can be intended as the two independent, predominantly subcortical systems that underlie emotions (see Fig. 2.1). Valence represents how much an emotion is felt by people as positive or negative. For example, someone feeling sad has evaluated surrounding events as very negative. On the contrary, someone feeling joy would have appraised the environment as positive for his well being. Arousal indicates how relevant the surrounding events are and therefore how strong the emotion is. In this case, someone feeling excited will have an emotion represented by a bigger arousal and someone feeling bored will experience a much less relevant emotion. Accordingly, in CMA, arousal and valence can be considered adequate parameters to identify specific emotions. This simplified model addresses most of the methodological issues raised by experimental studies on emotions and provides a reliable means for comparing outcomes.

2.2 Autonomic Nervous System Correlates of Emotions

The idea behind this book is that ANS (nonlinear) dynamics reflects measurable changes according to the emotional experience [89, 90].

Many researchers have observed that peripheral physiological responses to affective stimuli vary incrementally with subjective ratings of valence and arousal. As a matter of fact, several physiological ANS signs, e.g. Heart Rate Variability (HRV), Respiration (RSP), Electrodermal Response (EDR), pupil size and eye movement variation) correlates with subject behavior or emotional status [91–94]. Nevertheless, the correlation between emotions and physiological reactions controlled by the ANS are complex. Anger, for example, has been associated with higher heart rate than happiness, and on the other hand, has been associated with higher finger temperature than fear [95, 96].

2.2.1 Heart Rate Variability

One of the most important ANS-related marker is the HRV. It refers to the variations in the beat-to-beat intervals or correspondingly in the instantaneous heart rate (HR). HRV reflects the regulation mechanism of the cardiac activity by the ANS [97]. Over the last 20 years, several studies have demonstrated the significant relationship between ANS and HRV, especially by means of frequency domain indexes, e.g. LF/HF ratio [98]. Since the human cardiovascular system is intrinsically nonlinear, methods for studying dynamic systems have been adopted to quantify HRV and find nonlinear fluctuations in the HR, that are otherwise not apparent. Although a detailed physiological explanation behind these complex dynamics has not been completely clarified, several nonlinearity measures of HRV have been used as important quantifiers of the complexity of cardiovascular control in healthy and impaired subjects [99–101]. Some nonlinear methods used for studying the HRV include Lyapunov exponents [102], $1/f$ slope [103], approximate entropy (ApEn) [104], Detrended Fluctuation Analysis (DFA) [105], Recurrence Plot (RP) [106, 107], and entropy analysis [108]. As reported in [109], HRV of sinus rhythm is characterized by being a chaos-like determinism, with at least a positive Dominant Lyapunov Exponent (DLE) and $1/f$-like broad-band spectrum with an exponent of approximately -1. Moreover, HRV chaos-like determinism is modulated but not eliminated by the inhibition of the autonomic tone or by exercise.

2.2.2 The Electrodermal Response

Electrodermal Responses (EDR) has been shown to be a powerful emotion-related signal [110]. EDR represents changes in the skin electrical properties, i.e. electric impedance, due to psychologically-induced sweat gland activity [111] upon an external stimulus. More specifically, it is strictly related to the activity of the eccrine sweat glands (located in the palms of the hands and soles of the feet) and the skin pore size. In a variety of induction contexts, electrodermal reactivity consistently varies with emotional intensity, with largest responses elicited in either unpleasant and pleasant contexts with high rate of arousal. Many studies, for example, have

found that skin conductance increases when people view pictures rated as emotional, compared to neutral, regardless of whether they are rated pleasant or unpleasant [111–113]. Moreover, when listening to affective sounds [114], or music [115], skin conductance activity increases as the acoustic stimuli are highly rated in emotional arousal. Demonstrating consistent modulation by affective intensity across perceptual contexts, elevated electrodermal reactions are also found when people view film clips that are either unpleasant or pleasant [116]. The scientific community has accepted to consider the EDR as indirect indicator of the sympathetic nervous system [110]. Several approaches are used to measure this signal (e.g. [117]).

In this work, a small continuous voltage is applied to the skin and the induced current is measured through two electrodes positioned at the index and middle fingertips of the non-dominant hand. The ratio between voltage drop and induced current represents the skin electric impedance. EDR changes depend on the individual physiological state as well as on interaction with environmental events. Using a continuous voltage as source, the EDR can be referred to as Skin Conductance (SC). SC can be split into two components: tonic and phasic. Tonic component is the baseline level of skin conductance (also called skin conductance level-SCL), whose trend is different from person to person and depends on both patient physiological state and autonomic regulation. Phasic component (also called Skin Conductance Responses—SCRs), superimposed on the tonic baseline level, changes with specific external stimuli such as lights, sounds, smells, etc. or events.

This book also focus on identifying emotional cues, due to arousal elicitation, in EDR measurements by using a textile-based sensing glove. The use of a wearable textile system exhibits several advantages in terms of portability and usability for long-term monitoring, and gives minimal constraints. Therefore, this kind of system broadens scientific horizons which autonomic regulation investigation is currently based on, providing high acceptability and usability in daily activities.

2.2.3 Information Coming from the Eyes: Pupil Size Variation and Eye Tracking

Eye movements can provide an estimation of what information an individual is considering. Eye tracking is becoming an increasing popular measurement of cognitive information processing [118]. The most recent eye-tracking technology development (e.g. ease of use, improved accuracy, and enhanced sampling rate) also offers the possibility for unobtrusive monitoring in the field of emotions because no sensors need to be attached to the user. By gathering and analyzing data on where and how long eyes are looking, a lot of information about the cognitive and emotional structure could be inferred. Eye tracking allows estimating cognitive or affective states exploiting the property of the immediacy (people process information as it is seen) and the eye-mind (the eye remains fixated upon an object while the object is being processed). Concerning eye-tracking methods, two popular methods are currently used:

1. shining a light on the eye and detecting corneal reflection
2. simply taking visual images of the eye and then locating the dark pupil area.

Generally, the choice of the best method depends upon the external lighting conditions. To compute where a person is fixating, the eye-tracking apparatus can be placed on the person head along with a camera so that a visual image is captured showing what the person is currently looking at, with a point on the image indicating the object being fixated. Pupil dilations and constrictions are also governed by the ANS [119]. Previous studies have suggested that pupil size variation is related to both cognitive and affective information processing. As a matter of fact, it has been pointed how the eye tracking information plays a crucial role on emotional processing related to visual stimuli [120, 121]. Moreover, some works reported on how eye tracking information can be related to selective attention to emotional pictorial stimuli [122]. They found out that preferential attention depends on the affective valence of visual stimuli, i.e. pleasant and unpleasant pictures.

Concerning information provided by the pupil, previous studies suggested that pupil size variation is related to both cognitive and affective information processing [58, 123]. More specifically, [124] pointed out that during cognitive tasks such as recalling something from memory the pupils dilate and return to previous size within a few seconds of completing the mental work. However, previous works on affective elicitation and pupil size variation have been somewhat controversial. Dated research activity of [125] studied the effects of various sensory and psychological stimuli to pupil size variation and argued that none of them caused pupil constriction except for increased light intensity. On the contrary, [126] found out that there would be a continuum ranging from extreme dilation due to interesting or pleasing stimuli to extreme constriction due to unpleasant or distasteful content. Almost in the same years, [127] contradicted this bi-directional view arguing that there is no pupil constriction in response to negative stimuli, or it can be limited to a few individuals and a small range of stimuli. He proposed that pupil size should be linearly related to the stimulation intensity. From this point of view, pupil size variation seems to be sensitive to the valence scale, resulting largest at the negative and positive ends of the continuum and smallest at the center, that would represent neutral affect. The latest work of [123] reported a study concerning pupil size variation during and after auditory emotional stimulation. Their results showed that pupil size was significantly larger after both negative and positive than neutral stimulation. These results suggested that the autonomic nervous system is sensitive to systematically chosen highly arousing emotional stimulation. It is reasonable that the above contradictory results and theories may be due to the variety of stimuli used. Mostly, they have used limited sets of pictures varying in content, and they have suffered from methodological problems with color, luminance, and contrast [128]. Clearly, controlled stimulus set is a fundamental requirement for a systematic study of the effects of emotions on pupil size variation.

2.2.4 Cardio-Respiratory Coupling

The coupling between cardiac and respiratory patterns has been increasingly gaining interest in the scientific community. Starting from the pioneering work of Angelone et al. [129], the coupling between the respiratory system and the heart is known to be both neurological and mechanical [130, 131] as well as nonlinear [132]. However, the exact physiological mechanisms responsible for cardio-respiratory synchronization are, so far, poorly understood. In the literature, at least two levels of interaction are known.

One level is identified as the frequency modulation of the heart's primary pacemaker (sino-atrial node) through autonomic neural and hormonal control. In this level two concurrent effects take place, the efferent neural activity (the respiratory related rhythms [133]) and a mechanical coupling between the systems. In the latter, the variation of the intra-thoracic pressure causes a mechanical stretch of the sinus node, which alters the electrical properties of the sino-atrial node membrane, and therefore influences the frequency of heart excitation [134].

The second level has been found in the cardio-respiratory center of the brain stem where the respiratory rhythm is generated, [135]. At this level, the brain stem modifies the heart rhythm according to information regarding blood pressure provided by arterial baroreceptors, and, in turn, the baroreceptor reflex depends on the respiration phase [136].

> Nowadays, it is well accepted that the cardiovascular system and its relationship with respiration is a truly complex system. Therefore, nonlinearities and nonlinear coupling measures should be taken into account in its modeling and analysis [137].

As a matter of fact, the current literature provides plenty of nonlinear methods that are able to distinguish between healthy subjects and patients, and sometimes can even predict the status of the latter ones (e.g. see [100, 138]).

Although it is well-known that the cardiovascular and respiratory systems do not act independently, in the biological physics community these two systems were often considered to be not synchronized. So, there is a weak coupling between respiration and cardiac rhythm, and the resulting rhythms are generally not phase locked [139]. As a matter of fact, in rest conditions, while long synchronization episodes were observed in athletes and heart transplant patients (several hundreds of seconds) [140, 141], shorter episodes were detected in normal subjects (typical duration less than one hundred seconds) [141, 142].

In other several cases the cardio-respiratory synchronization was well demonstrated ([43, 143–145]). Since Pecora and Carroll [146] presented the conception of chaotic synchronization for two identical chaotic systems with different initial conditions, many synchronization methods have been proposed [147–151]. Recently,

Schafer et al. presented a new technique for the analysis of cardio-respiratory interaction, [140, 152], making use of their recent achievements in understanding hidden synchronization effects in chaotic and noisy oscillators [39, 153]. Even though some recent works have shown that ANS and cerebral cortex are implicated in the changes of cardio-respiratory synchronization during mental tasks [154], the effect of emotional stimuli on the cardio-respiratory interaction has been poorly investigated [155]. Starting from the hypothesis that respiratory and cardiac systems adapt their rhythms as a response to an external emotional stimulation, in this book it will be demonstrated that the cardio-respiratory system tends to become synchronized when experiencing strong affective events [36].

2.3 Emotion Elicitation

How emotions can be elicited is a crucial issue still open. The difficulty associated to the elicitation is related to a complex interaction between cognition and neurophysiological changes. Several modalities and several perceptual channels could be used for this purpose, which can be thought as affected by several "noisy" factors, including physiological process such as attention, social interaction, and body-to-biosensors connections. In the literature, a wide range of elicitation methods have been applied: introspection, movements, lights and colors [156], set of actions, images (e.g. IAPS described below) [157, 158], sounds (e.g., music and IADS described below) [12, 93, 159, 160], (fragments of) movies [161, 162], speech [163], commercials [164], games, agents/serious gaming/virtual reality [165], reliving of emotions [166], real world experiences [167, 168] along with using personalized imagery stimuli [92].

In order to induce a specific emotion, some of these methods employ stimuli belonging to international standardized databases. In this context, the International Affective Picture System (IAPS) [157] and the International Affective Digital Sounds system (IADS) [169] are two of the most frequently cited tools in the area of affective stimulation. They consist of hundreds of images and sounds, with associated standardized affective values. A commonly used approach is to have a collection of stimuli in which each is slightly varied in terms of intra-individual standard deviation of affective ratings.

In several experiments reported on this book, a set of images gathered from the IAPS is chosen [170]. Specifically, IAPS is a set of 944 images having a specific emotional rating, in terms of valence, arousal, and dominance. The emotional ratings are based on several studies previously conducted where subjects were requested to rank these images using the self assessment manikin [171]. The elicitation by IAPS is able to activate segregated neural representations of the different emotion dimensions in different prefrontal cortical regions [172, 173].

2.4 Affective Computing: From Theory to Emotion Recognition

Emotion recognition using intelligent systems is a crucial issue to be addressed for understanding human behavior, investigating mental health, interpreting social relations, etc. Recently, several engineering approaches have been used in order to guarantee acceptable emotion recognition systems having high accuracy, robustness, and adaptability to practical applications. An emotion recognition system is generally comprised of two main parts: emotion elicitation and identification of physiological correlates. Such systems are devised to map physiological patterns into well-defined emotional states for an automatic classification. The physiological signs include implicit and explicit emotional channels of human communication, such as speech, facial expression, gesture, physiological responses [7]. Recently, numerous automatic emotion recognition systems have been proposed involving, among others, patient-robot interactions [174], car drivers [175], facial expression [176], and adaptation of game difficulty [177]. Table 2.1 summarizes the most relevant results reported in the literature during the last decade about the emotion recognition through the ANS biosignal response [92–94, 165, 168, 175, 178–188]. All the acronyms used in this table are expanded in Table 2.2. Each row of Table 2.1 shows the first author along with the publication year, the set of physiological signals used for that study, the typology of stimulation pattern, the emotion classes, the type of the classifier and the results in terms of best percentage of successful recognition. Besides, the rest of the state-of-the-art of ANS-based emotion recognition is referred to a recent review written by Calvo et al. [7] which reports on the most relevant theories and detection systems using physiological and speech signals, face expression and movement analysis.

The detection and recognition of emotional information is an important topic in the field of *affective computing*, i.e., the study of human affects by technological systems and devices [91].

2.5 Emotions and Mood Disorders: The Bipolar Disorders

Mood has been defined as a long-lasting, diffuse, affective state, not associated to a specific trigger [189]. In turn, emotions are considered transient, acute and arousing responses to specific stimuli. It is well-known, however, that mood status affects the normal emotional response, and for this reason a possible assessment approach is to study the physiological variations provoked by external affective stimuli.

Table 2.1 Performance of the peripheral biosignal based emotion recognition methods reported in the literature of last decade

Authors	Signals	Elicitation	Emotion classes	Accuracy	Best results (%)
Picard et al. 2001 [92]	EMG, BVP, EDR, RSP	Internal feeling of each emotion	Neutral, anger, hatred, grief, platonic love, romantic love, joy, reverence	LDA	81.0
Lisetti & Nasoz 2004 [178]	ECG, EDR, ST	Film clips and difficult mathematics questions	Sadness, anger, fear, surprise, frustration, and amusement	MBA	84
Haag et al. 2004 [179]	EMG, EDR, ST, BVP, ECG, RSP	IAPS	Valence	ANN	90
			Arousal		96
Yoo et al. 2005 [181]	ECG, EDR	Video clip	Sad, calm pleasure, interesting pleasure, fear	ANN	80
Choi & Woo et al. 2005 [182]	BVP, EDR	Music and image chosen by subject	Joy, anger, and sadness	ANN	74.5
Healey & Picard 2005 [168]	EMG, ECG, EDR, RSP	Driving	3 stress levels	LDA	97
Li & Chen 2006 [183]	ECG, BVP, EDR, ST	Film clips	Fear, neutral, and joy	CCA	93.33
Rani et al. 2006 [184]	ECG, BVP, EDR, EMG	Cognitive tasks (i.e. anagrams and pong)	Engagement, anxiety, boredom, frustration and anger	SVM	86
Rainville et al. 2006 [185]	ECG, RSP, EDR, EMG	Self induction	Anger, fear, happiness, sadness	SDA	49
Zhai & Barreto 2006 [186]	EDR, BVP, PD, ST	Stroop test game	2 stress levels	SVM	90
Leon et al. 2007 [165]	ECG, EDR, BVP	IAPS	Neutral, negative, positive	ANN	71
Liu et al. 2008 [187]	ECG, ICG, BVP, HS, EDR, EMG, ST	Cognitive tasks (i.e. anagrams and pong)	Anxiety, engagement, liking	SVM	83
Katsis et al. 2008 [175]	EMG, ECG, RSP, EDR	Car-racing drivers	High stress, low stress, disappointment, euphoria	SVM	79.3
Yannakakis & Hallam 2008 [188]	ECG, BVP, EDR	Interactive games	2 fun levels	SVM, ANN	70
Kim & Andrè 2008 [93]	EMG, ECG, EDR, RSP	Music listening	4 musical emotion	LDA	70/95
Katsis et al. 2010 [94]	BVP, ECG, EDR, RSP	IAPS	Relaxed, neutral, startled, apprehensive, very apprehensive	ANN, SVM	84

Table 2.2 Peripheral biosignals and classification methods used in the literature, along with acronyms

Peripheral biosignals	Acronym
ElectroCardioGram	ECG
ElectroMyoGram	EMG
Blood Volume Pulse	BVP
ElectroDermal Response	EDR
ReSPiration Activity	RSP
Skin Temperature	ST
Pupil Diameter	PD
Impedance CardioGram	ICG
Heart Sound	HS

Classification methods	Acronym
Linear Discriminant Analysis	LDA
Marquardt Backpropagation Algorithm	MBA
Artificial Neural Network	ANN
Support Vector Machine	SVM
Canonical Correlation Analysis	CCA
Stepwise Discriminant Analysis	SDA

Specifically, paradigms based on emotional reactions have been proven to be widely able to differentiate among different mood states both in normal [190] and pathological conditions [191].

As a case study on patients, the concepts and methodologies developed in this book were applied to data coming from patients with bipolar disorders. *Bipolar disorder*, formerly known as manic-depressive illness, is a psychiatric condition in which patients experience drastic mood shifts. Typically, the disorder is cyclic with patients experiencing episodes of pathological low moods (depressive episodes), pathological elevated moods (maniacal or hypomaniacal episodes) and episodes in which depressive and maniacal symptoms are present at the same time (mixed episodes). In the intervals between these episodes, patients typically experience periods of relatively good affective balance (euthymia). Patients during a depressive episode experience a sad and desperate mood presenting a lack of interest together with other several neurovegetative symptoms including loss of appetite and sleep. Other symptoms such as cognitive retardation, somatic pain or functional symptoms (headache, dyspepsia etc.) are frequent as well. Depressed patients might also experience thoughts of ruin, guilt or death including suicidal thoughts that might end in suicide attempts. On the other hand, maniac patients express an increase in activity and an acceleration of thoughts. Rather than being a positive effect, these conditions are the cause of attention loss and prevent the patient from expressing a coherent mental stream of thoughts. Hyperactivity is often not finalized and patients switching from task to task are not able to complete any activity. In the maniac phase

patients also experience a reduction of the necessity to sleep, sleeping a few hours per night without feeling tired. Finally, mania is often dominated by a feeling of an excited mood with the idea of grandiosity and hypertrophic self-esteem. Maniacs, differently from hypomaniacs, might be delusional, e.g. they often believe of being a descendent of some important historical character. In the mixed state, patients share symptoms of both mania and depression, i.e. they exhibit symptoms of both mood states. For instance, patients can be hyperactive but have insomnia, have an increased self-esteem but also thoughts of inadequacy, and so on.

According to epidemiological studies,

> almost 15% of the population in the United States has suffered from at least one episode of mood alteration [192], and more than two million Americans have been diagnosed with bipolar disorder. Moreover, it has been estimated that about 27% (equals 82.7 million; 95% confidence interval: 78.5–87.1) of the adult European population, from 18 to 65 years of age, is or has been affected by at least one mental disorder [193, 194].

Despite its prevalence and the high cost of treating mood disorders, the clinical management of this condition is still ill-defined. First of all, this long-term illness may go undetected for years before it is diagnosed and treated. Secondly, bipolar patients are extremely heterogeneous with respect to the phenomenology and severity of the symptoms, the number and duration of the episodes, as well as the time interval between them. Even during euthymic periods (i.e. after remission from maniacal or depressive episodes), patients tend to experience sub-threshold mood alterations over time. In spite of the non-specific symptoms, currently the patient's mood is typically assessed by clinician-administered rating scales.

For clinical and research purposes, several clinical rating scales have been proposed and validated, but at present neither biological markers nor physiological signals highlighted in research studies are used for clinical purposes [195–197]. In this view, there is another fundamental issue concerning both the research and clinical domains. Relying on subjective mood evaluation alone, there is no possibility to evaluate the preclinical indicators of relapse or patient response to treatment. For instance, previous studies on sleep [198–200], circadian heart rate rhythms [201, 202] and the hormonal system [203–205] highlighted changes in these parameters according to the clinical status that may be considered predictors of clinical changes. However, none of these studies have reached an acceptable level of accuracy for clinical use in order to forecast the clinical course in single patients. A possible explanation for these negative results can be that mood disorders are more heterogeneous, in terms of psychophysiological, neuroendocrine and neurobiological correlates, than relatively simple clinical phenotypes usually adopted for clinical and also for research purposes. This might result in gathering subjects in groups that, although homogeneous in a clinical descriptive point of view, are extremely dishomogeneous in terms of endophenotypes.

2.6 Autonomic Nervous System as a Nonlinear Physiological System

Most of the methodologies developed and applied within this book are related to nonlinear dynamics and the theory of nonlinear system identification. This choice is justified by both physiological and experimental evidences.

As a matter of fact, it has been well-accepted by the scientific community that physiological models should be nonlinear in order to thoroughly describe the characteristics of such complex systems. Within the cardiovascular system,

> the complex and nonstationary dynamics of heartbeat variations have been associated to nonlinear neural interactions and integrations occurring at the neuron and receptor levels, so that the sinoatrial node responds in a nonlinear way to the changing levels of efferent autonomic inputs [29].

In fact, HRV nonlinear measures have been demonstrated to be of prognostic value in aging and diseases [24, 25, 99–101, 138, 206–211].

For instance, ApEn and DLE are adopted to characterize the complexity of HRV [46]. ApEn is chosen because it can distinguish between wide variety of systems. Moreover, its estimation can be achieved with relatively few points, as reported by Pincus et al. [104]. The DLE index has been already used in the literature, e.g. [109], to characterize HRV in terms of low-dimensional chaos-like determinism.

In several previous works [30, 212–215], it has been demonstrated how it is possible to estimate heartbeat (nonlinear) dynamics in cardiovascular recordings under nonstationary conditions by means of the analysis of the probabilistic generative mechanism of the heartbeat. Concerning emotion recognition, the crucial role of nonlinear dynamics has been demonstrated in order to perform an effective arousal and valence recognition from ANS signals [22, 31, 36, 46].

Part II
Methodology

The second part of the book reports on methodological advances related to data acquisition, signal processing and classification. In particular, experimental procedures applied to study healthy subjects and patients as well as novel wearable systems for physiological monitoring such as sensorized t-shirt and glove, eye-tracking hat, and the multi-parametric platform PSYCHE are described in Chap. 2. Concerning data analysis, ad-hoc pre-processing methods for noisy data as well as advanced feature extraction and classification techniques are reported in Chap. 3, particularly emphasizing the assessment of the autonomic nervous system nonlinear dynamics.

Chapter 3
Data Acquisition: Experimental Procedures and Wearable Monitoring Systems

In this chapter, the methodological procedures and techniques performed for mood and emotion recognition based on ANS signs are reported. It includes several experimental protocols successfully applied to elicit emotional variations in healthy subjects and in bipolar patients. The rationale behind all the proposed procedures is to maximize the ANS dynamical response under specific stimuli with respect to the baseline (rest condition).

The description of novel wearable systems able to perform an ubiquitous, pervasive, and comfortable ANS monitoring in a naturalistic environment is also reported along with a brief description of a standard portable ANS monitoring system.

3.1 Procedures on Healthy Subjects

The procedures described here were applied to ANS signals, i.e., HRV, RSP, and EDR, acquired from healthy subjects during a specific emotion-induced experiment through visual stimuli. As mentioned in Chap. 2, such affective stimuli are characterized by a common dimensional model which uses multiple dimensions to categorize the affective states, i.e. the Circumplex Model of Affects (CMA) [89]. In particular, a simplified version of the CMA is used where the affective states are conceptualized by the terms of valence and arousal, which can be intended as the two independent, predominantly subcortical systems that underlie emotions.

> Valence represents the extent to which an emotion is perceived as being pleasant or unpleasant. Arousal indicates the intensity of the emotion.

Accordingly, the stimuli are presented as images gathered from the International Affective Picture System (IAPS) having five levels of arousal and five levels of valence, including a neutral reference level. Peripheral physiological signals are simultaneously acquired. The experimental protocol was structured into the following

G. Valenza, E.P. Scilingo, *Autonomic Nervous System Dynamics for Mood and Emotional-State Recognition*, Series in BioEngineering,
DOI 10.1007/978-3-319-02639-8_3,

phases: recruitment of eligible subjects; elicitation of emotional stimuli; acquisition of the physiological signal set.

3.1.1 Recruitment of Eligible Subjects

A group of 35 healthy subjects, i.e. not suffering from both cardiovascular and evident mental pathologies, is recruited to participate in the experiment. Their age ranged from 21 to 24 and were naive to the purpose of the experiment. All participants were screened by Patient Health Questionnaire™ (PHQ) and only participants with a score lower than 5 were included in the study. Such a cut-off value was chosen in order to avoid the presence of either middle or severe personality disorders [216] such as subjects suffering from borderline personality disorders. It is well-known in the literature, indeed, that this typology of subjects show significantly lower levels of emotional awareness, a lesser ability in coordinating mixed valence feelings, a lower accuracy in recognizing facial expressions of emotion, and a more intense response to negative emotions than the non-borderline controls, [217]. The tests were evaluated by a team of expert psycho-physiologists from the University of Pisa. The test uses an empirical keying approach, where personality scales were derived from items endorsed by patients. It consists of 16 items, and usually took between 20 and 30 minutes (depending on the reading level). The test was given in Italian language since the subjects were Italian native speakers.

3.1.2 Stimulus Elicitation

The affective elicitation is performed by projecting a set of pictures to a PC monitor. These images are chosen from the official IAPS database [157, 170] which consists of hundreds of pictures with an associated specific emotional rating in terms of valence, arousal, and dominance. The emotional ratings are based on several studies previously conducted where subjects were requested to rank these images using the self assessment manikin [171]. In addition, the elicitation by IAPS is able to activate segregated neural representation of the different dimensions of emotion in different prefrontal cortical regions [172, 173].

In the proposed procedure, the slideshow is projected in a room equipped with a dedicated monitor and headset to acoustically insulate from external noise. The slideshow is comprised of 9 sessions of images N, $A1$, N, $A2$, N, $A3$, N, $A4$, N, where N is a session of 6 neutral images (mean valence rating $= 6.49$, $SD = 0.87$, range $= 5.52 \div 7.08$; mean arousal rating $= 2.81$, $SD = 0.24$, range $= 2.42 \div 3.22$), and A_i (with i going from 1 to 4) are sets of 20 images eliciting an increasing level of arousal and valence. Detailed values are reported in Table 3.1.

Each session is characterized by the valence/arousal rating, i.e. a 66% Confidence Interval (CI) expressed in terms of (Mean $\pm$ Standard Deviation) of the image

Table 3.1 Ratings and ranges of the IAPS images used in the procedures on healthy subjects (from [36])

Session	N. images	Valence rating	Valence range	Arousal rating	Arousal range
Neutral	6	6.49 ± 0.87	[5.52, 7.08]	2.81 ± 0.24	[2.42, 3.22]
Arousal 1	20	/	[2.87, 7.63]	3.58 ± 0.30	[3.08, 3.98]
Arousal 2	20	/	[1.95, 8.03]	4.60 ± 0.31	[4.00, 4.99]
Arousal 3	20	/	[1.78, 7.57]	5.55 ± 0.28	[5.01, 6.21]
Arousal 4	20	/	[1.49, 7.77]	6.50 ± 0.33	[5.78, 6.99]

Ranges are expressed as [min, max] values, whereas ratings are expressed as mean ± standard deviation

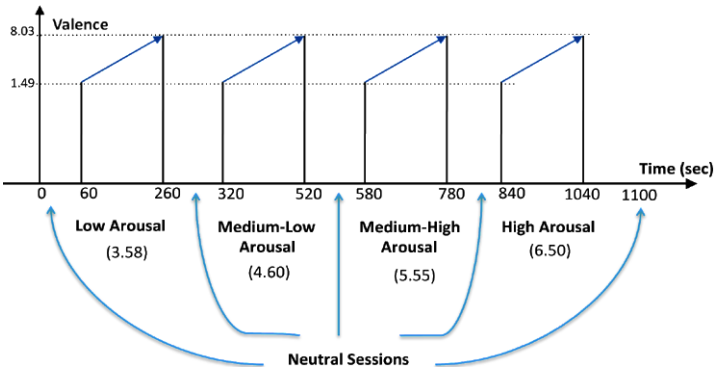

Fig. 3.1 Sequence scheme over time of image presentation proposed in the procedures on healthy subjects (from [36])

scores. Since even a single outlier (i.e. image with a score outside the CI boundaries) could strongly bias the session, the valence/arousal range information (i.e. from minimum to maximum score, reported in brackets as [min value,max value]) are also considered.

The overall protocol utilized 110 images. Each image is presented for 10 seconds for a total duration of the experiment of 18 minutes and 20 seconds. Figure 3.1 shows a graphical representation of the protocol. During the visual elicitation three physiological signals, ECG, RSP, and EDR are acquired.

In order to present arousal images with different valence (from unpleasant to pleasant), arousal sessions resulted to be longer than the neutral ones. This protocol ensures an unbiased measure of phase synchronization regardless of the valence of the considered images. Figure 3.1 shows a graphical representation of the protocol. In some cases, it could be useful to collapse the elicited valence and arousal session in a lower number of classes. In particular, arousal sessions can be divided into Low–Medium (L–M) and Medium–High (M–H) classes, according to the arousal score associated. Such sessions include 20 images eliciting an increasing level of valence (from unpleasant to pleasant). The L–M arousal sessions have

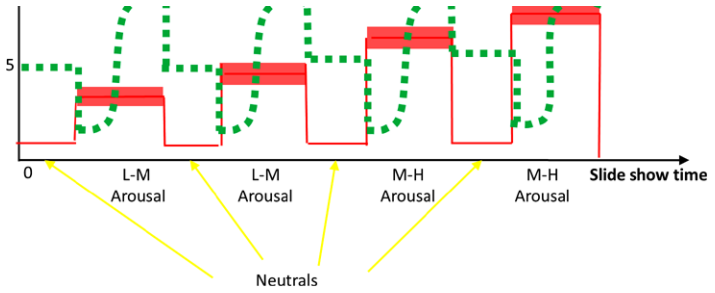

Fig. 3.2 Sequence scheme over time of image presentation in terms of arousal and valence levels. The *y axis* relates to the official IAPS score, whereas the *x axis* relates to the time

range valence rating $= 1.95 \div 8.03$, and mean arousal rating $= 4.01 \pm 0.30$, range $= 3.08 \div 4.99$. The M–H arousal sessions have range valence rating $= 1.49 \div 7.77$, and mean arousal rating $= 6.01 \pm 0.31$, range $= 5.01 \div 6.99$ (see the specific experimental protocol in Fig. 3.2). This simplified labeling of the sessions is successfully applied with the point-process approach for a personalized and instantaneous assessment of the fast emotional responses. The general overview of this analysis is shown in Fig. 3.3. In line with the CMA model, the combination of two levels of arousal and valence brings to the definition of four different emotional states. The stimuli, which stimulate several cortical areas also allowing the generation of cognitive perceptions [16], produce changes in the ANS dynamics through both sympathetic and parasympathetic pathways that can be tracked by a multidimensional representation estimated in continuous time by the proposed point-process model.

3.2 Procedures on Bipolar Patients

According to the state-of-the-art (see Chap. 2),

> it is reasonable to hypothesize that a correlation between mood disorders and dysfunctions involving ANS might exist.

To this aim, a novel approach to assessing the patient mood by using ANS-related biosignals gathered by wearable systems is proposed here. In this study, the psychophysiological variability in the same subject across different clinical states was considered. This approach is also justified by the small number of patients enrolled as well as the small number of examples for some classes. In the future, when a sufficient number of acquisitions are available, suitable data-mining techniques could be implemented in order to also investigate inter-subject variability. Considering such an intra-subject variability, the basic idea of this procedure is to bridge the

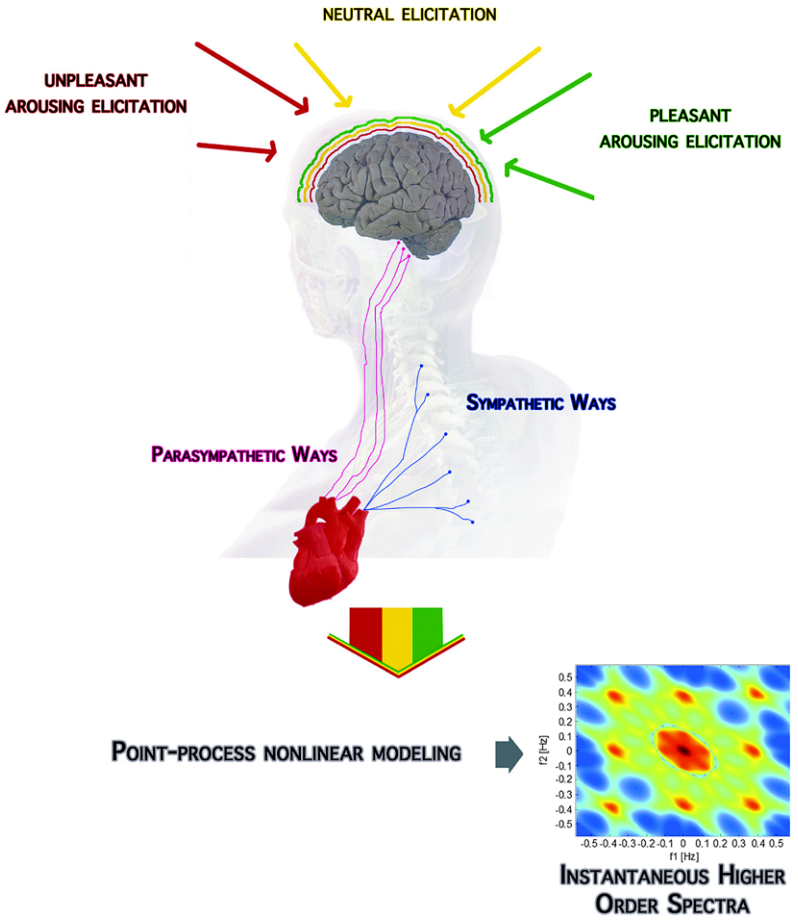

Fig. 3.3 An overview of the experimental set-up and rationale behind the emotional elicitation procedure on healthy subjects. The central nervous system is emotionally stimulated through images gathered from the International Affective Picture System. Such a standardized dataset associates multiple scores to each picture quantifying the supposed elicited pleasantness (valence) and activation (arousal). Accordingly, the *pictures* are grouped into arousal and valence classes, including the neutral one. During the slideshow, each image stands for 10 seconds activating the prefrontal cortex, along with other cortical areas, and thus producing the proper autonomic nervous system changes through both parasympathetic and sympathetic pathways. Starting from the ECG recordings, the RR interval series are extracted by using automatic R-peak detection algorithms applied on artifact-free ECG. A viable way to process the signals is represented by the point-process model which gives features in an instantaneous fashion

gap between research and the clinical routine management of bipolar patients integrating the traditional clinical standard procedures of mood assessment with data coming from the personalized monitoring systems for care in mental health (hereinafter PSYCHE) pervasive system which includes long-term physiological signals, as well as biochemical and behavioral data (see Sect. 3.3.2).

More specifically, this protocol aims to the identification of mood changes by acquiring and processing peripheral physiological signals from bipolar patients. They were monitored from the first hospital enrollment to the end of the therapy, i.e. euthymia condition. The study included up to a maximum of 6 evaluations performed for each patient, over a period of 90 days. The protocol implied a patient evaluation at the moment of the recruitment and a clinical assessment was repeated after one, two, four, eight, and twelve weeks.

3.2.1 Recruitment of Eligible Subjects and Experimental Protocols

Patients were recruited according to the following general inclusion/exclusion criteria:

- Age 18–65
- Diagnosis of bipolar disorder (I or II)
- Absence of suicidal tendencies
- Absence of delusions or hallucinations at the moment of the recruitment
- Absence of relevant somatic or neurological conditions
- Recent therapy switch

A physician presented the study to each patient. Before entering the study, each patient needs to sign an informed consent approved by the local ethical committee. Once enrolled, the patient is administered with a set of questionnaires and rating scales in order to assess the current mood at the hospital (see Sect. 3.2.2).

3.2.1.1 Long-Term Monitoring

The main experimental protocol for bipolar patients deals with a long-term monitoring in a naturalistic environment, performed by wearable systems. The clinicians associate to each patient a mood label in agreement with an ad-hoc mania–depression model described more in detail in the next section and suitably developed for this study. Before leaving the hospital, each patient is asked to wear the PSYCHE wearable system and keep it at all times until the battery ran out, i.e. approximately for 18 hours after leaving the hospital. The day after, the subject gave the t-shirt back and the data is downloaded and stored in the database.

3.2.1.2 Emotion-Related Tasks in Bipolar Patients

This book also focuses on the ANS changes induced by emotion-related tasks in bipolar patients. In this case, clinicians associated a mood label in agreement with one of the four possible defined mood states: euthymia, depression, mania or hypomania, and mixed-state.

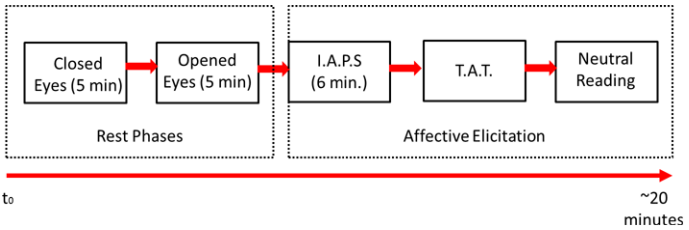

Fig. 3.4 Timeline of the emotional-related experimental protocol in bipolar patients

Each recording session was constituted by a dedicated affective elicitation protocol which started with two five minutes lasting phases of resting state with eyes closed and open, respectively. Subsequently, passive (IAPS) and active (TAT) visual stimuli were administered. In this case, the IAPS protocol implies a slideshow of pictures having two classes of arousal, either minimum or maximum, and random valence, ranging from unpleasant to pleasant. After the IAPS elicitation, the patients were asked to describe several TAT images. TAT stands for Thematic Apperception Test, a projective psychological test. The TAT is supposed to tap the subject's unconscious and reveal repressed aspects of personality, motives and needs for achievement, power and intimacy, and problem-solving skills. However, in this protocol the pictures were only used to elicit spontaneous comments from the patients. Of note, as there is no standardization of the use of the texts/pictures according to the subjects' clinical state, text/picture stimuli were always proposed in the same order. A schematic timeline of the experimental protocol is shown in Fig. 3.4. The described dedicated emotional elicitation protocol was performed according to the following timeline:

- 5 minutes of resting state with eyes closed;
- 5 minutes of resting state with eyes opened;
- IAPS slideshow: in which the subject observed a series of images at different content of arousal and random valence;
- TAT slideshow: in which the subject observed and commented particular images that investigate the unconscious of a person.

The ECG and RSP are acquired using the PSYCHE platform whereas the EDR signal was acquired by using the BIOPAC MP150 system (BIOPAC Systems, Inc., USA).

The presented paradigm is pretty heterogeneous and includes different conditions which elicit different emotional responses and different changes in arousal. In the future analyses, the perturbations of emotional baseline will be considered as a whole regardless of any differential analysis between the different parts of the protocol.

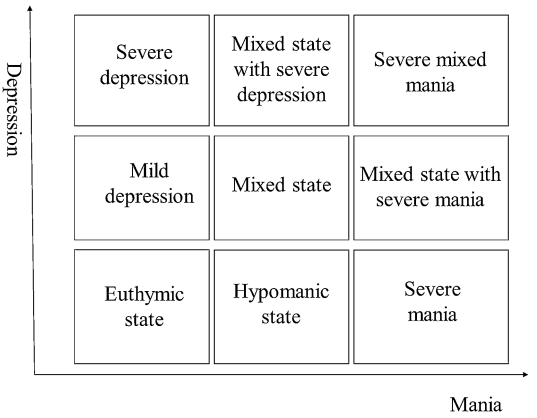

Fig. 3.5 The mania–depression model for mood assessment in bipolar patients (from [54])

3.2.2 The Mood Model

As mentioned in Chap. 2, the current clinical practice assesses the patient mood through clinician-administered rating scales and questionnaires, namely the Bauer internal mood scale (IMS) [218], the profile of mood states (POMS) [219], the 16th items version of the quick inventory of depressive symptomatology (QIDS) [220], and the Young mania scale (YMS) [221]. Concerning the Italian versions of these scales, IMS and YMS can be found in [222]. The Italian version of POMS was published by M. Farné et al. [223]. Finally, the Italian version of QIDS can be found in the web-page www.ids-qids.org/tr-italian.html. From a data mining point of view, it is necessary to have reliable mood labels associated to the points in the feature space. For this purpose, an ad-hoc model of mood states describing all of the possible states of the mental disorder is developed. During each clinical visit, each patient is diagnosed as belonging to a class of this model according to these clinical rating scales. The model is shown in Fig. 3.5. This model is built considering mania and depression not as opposite sides of a unique dimension, as it sometimes occurs in mood agendas, but as two different dimensions. In this way, the linear combination of the two allows for the possibility of identifying mixed states. Three levels with two degrees of severity for each of the two dimensions in order to have an approximate evaluation of the clinical severity were considered. This model has to be considered as a preliminary approach to categorize the mood states. In the literature other works exploring the mood assessment (e.g. A. Mehrabian et al. [224]) consider other basic dimensions. However, this is a preliminary clinical model that fits current needs since the purpose of the PSYCHE system was to classify different clinical states. Moreover, the algorithm for datamining might allow for multiple classes with a higher number of subjects. The model will be enriched with other dimensions (e.g. anxiety levels) as the number of subjects considered for the analysis increases.

3.3 Portable and Novel Wearable Systems for Autonomic Nervous System Monitoring

It has been pointed out in Chap. 2 how emotion elicitation is a crucial step to effectively characterize the emotional or mood state of a subject. Indeed, different kind of elicitation could generate different ANS dynamics leading to lower generality properties of the proposed emotion recognition system. Moreover, it is well known how the monitoring system used for data collection could bias the effectiveness of the eliciting stimuli and, therefore, the whole experiment. As a matter of fact, nowadays, in the research and industrial world the requirement of wearability is strongly increased.

To this aims, the description of three comfortable wearable systems able to acquire ANS signals, even in a naturalistic environment, is reported. More specifically, the following innovative wearable monitoring systems will be described: a glove based on textile electrodes able to acquire the EDR, the PSYCHE platform able to acquire the ECG-HRV and RSP, and the HATCAM able to perform the eye tracking in real-time along with the monitoring of the pupil size variation. In addition, a standard portable instrumentation, i.e., the BIOPAC System Inc., able to acquire all the mentioned peripheral signals but the eye tracking is also described.

3.3.1 The Glove System

In this section, a system prototype consisting of a fabric glove, with integrated textile electrodes placed at the fingertips, and a dedicated electronic card including an analog front-end, a digital block, and a wireless communication module for data transmission to a remote Personal Computer (see Fig. 3.6) is described. Due to manufacturing reasons, the fabric glove incorporates textile electrodes at level of the first four fingers, although only the first two have been tested for experimental sessions. The analog front-end consists of a DC voltage source of Volt, a Wheatstone bridge followed by a set of filters and amplifiers aiming at reducing noise, limiting bandwidth, amplifying and adapting the signal to the analog-to-digital converter (ADC) dynamics. The digital block consists of a Texas Instrument microcontroller, MSP430F169, which is an ultra-low power device. The microcontroller is endowed with an integrated 12-bit ADC and an integrated Universal Synchronous Asynchronous Receiver Transmitter (USART) for serial data transmission. The communication is realized by XBee-PRO 802.15.4 OEM RF transmitter module, which implements the IEEE 802.15.4 networking protocol. Finally, data were real-time transmitted to a remote PC.

3.3.1.1 Textile Electrode Performance Assessment

Textile electrode performances are experimentally assessed according to the scheme shown in Fig. 3.7. First, textile electrodes are characterized by identifying the

Fig. 3.6 *Fabric glove* including *textile electrodes* connected to a dedicated *electronic card* (from [22])

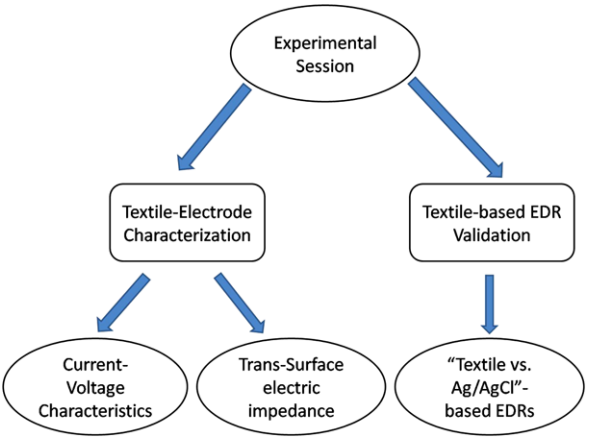

Fig. 3.7 Block diagram of textile electrode performance assessment (from [22])

current-voltage curve and evaluating the electrode impedance in terms of magnitude and phase in the bandwidth of the EDR. Afterwards, they are used together with standard electrodes Ag/AgCl in order to acquire simultaneously EDRs from them and make a quantitative comparison.

A suitable electrochemical cell is realized to characterize textile electrodes. It is comprised of a textile and a reference electrode immersed into a solution of potassium chloride (KCl) 0.1M. The cell structure is shown in Fig. 3.8. The two faces of the electrodes are connected to an external measurement device. Electrodes are placed at a distance of 3 millimeters and immersed into 0.015 liters of solution. Textile electrodes are provided by Smartex s.r.l. (Navacchio, Pisa), and have been al-

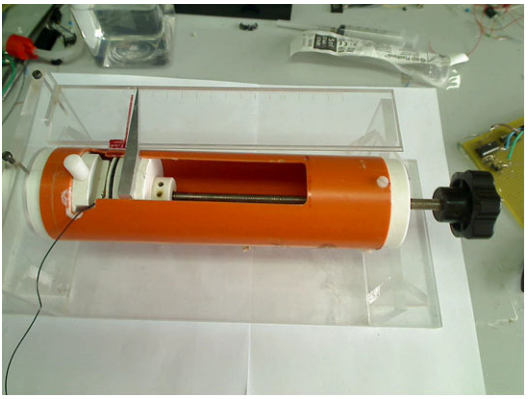

Fig. 3.8 Example of *electrolytic cell* (from [22])

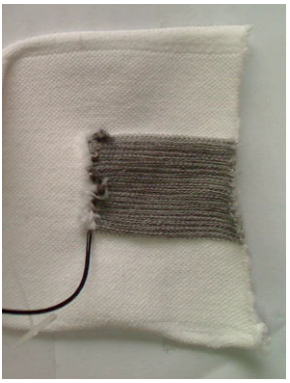

Fig. 3.9 Example of *textile electrode* (from [22])

ready cited and described in literature [21, 225]. They are made up of 80% polyester yarn knitted with 20% steel wire, with a dimension of 1×1 cm (see Fig. 3.9). The reference electrode is represented by a standard platinum electrode of 3×4 cm (see Fig. 3.10). The reference electrode size is chosen to be larger than the textile electrode in order to minimize border effects. The current-voltage characteristics were identified by applying a varying source voltage and determining the current flowing through the cell. This measurement is performed with the aim of investigating the electrode reaction due a potential drop applied between sensing and reference electrodes. In particular, an offset-free voltage varied from 1 to 20 peak-to-peak Volts, with an increasing step of about 1.2 volts, at frequency of about 0.1 Hz, has been applied. Experimental measurements were fitted by using the Butler–Volmer equation, which is defined as follows:

$$j = j_0\left(e^{\alpha(zF/(RT))\eta} - e^{-(1-\alpha)(zF/(RT))\eta}\right) \tag{3.1}$$

where j is the electrode density current [Am^2], j_0 is the exchange density current [Am^2], η is the over-potential [Volt], T is the absolute temperature [K], F is the Faraday constant, R is the universal gas constant, z is the valence of the ion, and α is the transfer coefficient. By analogy with Ohm Law ($V = IR$) and for small

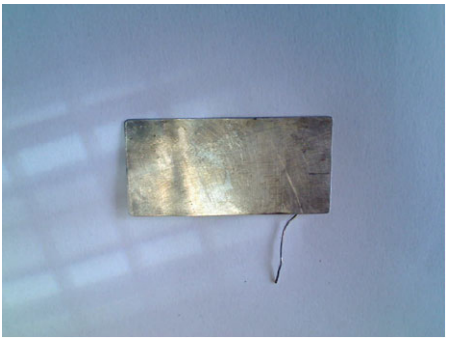

Fig. 3.10 Example of *platinum reference electrode* (from [22])

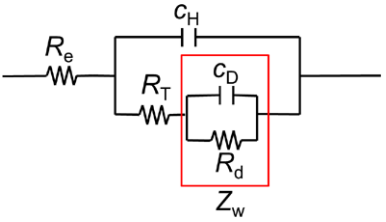

Fig. 3.11 Equivalent electric model of the textile electrode (from [22])

overpotentials the gradient of the relation between η and j can be interpreted as the equivalent resistance per unit area of the charge–transfer process on the electrode and which is called the charge transfer resistance R_T [226]. R_T can be obtained as follows:

$$R_T = \frac{\partial \eta}{\partial j} = \frac{TR}{\alpha z F j_0} \tag{3.2}$$

In order to evaluate the agreement of our experimental measurements with the Butler–Volmer equation, a nonlinear least square fitting method was used. The goodness of fit was evaluated by calculating the well-known statistic index *Adjusted R-square*.

The electrode is also characterized by estimating the trans-surface electric impedance. This measurement is used to investigate how the phase and amplitude of the electrode impedance change in the frequency domain. The impedance of electrodes in ionic liquids has been currently investigated experimentally and theoretically [227]. Figure 3.11 shows an equivalent circuit that models the relevant phenomena. In our experimental characterization, the same electrochemical cell is used with the same solution. The amplitude of the voltage applied between the electrodes was fixed while its frequency was varied in the range of the EDR bandwidth (from 0.01 Hz to 2.1 Hz with a step of about 0.13 Hz). In this equivalent circuit, C_H is the interface capacitance per area unit, which consists of the series combination of the Helmholtz double layer and the diffuse layer where Z_w is the Warburg impedance,

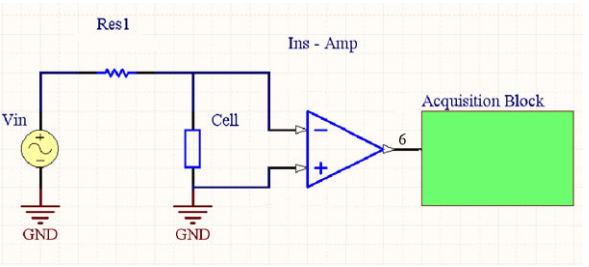

Fig. 3.12 *Electric circuit* used for the impedance characterization of the textile electrode (from [22])

R_T is the charge–transfer resistance and R_e is the spreading resistance. The Warburg impedance is reported as follows:

$$Z_w = \frac{\omega^{-1/2}}{A} \frac{k}{1+j} \tag{3.3}$$

where A is the electrode area and k [$\Omega s^{-1/2} cm^2$] is constant. The low frequency of EDRs implies, according to previous works [228], that both Warburg and interface capacitance terms are important for this characterization. All the experiments were carried out at 25°C and pressure of 1 atm. The electric circuit developed for the experimental characterization is illustrated in Fig. 3.12, where V_{in} is the generic voltage generator and R_{es1} is a resistance of 560 Ω connected in series to the cell. The voltage output was acquired using an instrumentation amplifier (*INA*118) with an input impedance of about 10^{13} Ω. Raw data were acquired by using a 6115*S*-series National Instrument acquisition board and processed by a personal computer.

3.3.1.2 Textile-Based EDR Validation

Textile-based EDR is further validated by simultaneously acquiring EDR through textile electrodes and standard Ag/AgCl electrodes. Both signals are acquired using the MP35 Biopac system with a sampling frequency of 1 KHz. It was found in the literature that skin conductance activity is greater at distal than medial site of fingers and is attributable to a greater number of active (open) sweat glands at distal site [229]. In order to correctly compare the EDRs from standard and textile electrodes, they were acquired simultaneously. Moreover, to minimize artifacts due to the different concentrations of sweat glands at the distal and medial sites, electrodes were placed in a crossed configuration, as shown in Fig. 3.13. Both signals were then filtered with a 2.5 Hz low-pass finite impulse response (FIR) filter approximated by a Butterworth polynomial. In order to consider only the variation of both textile and standard EDRs, data were normalized to the maximum value. The comparison was performed on the EDRs by means of a non-parametric correlation coefficient due to the non-gaussianity of both tonic and phasic signals. For this comparison, Spearman correlation [230] was chosen. Moreover, a ten-level wavelet decomposition was applied in order to obtain tonic and phasic signals using the Daubechies 5 function. The approximation at level 1 is tonic, and the details from levels 2 to 8 are phasic.

Fig. 3.13 Electrode placement (from [22]): with *orange standard electrodes* (case 1); with *blue textile electrodes* (case 2)

3.3.2 The PSYCHE System

The PSYCHE system is a personalized, pervasive, cost-effective, and multi-parametric monitoring system based on textile platforms and portable sensing devices for the long-term and short-term acquisition of data from a selected class of patients affected by mood disorders. It is designed and currently used in the frame of a European project, called precisely PSYCHE, which is funded in the seventh framework programme (FP7).

This project proposes a novel approach for bipolar disease management based on the paradigm that quasi-continuous monitoring in a natural environment provides parameters, indices and trends that will be used to assess mood status, support patients, predict and anticipate treatment response in its early phase, prevent relapse and to alert physicians in case of a critical event. The main goal of the PSYCHE project is to find out possible correlations between the patterns of physiological/behavioral signs and mood fluctuation over long term monitoring. The main novelty of this project is the number of features considered during signal processing, as opposed to previous works carried out in this field [198–202] where only a few parameters were considered. Extracted from linear and non linear methods, these features were investigated to find possible relationships between physiological signs and mental disorders. This approach increased the sensitivity and the specificity of the system functionality and therefore the success rate.

Patients wear the sensorized shirt and are free of performing whatever activity at home or elsewhere, while the aforementioned physiological signals were monitored and stored in a microSD card. After about 18 hours of monitoring, patients are

asked to bring the system back and the recorded data were manually sent to a central database. The final version of the PSYCHE system will provide an automatized storage process by means of a smartphone or a tablet personal computer without the involvement of a technician. Data will be automatically sent to a remote server where the processing and the data-mining procedures will be performed. The PSYCHE project includes the acquisition of other physiological signals as well as behavioral parameters (e.g. voice, activity index, sleep pattern alteration, biochemical markers), but they are not considered in this book. Moreover, the change in the diurnal variations of these measurements (circadian rhythms) may further allow achieving a better classification pattern and assessing other features in bipolar patients including response to therapy and proneness to relapse. A user-friendly device such as a smartphone for monitoring environmental information such as light, temperature and noise complete the PSYCHE platform. It is worthwhile pointing out that the experimental protocol undertaken in this study is novel with respect to the standard practice. A biochemical and psychological assessment was performed during the hospital admission. Since this book refers to the biomedical signal processing part of the PSYCHE project, the biochemical assessment was not considered. The experimental results showed in Chap. 5 demonstrated that the PSYCHE platform is able to recognize the mood state of the bipolar patients once the patients undergo an initial training session of a few acquisition sessions.

3.3.2.1 The Wearable Monitoring Platform

As mentioned before, the PSYCHE platform is the core sensing system of the PSYCHE project. It consists of a comfortable, textile-based sensorized t-shirt, embedded with fabric-based electrodes that can acquire ECG and RSP signals was used. This shirt is developed by Smartex s.r.l., Navacchio, Pisa. The inter-beat interval series (hereinafter RR) extracted from the ECG, i.e. the series constituted by the distance of two consecutive peaks of the ECG, and the respiratory dynamics were considered in the analysis strategy.

Figure 3.14 shows the wearable system prototype that employs textile electrodes to detect the ECG and a piezoresistive sensor is used to acquire the respiration signal. In addition, a three axial accelerometer is integrated into the system to track the movement. The technical specifications of the system are reported in Table 3.2.

3.3.3 HATCAM—Wearable Eye Gaze Tracking System

The system here proposed, HATCAM, is a new wearable and wireless eye tracking system which can be tailored to both adults and children. It is comprised of only one lightweight camera able to capture, by means of a mirror, the eyes of the subject and the scene in front of him, simultaneously. It exhibits the following properties:

(1) wearability;

Fig. 3.14 Wearable system prototype of the PSYCHE system (from [54])

(2) minimal obtrusiveness;
(3) eye tracking and pupillometry capabilities;
(4) lightweight below 100 g;
(5) wireless communication.

The system configuration is shown in Fig. 3.15. In detail, the system is comprised of a wireless CMOS camera (CP294) having low weight (20 g), low size ($2 \times 2 \times 2$ cm), and an A/V transmitter up to 30 m of distance. The camera has a resolution of 628×586 pixels with $F2.0$, $D45°$ optic, and 25 frames per second (f.p.s.). The original lens of the camera was removed and substituted with a wide-angle-lens without IR filter. This operation allows enlarging the view angle and acquiring infrared components, which emphasize the contrast between pupil and iris. This system is able to capture simultaneously, without latency, the visual scene in front of the subject and the position of his eyes. This is achieved using a mirror (4×0.6 cm) placed on a shaft linked to the head (see Fig. 3.15). Tilt and shaft of the mirror and the camera orientation can be tailored to the forehead profile of the user (see Fig. 3.15).

Figure 3.16 shows how the HATCAM is able to acquire simultaneously the eyes of the user and the scene in front of him using the mirror. Eye extraction procedure was constituted of visual inspection of the first video frame, in which a rectangular area including the eye was manually selected (see Figs. 3.17 and 3.18). This region is called Region Of Interest (ROI). Since the system mounted on the head, the ROI does not change throughout the experiment. In addition, only the red-image-component (see Fig. 3.18a) is converted in gray scale (see Fig. 3.18b) and used as input to the other processing blocks, as this component is specifically helpful in enhancing the contrast between pupil and background.

Table 3.2 Technical specifications of the wearable monitoring platform provided by Smartex s.r.l. (from [54])

Characteristics	
Power supply	Litium battery (life up to 24 hours)
Data storage	MicroSD card
Data communication	Micro USB, bluetooth
Electrocardiogram	
Measurement principle	Bio-potentials on the thorax
Sensors	Textile electrodes
Number of leads	1
Input auto configurable analog filter	0.67 Hz to 40 Hz
Analog-to-digital conversion	16 bits
Sampling rate	250 Hz
Respiration signal	
Measurement principle	Piezoresistive method
Range of electrical resistance	20 kΩ to 10 MΩ
Bandwidth	DC to 10 Hz
Resolution	12 bits
Sampling rate	25 Hz

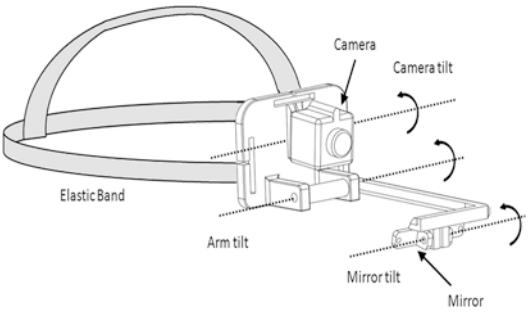

Fig. 3.15 HATCAM configuration (from [58, 59])

3.3.3.1 Photometric Normalization Technique

The purpose of the illumination normalization is to reduce or eliminate some variations in the captured eyes due to different conditions of illumination. It normalizes and enhances the eye image to improve the recognition performance of the system. For this purpose, the Discrete Cosine Transform (DCT) has been proposed by Chen et al. [231]. This approach is based on the Retinex theory (from the words "*retina*" and "*cortex*", suggesting that both eye and brain are involved in the processing) de-

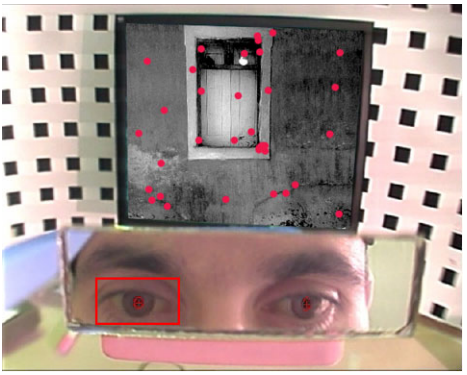

Fig. 3.16 Example of a single frame captured by the camera. The rectangular area marked up in *red* represents the ROI (from [58, 59])

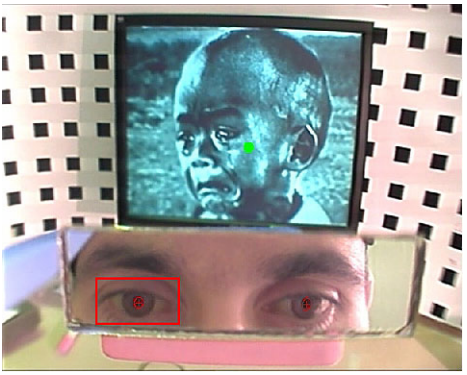

Fig. 3.17 Example of a single frame captured by the camera. The rectangular area marked by *red* represents the ROI (from [58, 59])

veloped by Land, [232]. This theory is based on color constancy assumption which ensures that the perceived color of objects remains relatively constant under varying illumination conditions. Land and his colleagues assume that the stimulus is not the result of the light source and surface reflectivity only, but that the visual system processes the stimulus, integrating the spectral radiance and generating a ratio of integrated radiance of any region of the scene with that of the brightest region. This stimulus is called *lightness*. This model eliminates the effect of a non uniform illumination and is completely independent of any a-priori knowledge of the surfaces reflectance and light source composition. According to this theory, the image intensity $I(x, y)$ can be simplified and formulated as follows:

$$I(x, y) = R(x, y)L(x, y) \tag{3.4}$$

where $R(x, y)$ is the reflectance and $L(x, y)$ is the illuminance at each point (x, y). The luminance L is assumed to contain low frequency components of the image while the reflectance R mainly includes the high frequency components of the image. The DCT technique compensates for illumination variations by truncating the low frequency components of the DCT in the logarithm domain. In the logarithm domain the theory is formulated as follows:

$$\log I(x, y) = \log R(x, y) + \log L(x, y) \tag{3.5}$$

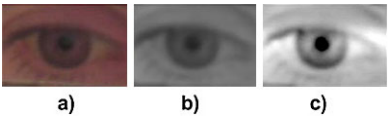

Fig. 3.18 *Red* component of the ROI (from [58, 59])

Fig. 3.18c shows the output of the DCT algorithm applied to gray scale image reported in Fig. 3.18b.

3.3.4 BIOPAC: Set of Physiological Signals and Instrumentation

When wearability is not a fundamental requirement of the experimental protocol, standard portable instrumentation can be used instead ofter giving better performance in terms of signal-to-noise ratio, resolution, sampling frequency, etc. The modules able to acquire physiological signals by using the BIOPAC MP150 are described in this section: ECG, RSP, and EDR. The proposed sampling rate is set to 250 Hz for all signals.

3.3.4.1 Electrocardiogram

ECG is acquired by means of the ECG100C Electrocardiogram Amplifier from BIOPAC inc., which records the D2 (II) lead ECG signal (bandwidth: 0.05–35 Hz) connected with pregelled Ag/AgCl electrodes placed following Einthoven triangle configuration. In the procedures reported in this book, ECG signal was used to extract the HRV [98], which reflects the sympathetic-parasympathetic balance.

3.3.4.2 Respiration

The dedicated module of BIOPAC MP150 used to record the respiration activity is RSP100C Respiration Amplifier with the TSD201 sensor, which is a piezo-resistive sensor with the output resistance within the range $5 \div 125$ KOhm and bandwidth of $0.05 \div 10$ Hz. This piezoresistive sensor changed its electrical resistance if stretched or shortened, and it was sensitive to the thoracic circumference variations occurring during respiration [233].

3.3.4.3 Electrodermal Response

In the literature, several approaches are used to measure this signal. In this section, a small continuous voltage applied to the skin is proposed to induce current which is measured through two Ag/AgCl electrodes positioned at the index and middle fingertips of the non-dominant hand. The ratio between voltage drop and induced current represents the skin electric impedance.

Chapter 4
Advanced Signal Processing and Modeling for ANS Data

In this chapter, advanced signal processing and modeling methodologies used for the analysis of ANS signals are reported. The main objective of such methods is to extract reliable and effective features, in a monovariate or multivariate fashion, able to characterize the emotional or mood status induced by an external stimulus. All the methodologies reported here are appropriate to be applied to data collected with standard portable or wearable systems using the procedures described in Chap. 3. In agreement with the current literature (see Chap. 2) and also on the basis of the comparative experimental results reported in the next chapter, a fundamental role in the methodological approach is played by nonlinear analysis.

It has been well-accepted by the scientific community, in fact, that physiological models should be nonlinear in order to thoroughly describe the characteristics of such complex systems. For instance, considering the cardiovascular system, the complex and nonstationary dynamics of heartbeat variations have been associated to nonlinear neural interactions and integrations occurring at the neuron and receptor levels, so that the sinoatrial node responds in a nonlinear way to the changing levels of efferent autonomic inputs [29].

However, whether a linear or nonlinear model is used, several limitations are present anyhow. For example, an interpolation process is required to cope with the intrinsic discrete and unevenly spaced heartbeat intervals. In previous works [30, 212–214], it has been demonstrated how it is possible to estimate heartbeat dynamics even in short recordings under nonstationary conditions by means of the point process theory, a powerful statistical tool able to characterize the probabilistic generative mechanism of physiological events. The unevenly spaced heartbeat intervals are represented as observations of a state-space point process model defined at each moment in time, thus allowing to estimate instantaneous HR and HRV measures [30, 212] without using any interpolation method.

Such a probabilistic approach is here proposed in a revised nonlinear version, and therefore it is able to provide novel instantaneous nonlinear features coming from the dynamic High Order Spectra (HOS).

G. Valenza, E.P. Scilingo, *Autonomic Nervous System Dynamics for Mood and Emotional-State Recognition*, Series in BioEngineering,
DOI 10.1007/978-3-319-02639-8_4,

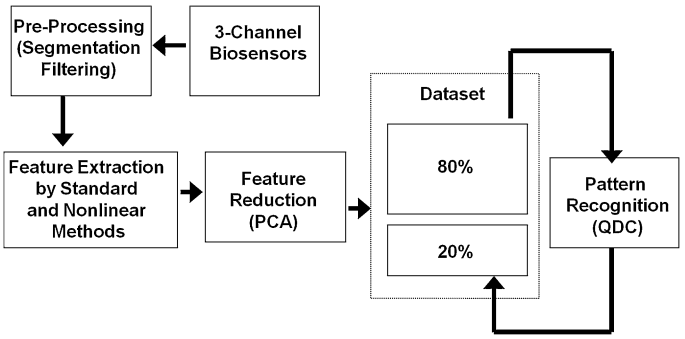

Fig. 4.1 Overall block diagram representing the acquisition and processing chain of three ANS signals (from [31])

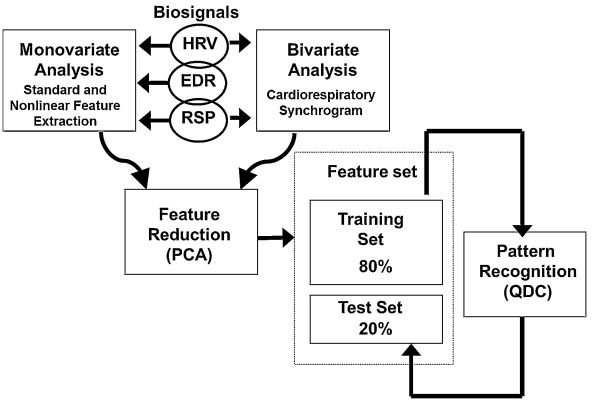

Fig. 4.2 Overall block diagram representing specific monovariate and bivariate analyses in the processing chain (from [38] "© Institute of Physics and Engineering in Medicine. Published on behalf of IPEM by IOP Publishing Ltd. All rights reserved.")

4.1 Overall Methodology

An overview of the general signal processing methodology is illustrated in Fig. 4.1. After the emotional elicitation, all the considered ANS signals are preprocessed, i.e. segmented and filtered. Afterwards, the most significant features are extracted and, then, reduced using the Principal Component Analysis (PCA) method. Finally, the feature set is classified using various machine learning methods [234].

More specifically, for each ANS biosignal, monovariate analyses can be applied in order to extract significant features using both standard and nonlinear techniques. Moreover, coupling measures by means of a bivariate analysis can be extracted from the RR interval series along with the RSP (see Fig. 4.2).

The general scheme proposed in Fig. 4.1 can be further modified in order to develop an effective mood recognition system by using, for instance, the PSYCHE platform to acquire ECG and RSP (see Fig. 4.3). In this case, a further preprocessing step able to robustly identify and discard motion artifacts is included (see Fig. 4.3).

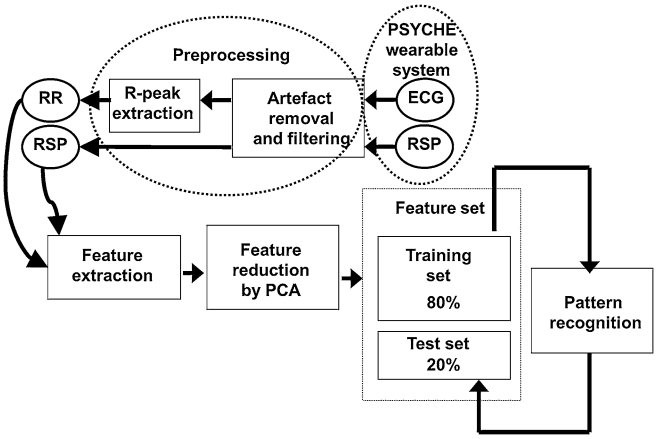

Fig. 4.3 Block diagram representing the acquisition and processing chain using the PSYCHE wearable platform (from [54])

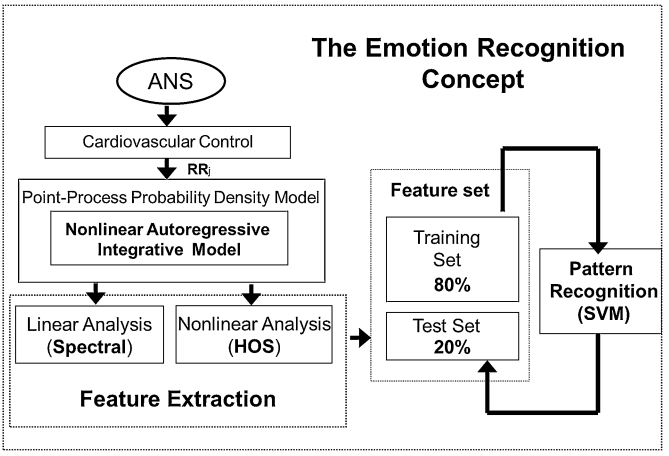

Fig. 4.4 Block scheme of the overall methodology for emotion recognition using point-process theory

Finally, an overall block diagram of the proposed recognition based on point-process theory system is illustrated in Fig. 4.4. As usual, the features obtained through the model are processed for classification.

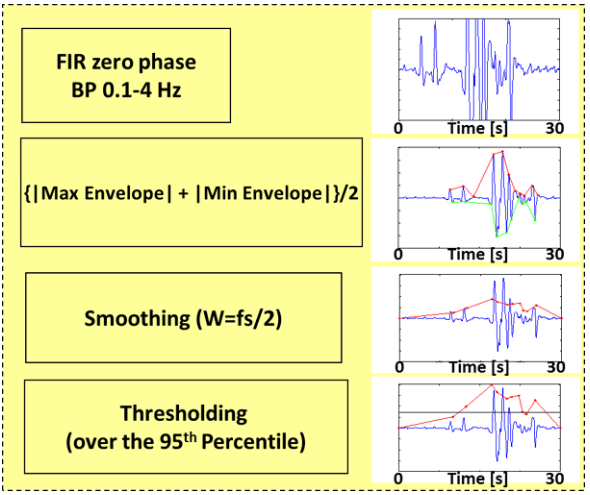

Fig. 4.5 Movement artifact removal algorithm (from [54])

4.2 Preprocessing

4.2.1 Movement Artifact Removal

Usually, signals acquired by wearable systems are strongly affected by movement artifacts because the ECG textile electrodes could lose contact with the skin during body movement. Therefore, an effective Movement Artifact Removal (MAR) algorithm must be applied to the signals before extracting the features. For this purpose, a simple and robust automatic MAR algorithm based on the four steps illustrated in Fig. 4.5 is developed. First, the ECG is filtered within the specific frequency band in which the movement artifacts were strongest, i.e. from 0.1 Hz to 4 Hz [235]. Then, the maximum and the minimum envelopes of the filtered data are calculated in order to extract the smoothed mean envelope. Movement artifacts are finally detected by means of simple statistical thresholds, i.e. 95th percentile, above which the signal is considered affected by artifacts. The parts of the signals with artifacts must be always discarded for further analysis.

4.2.2 Electrocardiogram and Heart Rate Variability

First, the ECG is pre-filtered through a Moving Average Filter (MAF) in order to extract and subtract the baseline. The frequency response of an M point moving average filter is expressed as follows:

$$\left|H[f]\right| = \frac{\sin\left(M\pi f\right)}{M\sin\left(\pi f\right)} \tag{4.1}$$

Accordingly, $M = 500$, which corresponds to a duration of 2 seconds, is proposed in order to obtain a cut-off frequency of 0.5 Hz, approximately. This choice is justified

by the guidelines provided by [236], suggesting to use a low-pass filter with a cut-off frequency below 0.67 Hz. Since HRV refers to the change over time of the Heart Rate (HR), a QRS complex detection algorithm could be used. The choice depends on the characteristics of the specific ECG signal [237], e.g. signal-to-noise-ratio (SNR), signal power, ECG leads. A common choice is represented by the algorithm developed by Pan–Tompkins [238], which allows for the extraction of each QRS complex and detection of the corresponding R-peak. Hence, the RR interval (t_{R-R}) is defined as the interval between two successive QRS complexes. Nevertheless, not all of the RR intervals obtained by the automatic QRS detection algorithm are correct. Any technical artifacts (i.e. errors due to the R-peak detection algorithm) in the RR interval time series may interfere with the analysis of these signals. Therefore, an artifact correction is needed. A proper piecewise cubic spline interpolation method [239, 240] can be adopted. Besides the above mentioned technical artifacts, physiological artifacts could be also present in the analyzed RR series. They include ectopic beats and arrhythmic events. A final check by visual inspection should be however always performed and only artifact-free sections must be included in further analysis. Another common feature that can significantly alter the analysis is the slow trend within the analyzed RR series. In fact, slow non-stationarities can be present in HRV signals and should be considered before the analysis [241]. In this book, the detrending procedure was implemented by means of an advanced method originally presented in [242]. This approach was based on smoothness priors regularization. The interval between two successive QRS complexes is defined as the RR interval (t_{R-R}) and the heart rate (beats per minute) is given by:

$$HR = \frac{60}{t_{R-R}} \tag{4.2}$$

As heart rate is a time series sequence of non-uniform RR intervals, this signal is further re-sampled at 4 Hz according to the algorithm of Berger et al. [243]. This algorithm is based on using an arbitrary frequency at which the heart rate samples will be evenly spaced in time, and using a local time window defined at each heart rate sample point as the time interval extending from the previous sample to the next. Successively, the number of RR intervals (including fractions of them) that occur within this local window are counted. The value r_i of the heart rate at each sample point is taken to be $r_i = f_r - n_i/2$ where f_r was the sampling frequency of the resulting heart rate signal and n_i was the number of *RR* intervals falling into the local window centered at the ith sample point [243].

4.2.3 Respiration

At this stage, the respiratory signal is treated in order to remove the baseline and reject the movement artifacts. Baseline removal is performed by means of MAF technique similarly to the ECG signal. Moreover, it is filtered by means of a tenth order low-pass Finite Impulse Response (FIR) filter with a cut-off frequency of 1 Hz approximated by Butterworth polynomial.

4.2.4 Electrodermal Response

EDRs is filtered by means of a 2.5 Hz low-pass FIR filter approximated by Butterworth polynomial. As reported in the literature, the bulk of the energy of the tonic component of the signal is considered to be in the frequency band ranging from 0 to 0.05 Hz, and the energy of the phasic component is in the band from 0.05 to 1–2 Hz [244]. Therefore, a Wavelet filtering, which is one of the best available non-stationary data analysis tool, is chosen. In detail, twelve levels wavelet decomposition can be applied in order to obtain tonic and phasic signals using Daubechies 5 function. Approximation at level 1 is the tonic component and details represent the phasic component.

4.2.4.1 EDR Deconvolution Analysis

The EDR signal is characterized by a slowly varying component called tonic component (i.e. Skin Conductance Level, SCL) and a superposed phasic component (Skin Conductance Response, SCR).

SCR is generally considered strictly related to a given stimulus and is defined as the part of the signal which arises within a predefined response window (1–5 s after stimulus onset), satisfying a minimum amplitude criterion (0.05 μS), [245, 246]. SCR is characterized by a short rise time followed by a slower recovery time. Generally, in case of an inter-stimulus interval shorter than the SCR recovery time, an overlapping of consecutive SCRs is visible. It results in one of the main EDR issue, since it does not allow a good estimation of responses as well as the signal division into its phasic and tonic components. In order to overcome this issue, the EDR signal process is modeled as a convolution process between the SudoMotor Nerve Activity (SMNA), as part of the sympathetic nervous system, and an Impulse Response Function (IRF) [247] under the hypothesis that EDR is controlled by SMNA resulting in a sequence of distinct impulses which regulate the eccrine sweat glands dynamics.

The IRF, also called Bateman function is modeled as a biexponential [248]:

$$IRF(t) = \left(e^{-t/\tau_1} - e^{-t/\tau_2}\right) \cdot u(t) \tag{4.3}$$

where $u(t)$ is the stepwise function. The result of deconvolution between EDR and IRF is defined as *driver function* which describes the SMNA behavior. The Bateman function is directly derived from bicompartment model of the diffusion process of the sweat through the sweat ducts (first compartment) and the stratum corneum (second compartment) [249].

Before applying the deconvolution analysis, EDR is filtered with a low pass zero-phase forward and reverse digital filter [250, 251] with a cutoff frequency of 2 Hz, to limit the frequency bandwidth of the EDR signal. The decomposition of the EDR in its components can be performed by means of Ledalab 3.2.2. software package for MATLAB [252]. In detail, EDR signal is described as follows [247]:

$$EDR = SMNA \otimes IRF \tag{4.4}$$

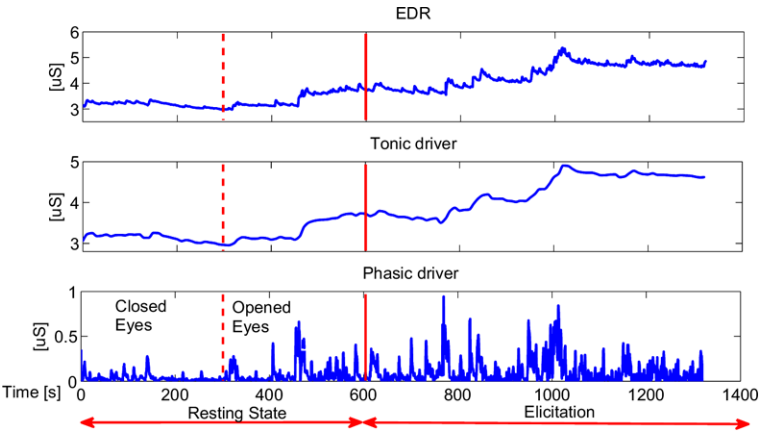

Fig. 4.6 Example of decomposition analysis. In the *upper* figure the EDR signal before the deconvolution analysis is reported. The *lower* figures report the deconvoluted tonic and phasic driver signals during resting and elicitation phase (from [55])

where $SMNA = (DRIVER_{tonic} + DRIVER_{phasic})$. The sum of the two driver functions is achieved by a deconvolution between the skin conductance data and the impulse response function. According to Eq. 4.4 the phasic driver is obtained subtracting the tonic from the deconvoluted signal. The hypothesis underling the EDR behavior is that tonic activity is observable in the absence of any phasic activity [253]. Therefore, the tonic component is obtained by the application of a smoothing Gauss window of 200 ms and a peak detection algorithm in order to find the peaks over a threshold of 0.2 μS (i.e. all the peaks over the threshold are identified as a part of the phasic response), and the points under the threshold are considered as part of the tonic driver. In order to estimate the continuous tonic driver signal, the points detected are used to build a 10-s spacing grid. Then, the grid points are interpolated with a cubic spline fitting method. As mentioned above, the phasic driver is the result of the subtraction between the continuos tonic and the deconvoluted signal. As shown in Fig. 4.6, the original EDR signal and the two deconvoluted tonic and phasic driver signals, during resting and elicitation states, are reported.

4.3 Feature Sets

Sets of features can be extracted in different ways. In this book, two categories of features are proposed: the first one consists of most standard and commonly used features, and the second category is comprised of features extracted from nonlinear dynamic techniques.

4.3.1 Standard Feature Set

Standard features are derived from the time series, statistics, frequency domain, geometric analysis for the whole set of physiological signals. In the following sections these methods are described in detail.

4.3.1.1 Heart Rate Variability

Heart rate variability (HRV) [24, 98] is concerned with the analysis of the time intervals between heartbeats. Several features can be extracted from this signal, both in the time and frequency domain. Time domain features include statistical parameters and morphological indexes. Defining, e.g., a time window related to the Normal-to-Normal beats (NN), several parameters are calculated, such as simple MNN and SDNN, which are the mean value and the standard deviation of the NN intervals, respectively. Moreover, the root mean square of successive differences of intervals (RMSSD) and the probability of the successive differences of intervals which differ by more than 50 ms (pNN50% expressed as a percentage of the total number of heartbeats analyzed) can be calculated.

Referring to morphological patterns of HRV, the triangular index can be calculated. It is derived from the histogram of RR intervals into NN window (TINN) in which a triangular interpolation was performed. Triangular interpolation approximated the RR interval distribution by a linear function and the baseline width of this approximation (base of the triangle) is used as a measure of the HRV index. In the literature, TINN is known to be correlated with SDNN as well as it is highly insensitive to artifacts and ectopic beats, because they are left outside the triangle.

The time domain methods are simple and widely used, but are unable to discriminate between sympathetic and para-sympathetic activity (although RMSSD can be considered to reflect mainly parasympathetic activity, since it is computed as differences between successive beats), while an appreciable contribution is given by the frequency domain parameters. All features extracted in the frequency domain were based on the Power Spectral Density (PSD) of the HRV. Methods for the estimation of PSD may be generally classified as non-parametric (like Fourier Transform) and parametric (model based) method. In this book, the Auto-Regressive (AR) model was used to estimate the PSD of HRV in order to provide better frequency resolution than nonparametric method. Furthermore, conventional frequency transformation based on the Fourier transform technique are not very suitable for analyzing non-stationary signals. Considering HRV as an output process $z(n)$ of a causal, all-pole, discrete filter whose input is white noise, the AR method of order p is expressed as the following equation:

$$z(n) = -\sum_{k=1}^{p} a(k)z(n-k) + w(n) \tag{4.5}$$

where $a(k)$ are AR coefficients and $w(n)$ is white noise of variance equal to σ^2.

AR(p) model is characterized by AR parameters $\{a[1], a[2], \ldots, a[p], \sigma^2\}$. In this book, the Burg method is used to get the AR model parameters, according to the results presented by Akaike [254, 255]. This method provides high resolution in frequency and yielded a stable AR model. The power spectrum of a pth order AR process is:

$$P_{zz}^{BU}(f) = \frac{\widehat{E}_p}{f_s|1 + \sum_{k=1}^{p} \widehat{a}_p(k) e^{-j2\pi f k}|^2} \tag{4.6}$$

where $\widehat{E}_p$ is the total least square error and f_s is the sampling frequency. Three main spectral components are distinguished in a spectrum calculated from short-term recordings: Very Low Frequency (VLF), Low Frequency (LF), and High Frequency (HF) components. It is well known, in the literature, that the distribution of the spectral power changes follow the ANS modulation. However, the VLF band is usually < 0.04 Hz and is almost never considered as an ANS marker because it is related more to thermal regulation [256]. The LF band is centered in 0.1 Hz (range: $[0.04 \div 0.15]$ Hz) and is mainly due to the arterial baroreceptor modulation. Current literature [24] suggests that the LF component of the power spectrum is strongly affected by the sympathetic system. The HF components (> 0.15 Hz) are also called respiratory components. A common viewpoint in the literature is that the HF peak can be considered as an index of the vagal activity [257]. However, available studies report the importance of HF and LF components and how their analysis per se cannot afford a precise delineation of the state of sympathetic activation [258]. Therefore, in addition to VLF, LF, and HF power, the LF and HF power in normalized units along with, especially, the LF/HF Ratio are proposed to give more information about the sympatho-vagal balance [24].

4.3.1.2 Respiration

By defining a time window W, standard RSP feature set is comprised of the ReSPiration Rate (RSPR), Mean and Standard Deviation of the First (MFD and SDFD, respectively) and Second Derivative (MSD and SDSD, respectively), i.e. variation of the respiration signal, Standard Deviation of the Breathing Amplitude (SDBA) and several statistical parameters. Respiration rate is calculated as the frequency corresponding to the maximum spectral magnitude. Statistical parameters are calculated in order to characterize the differences between inspiratory and expiratory phases (range or greatest breath). These parameters include the maximum (MAXRSP) and the minimum (MINRSP) value of breathing amplitude and their difference (DMMRSP). Other measures used to quantify the asymmetries between the two respiratory phases are obtained from the High Order Statistics (HOS). In detail, the third order statistics (i.e. Skewness), which takes into account the quantification of the asymmetry of the probability distribution, and the fourth order statistics (i.e. Kurtosis), which is a measure of the "peakedness" of the probability distribution are calculated. Moreover, another parameter is the Standard Error of the Mean (SEM),

which is calculated as follows: $SEM = \frac{\sigma}{\sqrt{n}}$ where σ is the standard deviation and n is the number of points within the window W. Concerning features in frequency domain, spectral power in the bandwidths $[0 \div 0.1$ Hz$]$, $[0.1 \div 0.2$ Hz$]$, $[0.2 \div 0.3$ Hz$]$, $[0.3 \div 0.4$ Hz$]$ can be also calculated [259].

4.3.1.3 Electrodermal Response

Standard methods for both tonic and phasic EDR features include the same statistics applied to the RSP signal above described: rate, i.e. central frequency, mean and standard deviation of the amplitude and statistical parameters, i.e. skewness, kurtosis, SEM and mean and standard deviation of the first and second derivative [170]. Moreover, further features are extracted only from the phasic component of EDR. More specifically, the maximum peak and the relative latency from the beginning of the image, Mean of Absolute of Derivative (MAD), Mean of Derivative for Negative Values (MDNV) only (mean decrease rate during decay time), Proportion of Negative Samples in the Derivative vs All Samples (PNSDAS), and spectral power in the bandwidths $[0 \div 0.1$ Hz$]$, $[0.1 \div 0.2$ Hz$]$, $[0.2 \div 0.3$ Hz$]$, $[0.3 \div 0.4$ Hz$]$ [259].

4.3.2 Features from Higher Order Spectra

In addition to the above-mentioned standard techniques High Order Spectra (HOS) from all the acquired signals are also investigated.

> HOS are defined as the Fourier transform of moments or cumulants of order grater than two.

In particular, the study of the two dimensional Fourier Transform of the third order cumulant, i.e. the Bispectrum [260, 261], is proposed. It is defined as:

$$B(f_1, f_2) = \iint_{t_1, t_2 = -\infty}^{+\infty} c_3(t_1, t_2) \exp^{-j(2\pi f_1 t_1 + 2\pi f_2 t_2)} \, dt_1 \, dt_2 \tag{4.7}$$

with the condition:

$$|\omega_1|, |\omega_2| \leq \pi \quad \text{for } \omega = 2\pi f$$

The $c_3(t_1, t_2)$ variable represents the third order cumulant, which is defined as follows:

$$c_3(t_1, t_2) = E\{s(t_1)s(t_2)s(t_1 + t_2)\} \tag{4.8}$$

where $s(t)$ is a square integrable stationary signal with zero mean. Thus, the bispectrum measures the correlation among three spectral peaks, ω_1, ω_2 and $(\omega_1 + \omega_2)$ and

estimates the phase coupling. Sometime, the bispectrum is unable to distinguish between pairs of frequencies strongly coupled and pairs of frequency weakly coupled but at high frequencies, because their bispectrum values are similar. In order to overcome this limitation, it is possible to evaluate the bicoherence function, according to Brillinger et al. [262].

$$B_{co}(f_1, f_2) = \frac{B(f_1, f_2)}{\sqrt{P(f_1)P(f_2)P(f_1 + f_2)}} \tag{4.9}$$

where $P(f)$ is the estimated power spectrum of the $s(t)$ signal. It has been demonstrated that the bispectrum has several symmetry properties [261] which divide the (f_1, f_2) plane in symmetric zones such as:

$$B(f_1, f_2) = B(f_2, f_1) \tag{4.10}$$

$$B(f_1, f_2) = B^*(-f_2, -f_1) \tag{4.11}$$

$$B(f_1, f_2) = B^*(-f_1, -f_2) \tag{4.12}$$

$$B(f_1, f_2) = B(-f_1 - f_2, f_2) \tag{4.13}$$

$$B(f_1, f_2) = B(f_1, -f_1 - f_2) \tag{4.14}$$

$$B(f_1, f_2) = B(-f_1 - f_2, f_1) \tag{4.15}$$

$$B(f_1, f_2) = B(f_2, -f_1 - f_2) \tag{4.16}$$

The bispectrum of a real signal is uniquely defined by its values in the triangular region of computation, $0 \leq f_1 \leq f_2 \leq f_1 + f_2 \leq 1$, provided there is no bispectral aliasing [262]. The bispectral feature set consisted of: Mean and Variance of Bispectral Invariants (MBI and VBI), i.e. mean and variance of $P(a)$, Mean Magnitude (M_{mean}) of the Bispectrum (MMB) and the Phase Entropy P_e (PEB), Normalized Bispectral Entropy P_1 (NBE) and Normalized Bispectral Squared Entropy P_2 (NBSE). All the features were calculated within the region defined in Fig. 4.7, according to results presented by Chang et al. [263] and Chua et al. [264, 265].

Specifically, let us introduce the bispectral parameter, $P(a)$, which is invariant to translation, dc-level, amplification, and scale. It is defined as follows:

$$P(a) = \arctan\left(\frac{I_i(a)}{I_r(a)}\right) \tag{4.17}$$

where:

$$I(a) = I_r(a) + jI_i(a) = \int_{f_1=0^+}^{1/(1+a)} B(f_1, af_1)\, df_1 \tag{4.18}$$

for $0 < a \leq 1$ and $j = \sqrt{-1}$ where a is the slope of the straight line on which bispectrum is integrated. In this book, the mean and variance of $P(a)$ are considered as features. Also Mean magnitude and phase entropy [263] are calculated within the region defined in Fig. 4.7.

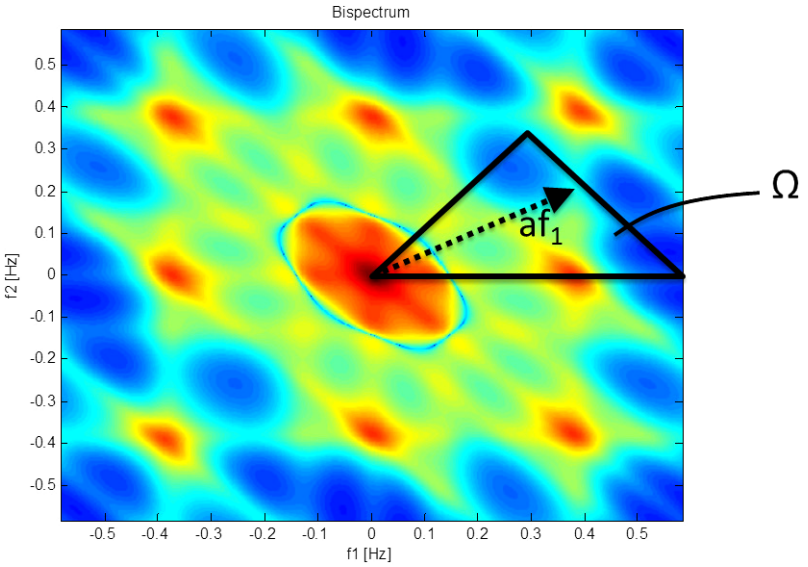

Fig. 4.7 Example of bispectrum invariant *triangular region*

Mean magnitude is defined as:

$$M_{mean} = \frac{1}{L}\sum_{\Omega}\left|B(f_1, af_1)\right| \tag{4.19}$$

and phase entropy is:

$$P_e = \sum_{n} p(\Psi_n)\log\left(p(\Psi_n)\right) \tag{4.20}$$

$$p(\Psi_n) = \frac{1}{L}\sum_{\Omega} 1\left(\Phi\left(B(f_1, af_1)\right)\epsilon\Psi_n\right) \tag{4.21}$$

$$\Psi_n = \left\{\Phi\left|-\pi + 2\pi n/N \le \phi \le -\pi + 2\pi(n+1)/N\right.\right\} \tag{4.22}$$

with $n = 0, 1, \ldots, N-1$.

L is the number of points within the region in Fig. 4.7, Φ refers to the phase angle of the bispectrum, Ω refers to the space of the defined region in Fig. 4.7, and $1(\cdot)$ is an indicator function which is equal to 1 when the phase angle Φ is within the range of bin Ψ_n in Eq. 4.22.

The mean magnitude of the bispectrum can be useful in discriminating between processes with similar power spectra but different third order statistics. However, it is sensitive to amplitude changes. The Normalized bispectral entropy (P_1) is equal

to:

$$P_1 = -\sum_n p_n \log(p_n) \tag{4.23}$$

where:

$$p_n = \frac{|B(f_1, af_1)|}{\sum_\Omega |B(f_1, af_1)|} \tag{4.24}$$

and Ω is the region as in Fig. 4.7.

Normalized bispectral squared entropy (P_2) is calculated as:

$$P_2 = -\sum_n p_n \log(p_n) \tag{4.25}$$

where:

$$p_n = \frac{|B(f_1, af_1)|^2}{\sum_\Omega |B(f_1, af_1)|^2} \tag{4.26}$$

and Ω is the region as in Fig. 4.7.

In addition, the sum of logarithmic amplitudes of the bispectrum can be computed as [266]:

$$\text{Hbis}_1(t) = \sum_\Omega \log\big(\big|\text{Bis}(f_1, f_2, t)\big|\big) \tag{4.27}$$

As well-known, the sympatho-vagal linear effects on HRV are mainly characterized by the LF and HF spectral powers [24, 257, 267–269]. Through bispectral analysis, it is possible to further evaluate the nonlinear sympatho-vagal interactions by integrating $|B(f_1, f_2)|$ in the appropriate frequency bands. Specifically, it is possible to evaluate:

$$\text{LL}(t) = \int_{f_1=0^+}^{0.15} \int_{f_2=0^+}^{0.15} \text{Bis}(f_1, f_2, t)\, df_1\, df_2 \tag{4.28}$$

$$\text{LH}(t) = \int_{f_1=0^+}^{0.15} \int_{f_2=0.15^+}^{0.4} \text{Bis}(f_1, f_2, t)\, df_1\, df_2 \tag{4.29}$$

$$\text{HH}(t) = \int_{f_1=0.15^+}^{0.4} \int_{f_2=0.15^+}^{0.4} \text{Bis}(f_1, f_2, t)\, df_1\, df_2 \tag{4.30}$$

4.3.3 Pupillometry and Gaze Point

This paragraph deals with the processing techniques used to detect the center of the eye and how its movements are mapped into the image plane. This technique is often referred to video oculography and involves visible spectrum imaging. It is a passive

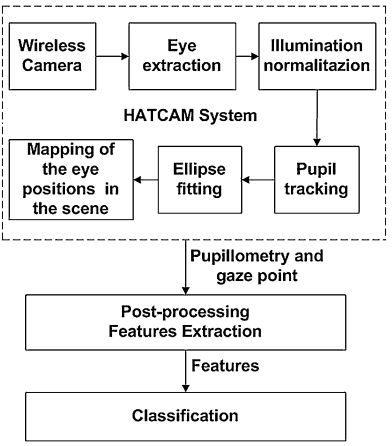

Fig. 4.8 Block diagram showing all the algorithmic stages of the processing of eyes and outside scene (from [58, 59])

approach that captures ambient light reflected from the eye. The mounted camera is modified to acquire also the IR components of natural light. Therefore, the system keeps the advantages of IR illumination in increasing the contrast between pupil and iris, and at same time preventing any possible injuries due to artificial IR illuminators, which are not required because of the presence of natural light. Figure 4.8 shows the block diagram of the algorithmic process used to classify visual stimuli having different affective arousal. The upper block implements the pupillometry and gaze point identification. The outputs are then processed to extract a specific set of features used for the classification. More in detail, the pupillometry and gaze point block is comprised of a sub-chain of blocks implementing eye extraction algorithm, photometric normalization algorithm of illumination, pupil contour and mapping of the eye center into the image scene. In the next sections, each block is described more in depth.

4.3.3.1 Pupil Tracking

Pupil tracking algorithm extracts the contour of the pupil exploiting the higher contrast of the pupil than the background due to the IR components of the natural light. Figure 4.9 shows the algorithm block diagram. More in detail, the first block binarizes the image by means of a threshold. Figure 4.10 reports the histogram of the eye, i.e. the distribution of the image pixel vs the gray levels from 0 to 255. The threshold divides the histogram into two groups of pixels having only two levels of gray; the zero level should group all the pixel belonging to the pupil whereas the 255 level should identify the background. The criterion implies choosing the threshold as the absolute minimum value in the range comprised between the two highest peaks of the eye histogram as reported in Fig. 4.10. An example of the binarization process is reported in Fig. 4.11. After binarization, two sheafs of lines starting from the middle points of the vertical sides of the image, with an angular aperture of 30°, are drawn. As result of the binarization process, the image borders are expected to

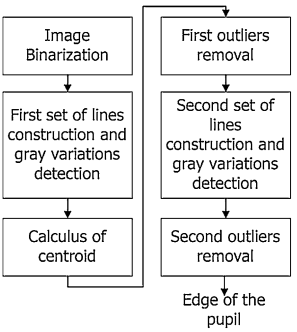

Fig. 4.9 Block diagram of the pupil tracking algorithm (from [58, 59])

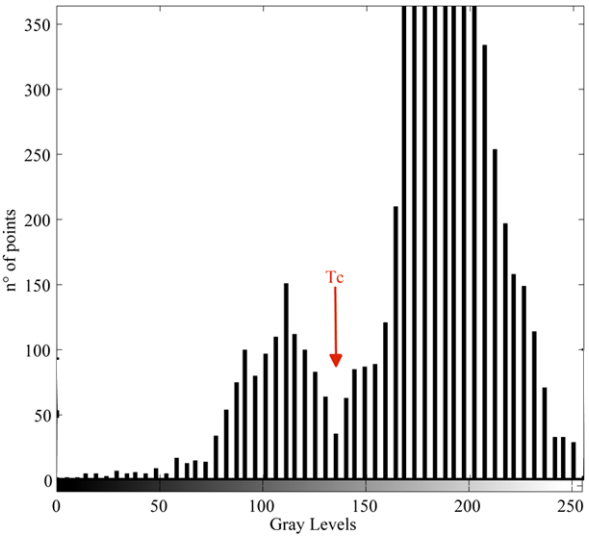

Fig. 4.10 Example of the histogram of the eye: T_c refers to the threshold identifying the eye and the sclera region (from [58, 59])

belong to the background, therefore the starting point of each line has a value of 255 in terms of gray level. Analogously, the pupil is expected to be placed roughly in the middle of the image (this is assured by an accurate freehand selection of the ROI). When each line encounters, along its path, a dark pixel, this latter can be thought to belong to the contour of the pupil. Afterwards, the centroid of these points is calculated. After removing all the outliers, being these points very far from the centroid with respect to the large point density (pupil edge), a large-grain approximation of the contour is obtained. Next, a sheaf of lines starting from the centroid with an angular aperture of 360°, and detects all discontinuities, but now from black to white. Finally, outliers are again removed. The result of this algorithm is a set of points constituting the pupil edge. This set will be the input of the fitting algorithm (see Fig. 4.12).

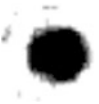

Fig. 4.11 Example the *eye image* after the binarization process (from [58, 59])

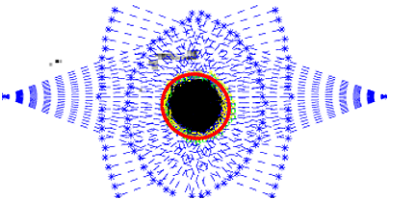

Fig. 4.12 Pupil tracking algorithm. Sheafs of lines are in *blue*; *black points* identify the eye including the outliers; *yellow points* highlight the pupil contour which is interpolated by the ellipse marked up in *red* (from [58, 59])

4.3.3.2 Ellipse Fitting

Ellipse fitting algorithm is implemented for constructing the pupil contour and detecting the center of the eye. Ellipse is considered as the best geometrical figure approximating the eye contour. According to the ellipse construction, it can be expressed by an implicit second order polynomial, being a central conic (with $b^2 - 4ac < 0$), such as:

$$F(x, y) = ax^2 + bxy + cy^2 + dx + ey + f = 0 \tag{4.31}$$

Ellipse fitting algorithms present in literature can be divided into two broad techniques: the clustering/voting (CV) and the least square (LSq) techniques. The first one uses two main approaches such as RANSAC and Hough Transform which are extremely robust but they are time-demanding or excessively resource consuming for real time machine vision [270, 271]. The LSq method is based on finding a set of parameters that minimize the distance between the data points and the ellipse. According to the current literature, this technique fulfills the real time requirement. One implementation of the LSq technique has been introduced by Fitzgibbon et al. [272], which is a direct computational method (i.e. B2AC) based on the algebraic distance with a quadratic constraint. In this book, a custom B2AC algorithm, where a Gaussian noise is added for algorithm stabilization [273], is used to calculate the center of the pupil (that coincides with the ellipse center), the axes dimensions as well as the eccentricity.

4.3.3.3 Mapping of the Eye Position

The mapping procedure associates the eye center position to the image plane of the scene, providing as result the gaze point. An experimenter guides this procedure. Firstly, the camera is positioned to capture both the scene (in our case the screen) and the mirror. In detail, tilt of the camera is adjusted as well as the tilt of mirror shaft and the tilt of the mirror to reflect the eyes. Each participant is asked to

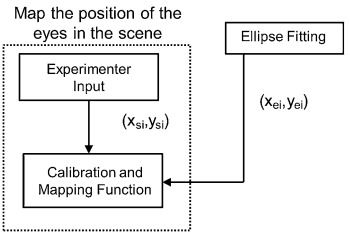

Fig. 4.13 Block diagram of the mapping function calculation process (from [58, 59])

look at some specific points of the screen. These points are identified by coordinates $s_i = (x_{si}, y_{si})$ referred to the image plane (i.e. the image plane captured by the camera) (see Fig. 3.17). The participants were instructed to keep their head as still as possible and to carefully look at each target point without blinking until looking at the next one.

The mapping function gets as input the center of the eye coming from Ellipse fitting block, and the coordinates of the gaze point on the image plane.

Mapping functions are quadratic polynomials defined as:

$$x_{si} = a_{11} + a_{12}x_{ei} + a_{13}y_{ei} + a_{14}x_{ei}y_{ei} + a_{15}x_{ei}^2 + a_{16}y_{ei}^2 \tag{4.32}$$

$$y_{si} = a_{21} + a_{22}x_{ei} + a_{23}y_{ei} + a_{24}x_{ei}y_{ei} + a_{25}x_{ei}^2 + a_{26}y_{ei}^2 \tag{4.33}$$

where x_{si}, y_{si} are the coordinates of the image plane (i.e. the coordinates of the point on the screen mapped into the image plane captured by the camera), and x_{ei}, y_{ei} are the coordinates of the center of the eye coming from the ellipse fitting block, referred to the image plane as well. The coefficients $a_{1,1\text{-}to\text{-}6}$ and $a_{2,1\text{-}to\text{-}6}$ are unknowns. Since each calibration point defines two equations, the system is over constrained with 12 unknowns and 18 equations, and can be solved using LSq method. A block diagram of the mapping function calculation progress is shown in Fig. 4.13.

4.3.3.4 Post-processing and Feature Extraction

Post-processing phase is based on parameters extracted by Recurrence Quantification Analysis (RQA), along with fixation time and pupil area detection. Each image can be represented as a matrix of 628 × 586 pixels. The gaze point is mapped into a pixel in each frame. A matrix of 628 rows and 586 columns, in which any position corresponding to the pixel coordinates associated to the gaze point is set to 1, is constructed. In order to minimize errors due to the eye blinking, only the pixels retained for at least five frames (0.2 sec) are set to 1.

4.3.3.5 Fixation Time

While watching each image, subject's eye can be caught by specific details. Fixation time of each pixel is defined as the absolute time during which the subject is dwelling on that pixel. A statistical distribution of fixation time over the fixed pixels is then obtained and the mode, which is defined here as T_{max}, is used as additional

feature. T_{max} is calculated for each image and each subject during both neutral and arousal elicitation as:

$$T_{max} = \max_{i=0}^{N}\left(t(P_i)\right) \tag{4.34}$$

where N is the number of points of gaze in the image, P_i is the ith point of gaze, $t(P_i)$ is the fixation time of the ith point of gaze, respectively.

4.3.3.6 Pupil Area Detection

The pupil area was approximated as an ellipse whose area is calculated for the pupillometry. To increase the robustness of the algorithm, averaged areas of both eyes are considered:

$$A_p = \frac{\pi r_a^l r_b^l + \pi r_a^r r_b^r}{2} \tag{4.35}$$

where A_p is the pupil area, r_a^l and r_b^l are the ellipse semi-axes of the left eye, r_a^r and r_b^r are the ellipse semi-axes of the right eye.

4.3.3.7 Most Visited Area in the Image

While looking at an image, there are areas more fixated than others. Hereby, the Most Visited Area (MVA) in the image is defined as the area of each image on which each subject lingered longer. Specifically, the area of the image is of $n \times n$ (where $n < N$) pixels, and the MVA was calculated as the sum of the fixation times of all the pixels inside this area. Let $T(x, y)$ be the time of fixation of the pixel whose coordinates are x, y. $T_{max}(x_c, y_c)$ is the maximum time of fixation of the image and (x_c, y_c) are the coordinates of the most watched pixel. The MVA can be calculated as:

$$MVA = \sum_{x,y=x_c-n/2,y_c-n/2}^{x_c+n/2,y_c+n/2} T(x, y) \tag{4.36}$$

where n is taken as forty pixels.

4.3.3.8 Length of the Gaze Path

The Length of the Gaze Path (LGP) of each image is calculated as the total length of the gaze path while the image was presented. The path between two consecutive points of gaze is approximated to a straight line, as two consecutive gaze points

were obtained from two consecutive frames, i.e. in a time interval of 1/25 seconds. The distance between two points was calculated as Euclidean distance.

$$LGP = \sum_{x,y=1}^{N} \sqrt{(x_i - x_{i+1})^2 + (y_i - y_{i+1})^2} \tag{4.37}$$

4.3.4 Nonlinear Methods for Feature Extraction

The evolution of a nonlinear system can be represented by a trajectory through a multidimensional space, often referred to as the phase space or state space.

If the multidimensional evolution converges to a subspace within the phase space, this subspace is called the attractor of the system [274]. Measures that are commonly used to describe the attractor in the phase space are dimension, entropy, and Lyapunov exponents.

A powerful basic technique used for analysis of complex dynamical systems is the so-called embedding procedure [275]. Embedding of a time series $x_t = (x_1, x_2, \ldots, x_N)$ is done by creating a set of vectors X_i such that

$$X_i = [x_i, x_{i+\Delta}, x_{i+2\Delta}, \ldots, x_{i+(m-1)\Delta}] \tag{4.38}$$

where Δ is the delay in number of samples and m is the number of samples (dimension) of the array X_i. When embedding a time series, the dimension m and the delay Δ of X_i must be chosen such that each vector X_i represents values that reveal the topological relationship between subsequent points in the time series. The number of samples in the embedded vector is usually chosen to be large enough to cover the dominant frequency in the time series, but m should not be so large that the first and last values in the epoch are practically unrelated. The evolution of the system can be represented by the projection of the vectors X_i onto a trajectory through a multidimensional space, i.e. the phase space. If the trajectory is comprised within a subspace in the phase space, then this subspace is called the attractor of the system.

Given a good estimation of the phase space, several features can be extracted by means of Recurrence Quantification Analysis, Lyapunov Exponents, Entropy measure, Detrended Fluctuation Analysis, etc.

4.3.4.1 Recurrence Plots and Recurrence Quantification Analysis

The Recurrence Plot (RP) [276] is a graph which shows all those times at which a state of the dynamical system recurs. In other words, the RP reveals all the times when the phase space trajectory visits roughly the same area in the phase space.

Natural processes, in fact, can have a distinct recurrent behavior, e.g. periodicities (as seasonal or Milankovich cycles), but also irregular cyclicities (as Southern Oscillation). Moreover, the recurrence of states, i.e. the states are arbitrarily close after a little while, is a fundamental property of deterministic dynamical systems and is typical for nonlinear or chaotic systems. The recurrence of states in nature has been known for a long time and has also been discussed in early publications (e.g. recurrence phenomena in cosmic-ray intensity, [277]). RPs were first introduced by Eckmann et al. [278] as a tool able to visualize the recurrence of states x_i in a phase space. RPs enable to investigate the m-dimensional phase space trajectory through a two-dimensional representation of its recurrences. When a state at time i recurs also at time j, the element (i, j) of a squared matrix $N \times N$ is set to 1, 0 otherwise. Such an RP can be mathematically expressed as:

$$R_{i,j} = \Theta\big(\epsilon_i - \|x_i - x_j\|\big) \tag{4.39}$$

where $x_i \in \mathbb{R}^m$, $i, j = 1, \ldots, N$; N is the number of considered states x_i, ε_i is a threshold distance, $\|\cdot\|$ a norm and $\Theta(\cdot)$ the Heaviside function which is defined as:

$$\Theta(z) = \begin{cases} 1, & \text{if } z \geq 0 \\ 0, & \text{if } z < 0 \end{cases} \tag{4.40}$$

In this book, the optimal value of ε_i [279] is chosen as follows:

$$\epsilon_i = 0.1 * A_{PD} \tag{4.41}$$

where A_{PD} is averaged phase space diameter of data x_i.

Following the above description, the Recurrence Quantification Analysis (RQA) [280] is a method of nonlinear data analysis which quantifies the number and duration of recurrences of a dynamical system presented by its state space trajectory. Quantification of RPs can be based either on evaluating diagonal lines to estimate chaos–order transitions or on vertical (horizontal) lines to estimate chaos–chaos transitions. RQA features used in this book are listed as follows.

Recurrence Rate (*RR*) is the percentage of recurrence points in an RP and it corresponds to the correlation sum:

$$RR = \frac{1}{N^2} \sum_{i,j=1}^{N} R_{i,j} \tag{4.42}$$

where N is the number of points on the phase space trajectory.

Determinism (*DET*) is the percentage of recurrence points which form diagonal lines:

$$DET = \frac{\sum_{l=l_{min}}^{N} l P(l)}{\sum_{i,j=1}^{N} R_{i,j}} \tag{4.43}$$

where $P(l)$ is the histogram of the lengths l of the diagonal lines.

Laminarity (*LAM*) is the percentage of recurrence points which form vertical lines:

$$LAM = \frac{\sum_{\upsilon=\upsilon_{min}}^{N} \upsilon P(\upsilon)}{\sum_{\upsilon=1}^{N} \upsilon P(\upsilon)} \tag{4.44}$$

where $P(\upsilon)$ is the histogram of the lengths υ of the diagonal lines.

Trapping Time *TT* is the average length of the vertical lines:

$$TT = \frac{\sum_{\upsilon=\upsilon_{min}}^{N} \upsilon P(\upsilon)}{\sum_{\upsilon=\upsilon_{min}}^{N} P(\upsilon)} \tag{4.45}$$

Ratio (*RATIO*) is the ratio between *DET* and *RR*:

$$RATIO = \frac{DET}{RR} \tag{4.46}$$

Averaged diagonal line length (L) is the average length of the diagonal lines:

$$L = \frac{\sum_{l=l_{min}}^{N} l P(l)}{\sum_{l=l_{min}}^{N} P(l)} \tag{4.47}$$

Entropy (*ENTR*) is the Shannon entropy of the probability distribution of the diagonal line lengths $p(l)$:

$$ENTR = -\sum_{l=l_{min}}^{N} p(l) \ln p(l) \tag{4.48}$$

Longest diagonal line (L_{max}) is the length of the longest diagonal line:

$$L_{max} = \max\left(\{l_i; i = 1, \ldots, N_l\}\right) \tag{4.49}$$

where N_l is the number of diagonal lines in the recurrence plot.

4.3.4.2 Detrended Fluctuation Analysis

Detrended Fluctuation Analysis (DFA) is a method for determining the statistical self-affinity of a signal. It is useful for analyzing time series that appear to be long-memory processes (diverging correlation time, e.g. power-law decaying autocorrelation function). It is related to measures based upon spectral techniques such as autocorrelation and Fourier transform. DFA method has proven useful in revealing the extent of long-range correlations in time series [281]. Briefly, the time series to be analyzed (with N samples) is first integrated. Next, the integrated time series is divided into boxes of equal length, n. In each box of length n, a least squares line is fit to the data (representing the trend in that box). The y coordinate of the

straight line segments is denoted by $y_n(k)$. Next, the integrated time series, $y(k)$, is detrended by subtracting the local trend, $y_n(k)$, in each box. The root-mean-square fluctuation of this integrated and detrended time series is calculated as:

$$F(n) = \sqrt{\frac{1}{N}\sum_{k=1}^{N}\left[y(k) - y_n(k)\right]^2} \tag{4.50}$$

4.3.4.3 Lyapunov Exponents

Deterministic chaos exhibits a number of features that distinguishes it from periodic and random behavior, more specifically by its sensitive dependence on initial conditions, which means that small changes in the state variables at one point will create large differences in the behavior of the system at some future point. This manifests itself graphically as adjacent trajectories that diverge widely from their initial close positions. The Lyapunov exponent is a quantitative measure of the average rate of this separation. A positive Lyapunov exponent indicates sensitive dependence on initial conditions and thus loss of predictability, indicative of deterministic chaos [282]. The Lyapunov exponent describes the speed of attraction as convergence, if negative, or divergence, if positive, of trajectories in each dimension of the attractor. In three dimensions, for instance, three Lyapunov exponents describe the evolution of the volume of a cube, and, in general, the sum of all Lyapunov exponents indicates how the measure of a hypercube evolves in a multidimensional attractor. The sum of positive exponents indicate the spreading rate of the hypercube, hence the increase of unpredictability per unit time. This dynamic is practically dominated by the largest positive (or Dominant) Lyapunov exponent (DLE). It describes the expansion along the principal axis (p_i) of the hypercube over a given time interval t. Formally, the exponents (λ_i) are calculated as:

$$\lambda_i = \lim_{t\to\infty} \frac{1}{t} \log_2\left[\frac{p_i(t)}{p_i(0)}\right] \tag{4.51}$$

where λ_i are ordered from largest to smallest. The calculation of the DLE in short time series is not a trivial task. For experimental applications, in fact, a number of researchers have proposed algorithms that estimate the Dominant Lyapunov exponent [283–287], or the positive Lyapunov spectrum, i.e., only positive exponents [287]. Here, the approach proposed by Rosenstein et al. [102], which ensures reliable values of DLE even in short data sets, is suggested. This method, in fact, is easy to implement and fast because it uses a simple measure of exponential divergence that circumvents the need to approximate the tangent map. In addition, the algorithm does not require large data sets. More in detail, the attractor dynamics was reconstructed from a single series by means of the embedding procedure [275]. The embedding dimension is usually estimated in accordance with Takens's theorem [275]. A common choice for the time delay estimation by means of the correlation sum was addressed by Liebert and Schuster [288]. After reconstructing

the dynamics $X_i(t)$, the algorithm locates the nearest neighbor of each point on the trajectory. The nearest neighbor, $X_{\hat{j}}$, is found by searching for the point that minimizes the distance to the particular reference point, identified by the vector X_j. This is expressed as:

$$d_j(0) = \min_{X_{\hat{j}}} \|X_j - X_{\hat{j}}\| \tag{4.52}$$

where $d_j(0)$ is the initial distance from the jth point to its nearest neighbor, and $\|\cdot\|$ denotes the Euclidean norm. The largest Lyapunov exponent, also known as Dominant Lyapunov Exponent (DLE), is then estimated as the mean rate of separation of the nearest neighbors. When applied to HRV series, the time delay Δ is often held constant to 1.

4.3.4.4 Approximate Entropy

Approximate Entropy (ApEn) measures the complexity or irregularity of the signal [108, 289].

The ApEn algorithm can be computed as follows. First, a set of length m vectors u_j is formed:

$$u_j = (RR_j, RR_{j+1}, \ldots, RR_{j+m-1}) \tag{4.53}$$

where $j = 1, 2, \ldots, N - m + 1$, m is the embedding dimension, and N is the number of measured RR intervals. The distance between these vectors is defined as the maximum absolute difference between the corresponding elements, i.e.:

$$d(u_j, u_k) = \max_{n=0,\ldots,m-1} \left\{ |RR_{j+n} - RR_{k+n}| \right\} \tag{4.54}$$

Next, for each u_j the relative number of vectors u_k for which $d(u_j, u_k) \leq r$ is calculated, where r is the tolerance value. The index is denoted with $C_j^m(r)$ and can be written in the form:

$$C_j^m(r) = \frac{\text{nbr of } \{u_k | d(u_j, u_k) \leq r\}}{N - m + 1} \quad \forall k \tag{4.55}$$

The value of $C_j^m(r)$ is always lesser than or equal to 1. Note that the value is, however, at least $1/(N - m + 1)$ since u_j is also included in the count. Then:

$$\Phi^m(r) = \frac{1}{N - m + 1} \sum_{j=1}^{N-m+1} \ln C_j^m(r) \tag{4.56}$$

Finally, the approximate entropy is obtained as:

$$ApEn(m, r, N) = \Phi^m(r) - \Phi^{m+1}(r) \tag{4.57}$$

The value of the estimate ApEn depends on three parameters: the length m of the vectors u_j, the tolerance r, and the data length N. When applied to HRV series, m is often chosen as $m = 2$. The length N of the data also affects ApEn. As N increases the ApEn approaches its asymptotic value. The tolerance r has a strong effect on ApEn and should be selected as a fraction of the standard deviation of the signal. A common selection for r is $r = 0.2 \cdot SD$, which is also adopted in this book. Large values of ApEn indicate high irregularity and smaller values of ApEn indicate a more regular signal.

4.3.4.5 Multiscale Entropy

Multiscale Entropy (MSE) is based on the calculation of the Sample Entropy (*SampEn*) over several time series, which are constructed from the original discrete time series by averaging the data points within non-overlapping windows of increasing length, τ. Formally, given a time series $\{x_1, \ldots, x_i, \ldots, x_N\}$ and a scale factor τ, each element of a course-grained series $\{y^{(\tau)}\}$ is calculated as $y_j^{(\tau)} = \frac{1}{\tau} \sum_{i=(j-1)\tau+1}^{j\tau} x_i$, $1 \leq j \leq N/\tau$ and, for each of the series, $y_j^{(\tau)}$, *SampEn* [104, 108, 290] is computed. *SampEn* estimation on each series starts with the calculation of the distance between two vectors x_1 and x_j on the phase space $x(1), x(2), \ldots, x(N - m + 1)$, which is defined in $\mathbb{R}^m$, where $m \leq N$ is a positive integer associated to the embedding dimension of the series [275, 291]. Then, all the distances within a radius r are counted and normalized by the quantity $N - m + 1$. This procedure is performed twice considering the chosen value of m and $m + 1$.

Previous studies suggest a fixed straightforward choice of the parameters as $m = 2$, and $r = 0.15\sigma$ where σ is the standard deviation of the series [290]. While such a choice could be reasonable for the m values, it could be pretty hazardous for the r value.

Therefore, it is reasonable to consider different r values for each acquisition of each subject such that maximizes the calculation of *ApEn* in the range $0.01 \leq r \leq 1.2$ [292–295]. The highest value $ApEn(r_k)$ is interpolated with the preceding and the following values, $ApEn(r_{k-1})$ and $ApEn(r_{k+1})$, with a parabola. The position of the vertex of the parabola gives r_{max}, and $ApEn(r_{max})$ quantifies the highest information difference between vectors of length m and $m + 1$.

4.3.5 Cardio-Respiratory Synchronization Analysis

Concerning general dynamical systems, all the possible mode-lockings are defined by the Farey tree [296, 297] (i.e. level 1: frequency ratio: 1 : 1; level 2: frequency ratio: 1 : 2; level 3: frequency ratios: 1 : 3, 2 : 3; level 4: frequency ratios: 1 : 4, 2 : 5, 3 : 5, 4 : 3; etc.). Considering the cardio-respiratory system, the generic synchronization ratio $n : m$ indicates that m heart beats fall within n respiratory periods. It

is clear that several of the mentioned Farey ratios cannot be used to describe physiological cardio-respiratory behaviors, such as level 1 and level 2. Indeed, the majority of healthy subjects have a resting heart rate between 50 (0.82 Hz) and 90 (1.5 Hz) bpm [298] and breathing rates between 10 (0.17 Hz) and 20 (0.33 Hz) breaths/min [299]. Therefore the resulting range for the ratio $n:m$ is between $0.33/0.82 = 0.4$ and $0.17/1.5 = 0.11$. In this book, the following physiologically plausible ratios: $1:6, 1:5, 1:4, 1:3, 2:9, 2:7, 3:11, 3:10, 3:8$ are considered.

4.3.5.1 Instantaneous Phase

In order to study the phase synchronization between two signals, it is necessary to obtain instantaneous phases at least for the slower oscillating signal, i.e., for respiration in our case. For a real valued continuous signal $x(t)$, this can be done within an analytic signal approach, adding a corresponding imaginary part $i\tilde{x}(t)$ to the signal. $\tilde{x}(t)$ is calculated by employing Hilbert transform [300]:

$$\tilde{x}(t) = \frac{1}{\pi} PV \int_{-\infty}^{\infty} \frac{x(t')}{t - t'} dt' \tag{4.58}$$

where PV denotes the Cauchy principal value. Finally, instantaneous phases can be defined from real and imaginary parts of the analytical signal:

$$\phi(t) = \arctan\left[\frac{\tilde{x}(t)}{x(t)}\right] \tag{4.59}$$

4.3.5.2 Cardio-Respiratory Synchrogram

By definition, in the simplest case of two periodic oscillators, synchronization is classically understood as phase locking:

$$|\varphi_{m,n}| = |m\phi_1 - n\phi_2| < c \tag{4.60}$$

where m and n are some integers that describe the locking ratio, c is a constant value, $\phi_{1,2}$ are the phases of the oscillators, and $\varphi_{m,n}$ is the generalized phase difference, or relative phase. The phases $\phi_{1,2}$ are not cyclic on the interval $[0, 2\pi]$, but are defined on the whole real line. Schafer et al. used the concept of phase synchronization of chaotic oscillators [39, 40] to develop a technique to analyze irregular non-stationary bivariate data, i.e. the Cardio-respiratory synchrogram (CRS) [37, 140, 152]. In the general case of $m:n$ synchronization, such a structure appears if the phases of the heart beats is related to the beginning of m adjacent respiratory cycles:

$$\varphi(t_k) = \frac{\phi_r(t_k) \mathrm{mod}(2\pi m)}{2\pi} \tag{4.61}$$

where ϕ_r refers to the instantaneous phase of the respiratory signal and t_k is the time where the R-peak in the kth heartbeat occurs and hence the phase of the heart rhythm increases by 2π. ϕ_r is calculated by means of the Hilbert transformation [39]. CRS is obtained by plotting these relative phases φ as a function of t_k. Therefore, if $m : n$ phase synchronization occurs, then CRS is constituted by n horizontal stripes within m respiratory cycles. In case of $1 : n$ synchronization (i.e., if n heartbeats fit to one breathing cycle) one observes n parallel horizontal (or at least approximately horizontal) lines in the synchrogram. This technique allows distinguishing between different periods of synchronization, even for noisy and non-stationary data [140, 152].

4.4 Feature Reduction Strategy

Given a large number of extracted features, a suitable feature reduction strategy is necessary in order to perform an effective pattern recognition. Feature reduction can be performed in different ways. The current literature distinguishes two main categories of reduction methods: feature selection and feature projection. In this book, a simple and well-known feature projection method is used in order to retain the most information from all features. Specifically, the Principal Component Analysis (PCA) [301] is adopted, which is able to project high-dimensional data to a lower dimensional space with a minimal loss of information. This means that new features were created by the linear transformation of original feature values, rather than by selecting a feature subset from a given feature set. Details are reported in the following paragraph.

4.4.1 Principal Component Analysis

PCA [301] is a useful statistical technique that projects a correlated high-dimensional space of variables to an uncorrelated low-dimensional space of variables. These variables are ordered according to decreasing variance and are called principal components. PCA uses the eigenvalues and eigenvectors generated by the correlation matrix to rotate the original dataset along the direction of maximum variance. Accordingly, the above general description was implemented by means of the Singular Value Decomposition (SVD). For the dataset matrix X, of dimension $n \times p$ and rank r, it can be rewritten using SVD as:

$$X = USV^T \tag{4.62}$$

where U is an orthogonal $n \times r$ matrix, V is an orthogonal $p \times r$ matrix with the eigenvectors $(e_1, e_2, \ldots, e_r)$ and S is $r \times r$ diagonal matrix containing the square roots of the eigenvalues of the correlation matrix $X^T X$ and hence the variances of the Principal Components. The r eigenvectors, i.e. Principal Components of matrix

V, form an orthogonal basis that spans a new vector space, called the feature-space. Therefore, each vector can be projected to a single point in this r-dimensional feature space. However, according to the theory of PCA for highly correlated data, each training set vector can be approximated by taking only the first few k, where, $k \leq r$, Principal Components. This mathematical method is based on the linear transformation of the different variables in principal components which could be assembled in clusters.

4.5 Classification

This book aims at classifying different mood and emotional states. Therefore, several pattern recognition algorithms are applied and the relative performances were evaluated using the confusion matrix [302]. The generic element r_{ij} of the confusion matrix indicates how many times in percentage a pattern belonging to the class i was classified as belonging to the class j. More the confusion matrix is diagonal and better is the classification. The matrix has to be read by columns. The training phase is usually carried out on 80% of the feature dataset while the testing phase to the remaining 20%. 40-fold cross-validation steps are performed in order to obtain unbiased classification results, i.e. to consider Gaussian the classification result distributions, which can be therefore described as mean and standard deviation among the obtained 40 confusion matrices. Several classifiers such as the linear discriminant classifier (LDC), the quadratic discriminant classifier (QDC), a mixture of Gaussian (MOG), the k-nearest neighbor (k-NN), the Kohonen self organizing map (KSOM), the multi-layer perceptron (MLP), and the probabilistic neural network (PNN) were applied to classify features from both the healthy subjects and bipolar patients procedures. Below, the three classifiers which gave the best recognition accuracy are described in detail. Such best classification algorithms are chosen by performing a statistical comparison of the results *a-posteriori* by means of the ANOVA test [303].

4.5.1 Quadratic Discriminant Classifier

The Quadratic Bayes Normal Classifier (also called Quadratic Discriminant Classifier (QDC)) [304] is a statistical based classifier which uses a supervised learning method which determines the parameters based on available knowledge. Assuming that the input training data is a finite set $\Gamma\{(x_1, y_1), \ldots, (x_l, y_l)\}$ containing pairs of observations $x_i \in \mathbb{R}^n$ and corresponding class labels $y_i \in Y$. Basically, statistical classifiers use *discriminant functions* $f_y(x), \forall y \in Y = \{1, 2, \ldots, c\}$ for c classes input dataset and x is a *d-component* feature vector. The classifier is said to assign a feature vector x to class y_i if:

$$f_i(x) > f_j(x) \quad \forall j \neq i \tag{4.63}$$

Thus, the classifier is viewed as a network or machine that computes c discriminant functions and selects the category corresponding to the largest discriminant. A Bayes based classifier is easily and naturally represented in this way. For the general case with risks, $f_i(x) = -R(\alpha_i|x)$, since the maximum discriminant function will then correspond to the minimum conditional risk. For the minimum-error-rate case, it is possible to simplify things further by taking $f_i(x) = P(y_i|x)$, so that the maximum discriminant function corresponds to the maximum posterior probability.

The effect of any decision rule is to divide the feature space into c decision regions, $\Re_1, \ldots, \Re_c$. If $f_i(x) > f_j(x)\ \forall j \neq i$, then x is in region $\Re_1$, and the decision rule calls for us to assign x to f_i. The regions are separated by decision boundaries, surfaces in feature space where ties occur among the largest discriminant functions.

The structure of a Bayes classifier is determined by the conditional densities $P(x|y_i)$ as well as by the prior probabilities, according to the Bayes theorem:

$$P(y_i|x) = \frac{P(x|y_i)P(y_i)}{P(x)} \tag{4.64}$$

where $P(y_i)$ and $P(x)$ are the prior probabilities.

Assuming that the minimum-error-rate classification can be achieved by using the discriminant functions [304]:

$$f_i(x) = \ln P(x|y_i) + \ln P(y_i) \tag{4.65}$$

If the densities $P(x|y_i)$ are multivariate normal, i.e. $P(x|y_i) \sim N(\mu_i, \Sigma_i)$ where μ_i is the *d-component* mean vector and Σ_i is the *d-by-d* covariance matrix:

$$f_i(x) = -\frac{1}{2}(x-\mu_i)^T \Sigma_i^{-1}(x-\mu_i) - \frac{d}{2}\ln 2\pi - \frac{1}{2}\ln|\Sigma_i| + \ln P(y_i) \tag{4.66}$$

where $(x-\mu_i)^T$ is the transpose of $(x-\mu_i)$ matrix. In the general multivariate normal case, the covariance matrices are different for each category. The only term that can be dropped from the above equation is the $\frac{d}{2}\ln 2\pi$ term, and the resulting discriminant functions are inherently quadratic:

$$f_y(x) = x^T \cdot A_y x + b_y x + c_y \quad \forall y \in Y \tag{4.67}$$

which are quadratic with respect to the input vector $x \in \mathbb{R}^n$. The quadratic discriminant function f_y is determined by:

$$A_y = -\frac{1}{2}\Sigma_i^{-1} \tag{4.68}$$

$$b_y = \Sigma_i^{-1}\mu_i \tag{4.69}$$

$$c_y = -\frac{1}{2}\mu_i^T \Sigma_i^{-1}\mu_i - \frac{1}{2}\ln|\Sigma_i| + \ln P(y_i) \tag{4.70}$$

Of course, if the distributions are more complicated, the decision regions can be even more complex, though the same underlying theory holds there too.

4.5.2 k-Nearest Neighborhood

The k-Nearest Neighborhood (k-NN) implementation is performed according to the following steps:

1. In the training phase, the k-NN algorithm just stores the training feature sets together with the labels.
2. In the test phase, the k-NN algorithm calculates the n Euclidean distances between the new feature set and the n features of the whole training feature set as follows:

$$D_i = \sqrt{(p_{i1} - q_1)^2 + \cdots + (p_{in} - q_n)^2} = \sqrt{\sum_{j=1}^{n} (p_{ij} - q_j)^2} \tag{4.71}$$

where $P_i = (p_{i1}, p_{i2}, \ldots, p_{in})$ is ith training feature set, $Q = (q_1, q_2, \ldots, q_n)$ is the new feature test set, n is the number of features.

Afterwards, the k-NN algorithm finds the k training feature sets that have the minimum distance from the new feature set. Among these, m training feature sets belong to the neutral class and $K - m$ belong to the arousal class. The new feature set is supposed to belong to the neutral class if $m > (K - m)$, i.e. $m > \frac{K}{2}$, to the arousal class otherwise.

4.5.3 Multi-layer Perceptron

The Multi-layer perceptron (MLP) [305] is a neural network which has, in the proposed implementation, an integrate-and-fire neuron model for the representation of the relations between input and output values. It is trained by implementing the supervised learning method, i.e. input and output values are specified and the relations between them learnt. Specifically, in the training phase, for each data record, each activation function of the artificial neurons is calculated. The weight w_{ij} of a generic neuron i at time T for the input vector $\overline{f_n^k} = f_{n1}^k, \ldots, f_{nF}^k$ is modified on the basis of the well-established back propagation of the resulting error between the input and the output values. The response of the MLP is a Boolean vector; each element represents the activation function of an output neuron.

4.5.4 Support Vector Machine

Support Vector Machines (SVMs) are classification algorithms that allow robust performances with respect to sparse and noisy data. Basically, they separate a set of binary labeled data with a hyper-plane that is maximizes the distance between

classes. Whether no linear separation is possible, it is possible to use kernel functions that performs a non-linear mapping of the feature space. Let X^j the feature space with $x^j = (x_1^j, \ldots, x_n^j)$ the jth point in n dimensions and $Y^j \in \{-1, +1\}$ the class label associated to each point. Let also define $\phi : X \subseteq \mathbb{R}^n \to F \subseteq \mathbb{R}^N$ be a mapping function from the feature space to the input space F expressed in N dimension. Let us assume that $S = \{(x^1, y^1), \ldots, (x^m, y^m)\}$ a sample of the feature space. The SVM learning algorithm finds a hyper-plane (w, b) such that the quantity:

$$\gamma = \min_i y^i \left\{ \left\langle w, \phi\left(x^i\right) \right\rangle - b \right\} \tag{4.72}$$

is maximized, where w has dimension N, $\langle \cdot, \cdot \rangle$ represents an inner product, b is a real number, and γ is named the *margin*. The quantity $\langle w, \phi(x^i) \rangle - b$ corresponds to the distance between the point x^i and the decision boundary and, if multiplied by the label y^i, it gives a positive value for all correct classifications and a negative value for the incorrect ones. Given a new data point, a label is assigned according to its relationship to the decision boundary, and the corresponding decision function is

$$f(x) = \text{sign}\left(\left\langle w, \phi\left(x^i\right) \right\rangle - b \right) \tag{4.73}$$

Other details can be found in [306–308].

4.6 Point-Process Theory and the Instantaneous Nonlinear Dynamics

Hypothesizing that the ANS responds with different time-varying heartbeat dynamics according to the patient's mood state or to the elicited level of arousal/valence, computational tools able to discern rapid dynamic changes with high time resolution are the best candidates to provide optimal assessments.

For this purpose, standard heart rate variability (HRV) analysis is not recommended since it would require relatively long-time intervals of ECG acquisitions [24, 25] and it would be unable to catch instantaneous variations.

To overcome these limitations, a novel stochastic model of heartbeat dynamics, based on point-process theory, is proposed to instantaneously assess the cardiovascular dynamics. This approach provides a novel paradigm in the literature in the field of psychiatric disorders and affective computing. The core of the model is the definition of the inter-beat probability function to predict the waiting time of the next heartbeat, i.e. the R-wave event, given a linear and nonlinear combination of the previous events. The use of point process theory allows for a fully parametric structure analytically defined at each moment in time, thus allowing to estimate instantaneous measures [30, 212–214] without using any interpolation method.

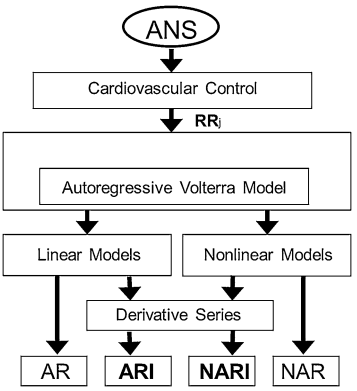

Fig. 4.14 Block diagram of the point process models derivation (from [48])

It has been demonstrated that the Inverse-Gaussian (IG) distribution well characterizes the inter-beat probability function [30] and, in particular, a linear [30, 212] and nonlinear [214] combination of the past events has been taken into account.

The hereby proposed quadratic Nonlinear Autoregressive Integrative (NARI) model improves the achievement of stationarity [309] and consequently improves system identification. This powerful approach further considers an equivalent 3rd-order input–output Wiener–Volterra model, allowing for the instantaneous estimation of the high-order polyspectra [310], such as bispectrum and trispectrum [311, 312]. Therefore, the methodology here proposed is able to instantaneously assess the subject's cardiovascular/autonomic state, even in short-time events (< than 10 seconds), remarkably using only one biosignal, the ECG.

The novel heartbeat model developed has its foundations in the nonlinear system identification theory. The general elements behind the considered model's derivation are shown in Fig. 4.14.

A Nonlinear Autoregressive Model (NAR) Model can be expressed, in a general form, as follows:

$$y(k) = \mathbf{F}\big(y(k-1), y(k-2), \ldots, y(k-M)\big) + \epsilon(k) \tag{4.74}$$

Considering $\epsilon(k)$ as independent, identically distributed Gaussian random variables, such a model can be can be written as a Taylor expansion:

$$\begin{aligned} y(k) = \gamma_0 &+ \sum_{i=1}^{M} \gamma_1(i) y(k-i) \\ &+ \sum_{n=2}^{\infty} \sum_{i_1=1}^{M} \cdots \sum_{i_n=1}^{M} \gamma_n(i_1, \ldots, i_n) \prod_{j=1}^{n} y(k-i_j) + \epsilon(k) \end{aligned} \tag{4.75}$$

The autoregressive structure of Eq. 4.75 allows the system identification with only exact knowledge on output data and with only few assumptions on input data (noise

assumptions). The nonlinear physiological system is represented by using nonlinear kernels up to the second order, i.e. γ_0, $\gamma_1(i)$, and $\gamma_2(i,j)$, taking into account the series of the derivatives in order to improve stationarity [309, 313]. Hence, the general quadratic form of a Nonlinear Autoregressive Integrative (NARI) model becomes:

$$y(k) = y(k-1) + \gamma_0 + \sum_{i=1}^{M} \gamma_1(i)\Delta y(k-i) + \sum_{i=1}^{M}\sum_{j=1}^{M} \gamma_2(i,j)\Delta y(k-i)\Delta y(k-j) + \epsilon(k) \tag{4.76}$$

where $\Delta y(k-i) = y(k-i) - y(k-i-1)$ and $\Delta y(k-j) = y(k-j) - y(k-j-1)$. The quadratic kernel $\gamma_2(i,j)$ is assumed to be symmetric. The extended kernels $\gamma_1'(i)$ and $\gamma_2'(i,j)$ are also defined as:

$$\gamma_1'(i) = \begin{cases} 1, & \text{if } i = 0 \\ -\gamma_1(i), & \text{if } 1 \le i \le M \end{cases} \tag{4.77}$$

$$\gamma_2'(i,j) = \begin{cases} 0, & \text{if } ij = 0 \wedge i + j \le M \\ -\gamma_2(i,j), & \text{if } 1 \le i \le M \wedge 1 \le j \le M \end{cases} \tag{4.78}$$

and link the NARI model to a general input–output form, here defined by using the well-known Wiener–Volterra [314] series:

$$y(k) = h_0 + \sum_{i=1}^{M} h_1(i)\Delta\epsilon(k-i) + \sum_{n=2}^{\infty}\sum_{i_1=1}^{M}\cdots\sum_{i_n=1}^{M} h_n(i_1,\ldots,i_n)\prod_{j=1}^{n}\Delta\epsilon(k-i_j). \tag{4.79}$$

where the functions $h_n(\tau_1,\ldots,\tau_n)$ are the Volterra kernels Mapping a quadratic NARI model to an nth order input–output model [310] allows, after the input–output transformation of the kernels, the evaluation of all the High Order statistics (HOS) of the system, such as the Dynamic Bispectrum and Trispectrum [261, 315]. In the following sections, after the definition of the point-process framework of the heartbeat dynamics, mathematical details on the derivation of the nonlinear kernels as well as the HOS tools are reported.

4.6.1 Point-Process Nonlinear Model of the Heartbeat

The point process framework primarily defines the probability of having a heartbeat event at each moment in time.

Defining $t \in (0, T]$, the observation interval, and $0 \leq u_1 < \cdots < u_k < u_{k+1} < \cdots < u_K \leq T$ the times of the events, it is possible to define $N(t) = \max\{k : u_k \leq t\}$ as the sample path of the associated counting process. Its differential, $dN(t)$, denotes a continuous-time indicator function, where $dN(t) = 1$ when there is an event (the ventricular contraction), or $dN(t) = 0$ otherwise. The left continuous sample path is defined as $\widetilde{N}(t) = \lim_{\tau \to t^-} N(\tau) = \max\{k : u_k < t\}$. Given the R-wave events $\{u_j\}_{j=1}^{J}$ detected from the ECG, $RR_j = u_j - u_{j-1} > 0$ denotes the jth RR interval. Assuming history dependence, the inverse Gaussian probability distribution of the waiting time $t - u_j$ until the next R-wave event is [30]:

$$f\left(t|\mathcal{H}_t, \xi(t)\right) = \left[\frac{\xi_0(t)}{2\pi(t-u_j)^3}\right]^{1/2} \times \exp\left\{-\frac{1}{2}\frac{\xi_0(t)[t-u_j-\mu_{RR}(t,\mathcal{H}_t,\xi(t))]^2}{\mu_{RR}(t,\mathcal{H}_t,\xi(t))^2(t-u_j)}\right\} \tag{4.80}$$

with $j = \widetilde{N}(t)$ the index of the previous R-wave event before time t, $\mathcal{H}_t = (u_j, RR_j, RR_{j-1}, \ldots, RR_{j-M+1})$ is the history of events, $\xi(t)$ the vector of the time-varing parameters, $\mu_{RR}(t, \mathcal{H}_t, \xi(t))$ the first-moment statistic (mean) of the distribution, and $\xi_0(t) > 0$ the shape parameter of the inverse Gaussian distribution. Since $f(t|\mathcal{H}_t, \xi(t))$ indicates the probability of having a beat at time t given that a previous beat has occurred at u_j, $\mu_{RR}(t, \mathcal{H}_t, \xi(t))$ can be interpreted as the expected waiting time until the next event could occur. The use of an inverse Gaussian distribution $f(t|\mathcal{H}_t, \xi(t))$, characterized at each moment in time, is motivated both physiologically (the integrate-and-fire initiating the cardiac contraction [30]) and by goodness-of-fit comparisons [213]. In previous works [212, 213], the instantaneous mean $\mu_{RR}(t, \mathcal{H}_t, \xi(t))$ was expressed as linear and quadratic combination of present and past R–R intervals, based on a nonlinear Volterra–Wiener expansion [214]. Here, the novel NARI formulation is proposed. The instantaneous RR mean is defined as:

$$\begin{aligned}\mu_{RR}\left(t, \mathcal{H}_t, \xi(t)\right) = RR_{\widetilde{N}(t)} + \gamma_0 + \sum_{i=1}^{p}\gamma_1(i,t)(RR_{\widetilde{N}(t)-i} - RR_{\widetilde{N}(t)-i-1}) \\ + \sum_{i=1}^{q}\sum_{j=1}^{q}\gamma_2(i,j,t)(RR_{\widetilde{N}(t)-i} - RR_{\widetilde{N}(t)-i-1}) \\ \times (RR_{\widetilde{N}(t)-j} - RR_{\widetilde{N}(t)-j-1})\end{aligned} \tag{4.81}$$

The coefficients γ_0, $\{\gamma_1(i)\}$, and $\{\gamma_2(i,j)\}$ correspond to the time-varying zero-, first-, second-order NARI coefficients, respectively. Considering the derivative RR interval series improves the achievement of stationarity within the sliding time window W ($W = 70$ seconds) [309]. Since $\mu_{RR}(t, \mathcal{H}_t, \xi(t))$ is defined in continuous time, it is possible to obtain an instantaneous RR mean estimate at a very fine timescale (with an arbitrarily small bin size Δ), which requires no interpolation between the arrival times of two beats. Given the proposed parametric model, all linear and nonlinear indices are defined as a time-varying function of the parameters $\xi(t) = [\xi_0(t), \gamma_0(t), \gamma_1(1,t), \ldots, \gamma_1(p,t), \gamma_2(1,1,t), \ldots, \gamma_2(i,j,t)]$.

The unknown time-varying parameter vector $\xi(t)$ is estimated by means of a local maximum likelihood method [30, 316, 317]. Briefly, given a local observation interval $(t-l, t]$ of duration l, a subset $U_{m:n}$ of the R-wave events is considered. Specifically, $m = N(t-l)+1$ and $n = N(t)$. At each time t, the unknown time-varying parameter vector $\xi(t)$ is found such that the following local log-likelihood is maximized:

$$L\big(\xi(t) \mid U_{m:n}\big) = \sum_{k=m+P-1}^{n-1} w(t-u_{k+1}) \log\Big[f\big(u_{k+1} \mid \mathcal{H}_{u_{k+1}}, \xi(t)\big)\Big] + \log \int_t^{\infty} f\big(\tau \mid \mathcal{H}_t, \xi(t)\big)\, d\tau \tag{4.82}$$

where $w(\tau) = e^{\varpi \tau}$ is an exponential weighting function for the local likelihood. In Eq. 4.82, the latter term accounts for the next, not yet observed, R–R interval (right censoring). A Newton–Raphson procedure is used to maximize the local log-likelihood in Eq. 4.82 and compute the local maximum-likelihood estimate of $\xi(t)$ [316]. Because there is significant overlap between adjacent local likelihood intervals, the Newton–Raphson procedure is started at t with the previous local maximum-likelihood estimate at time $t - \Delta$, where Δ defines the time interval shift to compute the next parameter update.

The model goodness-of-fit is based on the Kolmogorov–Smirnov (KS) test and associated KS statistics (see details in [30, 318]). Autocorrelation plots are considered to test the independence of the model-transformed intervals [30]. Once the order $\{p, q\}$ is determined, the initial NARI coefficients are estimated by the method of least squares [319]. In order to provide reliable results, the HRV processing techniques require uninterrupted series of RR intervals. Nevertheless, peak detection errors and ectopic beats often determine abrupt changes in the R–R interval series that may result in substantial deviations of the HRV indices, especially in changes in the dynamics. In addition, they could potentially bias the statistical outcomes. Therefore, all the actual heartbeat data are pre-processed with a previously developed algorithm [320]. It is based on the point process statistics (local likelihood) and is able to perform a real-time R–R interval error detection and correction. Specifically, the algorithm assesses whether the actual observation is in agreement with the resulting model or if, instead, the alternative hypothesis of an erroneous beat is more likely.

4.6.2 Estimation of the Input–Output Volterra Kernels

The nth-order spectral representations are related to the Volterra series expansion and the Volterra theorem [314]. In functional analysis, a Volterra series denotes a functional expansion of a dynamic, nonlinear, and time-invariant function, widely used in nonlinear physiological modeling [32, 321, 322]. The quadratic NARI model can be linked to the traditional input–output Volterra models by using a specific relationships [310] between the Fourier transforms of the Volterra kernels of order p, $H_p(f_1, \ldots, f_n)$, and the Fourier transforms of the extended NAR kernels, $\Gamma_1'(f_1)$ and $\Gamma_2'(f_1, f_2)$.

In general, a second-order NARI model have to be mapped into a infinite-order input–output Volterra model [310]:

$$\begin{aligned}\sum_{k=\mathrm{mid}(\rho)}^{\rho} \sum_{\sigma \in \sigma_\rho} & H_k(f_{\sigma(1)}, \ldots, f_{\sigma(r)}, \\ & \omega_{\sigma(r+1)} + f_{\sigma(r+2)}, \ldots, f_{\sigma(\rho-1)} + f_{\sigma(\rho)}) \\ & \times \Gamma_1'(f_{\sigma(1)}) \cdots \Gamma_1'(f_{\sigma(r)}) \\ & \times \Gamma_2'(f_{\sigma(r+1)}, f_{\sigma(r+2)}) \cdots \Gamma_2'(f_{\sigma(\rho-1)}, f_{\sigma(\rho)}) = 0 \end{aligned} \tag{4.83}$$

where ρ is a given integer representing the kernel order, $\mathrm{mid}(\rho) = \lceil \rho/2 \rceil$, $r = 2k - \rho$ and σ_ρ is the permutation set of N_ρ. Obviously, there is the need to truncate the series to a reasonable order for actual application. In this book, the cardiovascular activity is modeled with a cubic input–output Volterra by means of the following relationships with the NARI:

$$H_1(f) = \frac{1}{\Gamma_1'(f)} \tag{4.84}$$

$$H_2(f_1, f_2) = -\frac{\Gamma_2'(f_1, f_2)}{\Gamma_1'(f_1)\Gamma_1'(f_2)} H_1(f_1 + f_2) \tag{4.85}$$

$$\begin{aligned} H_3(f_1, f_2, f_3) = & -\frac{1}{6} \sum_{\sigma_3} \frac{\Gamma_2'(f_{\sigma_3(1)}, f_{\sigma_3(2)})}{\Gamma_1'(f_{\sigma_3(1)})\Gamma_1'(f_{\sigma_3(2)})} \\ & \times H_2(f_{\sigma_3(1)} + f_{\sigma_3(2)}, f_{\sigma_3(3)}) \end{aligned} \tag{4.86}$$

Once the vector of the autoregressive time-varing parameters $\xi(t)$ is estimated, it is possible to derive instantaneous quantitative tools such as the nth-order spectral representations. To summarize, the necessary steps are the followings:

1. From $\gamma_n(\cdots)$ find $\gamma_n'(\cdots)$.

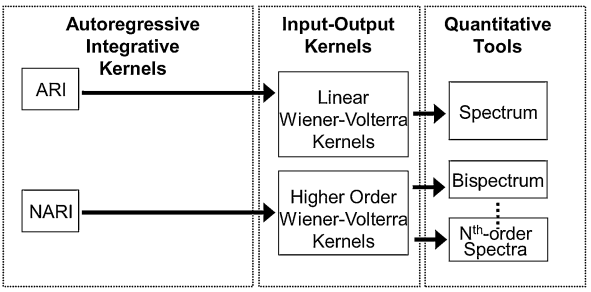

Fig. 4.15 Block diagram of the point process quantitative tools derivation (from [48])

2. Compute the Fourier transforms $\Gamma_n'(\cdots)$ of the kernels $\gamma_n'(\cdots)$.
3. Compute the input–output Volterra kernels $H_k(\cdots)$ from the $\Gamma_n'(\cdots)$ of the autoregressive model.
4. Estimate the nth-order spectra such as the instantaneous spectrum $\mathcal{Q}(f,t)$ and bispectrum $\mathrm{Bis}(f_1, f_2, t)$.

4.6.3 Quantitative Tools: High Order Spectral Analysis

The proposed framework allows for three levels of quantitative characterization of heartbeat dynamics: instantaneous time-domain estimation, linear power spectrum estimation, and higher order spectral representation. The general scheme of such quantitative characterizations is shown in Fig. 4.15. The linear power spectrum estimation reveals the linear mechanisms governing the heartbeat dynamics in the frequency domain. In particular, given the input–output Volterra kernels of the NARI model for the instantaneous R–R interval mean $\mu_{RR}(t, \mathcal{H}_t, \xi(t))$, it is possible to compute the time-varying parametric (linear) autospectrum [323] of the derivative series:

$$\begin{aligned}\mathcal{Q}(f,t) &= S_{xx}(f,t)H_1(f,t)H_1(-f,t) \\ &\quad - \frac{3}{2\pi}\int H_3(f, f_2, -f_2, t)S_{xx}(f_2,t)\,df_2 \end{aligned} \tag{4.87}$$

where $S_{xx}(f,t) = \sigma^2_{RR}$. The time-varying parametric autospectrum of the R–R intervals is given by multiplying its derivative spectrum $\mathcal{Q}(f,t)$ by the quantity $2(1-\cos(\omega))$ [309]. Importantly, previous derivations of the expressions for the autospectrum [214, 215] were possible because the first- and second-order Volterra operators are orthogonal to each other for Gaussian inputs. This property does not hold for orders greater than two [323], and in cubic nonlinear input–output Volterra systems the autospectrum is estimated by considering also the third order term. By integrating Eq. 4.87 in each frequency band, it is possible to compute the index within the very low frequency (VLF = 0.01–0.05 Hz), low frequency (LF = 0.05–0.15 Hz), and high frequency (HF = 0.15–0.5 Hz) ranges.

The higher order spectral representation allows for the consideration of statistics beyond the second order, and phase relations between frequency components otherwise suppressed [312, 324]. Higher order spectra (HOS), also known as polyspectra, are spectral representations of higher order statistics, i.e. moments and cumulants of third order and beyond. HOS can detect deviations from linearity, stationarity or gaussianity. Particular cases of higher order spectra are the third-order spectrum (Bispectrum) and the fourth-order spectrum (Trispectrum) [324], defined from the Volterra kernel coefficients estimated within the point process framework.

4.6.3.1 Dynamical Bispectrum Estimation

Let $H_2(f_1, f_2, t)$ denote the Fourier transform of the second-order Volterra kernel coefficients. The cross-bispectrum (Fourier transform of the third-order moment) is [311, 312]:

$$\text{CrossBis}(f_1, f_2, t) \approx 2\mathcal{S}_{xx}(f_1, t)\mathcal{S}_{xx}(f_2, t)H_2(-f_1, -f_2, t) \tag{4.88}$$

where $\mathcal{S}_{xx}(f, t)$ is the autospectrum of the input (i.e. σ^2_{RR}). Note that the approximation shown in Eq. 4.88 is used since the equality only strictly holds when the input variables are jointly Gaussian. The analytical solution for the bispectrum of a nonlinear system response with stationary, zero-mean Gaussian input is [325]:

$$\begin{aligned}
&\text{Bis}(f_1, f_2, t) \\
&\quad = 2H_2(f_1 + f_2, -f_2, t)H_1(-f_1 - f_2, t)H_1(f_2, t)\mathcal{S}_{xx}(f_1 + f_2, t)\mathcal{S}_{xx}(f_2, t) \\
&\qquad + 2H_2(f_1 + f_2, -f_1, t)H_1(-f_1 - f_2, t)H_1(f_1, t)\mathcal{S}_{xx}(f_1 + f_2, t)\mathcal{S}_{xx}(f_1, t) \\
&\qquad + 2H_2(-f_1, -f_2, t)H_1(f_1, t)H_1(f_2, t)\mathcal{S}_{xx}(f_1, t)\mathcal{S}_{xx}(f_2, t)
\end{aligned} \tag{4.89}$$

Of note, an expression similar to Eq. 4.89 was derived in the early work of Brillinger [326], and later in the appendix of [327]. Given the dynamical bispectrum $\text{Bis}(f_1, f_2, t)$, at each t it is possible to estimate the bispectral features as described in details in Sect. 4.3.2.

4.6.3.2 Dynamical Trispectrum Estimation

Brillinger [328], Billings [314], Priestley [329], and others have demonstrated that there is a closed form solution for homogeneous systems with Gaussian inputs. Thus, the transfer function of a m-order homogeneous system is estimated by the relation:

$$H_m(f_1, \ldots, f_m) = \frac{S_{yx\cdots x}(-f_1, \ldots, -f_m)}{m! S_{xx}(f_1) \cdots S_{xx}(f_m)} \tag{4.90}$$

where the numerator is the $m+1-n$th order crosspolyspectrum between y and x. This result is a generalization of the classical result for the transfer function of a linear system resulting for $m=1$. Therefore, the cross-trispectrum (Fourier transform of the third-order moment) can be estimated as:

$$\mathcal{T}(f_1, f_2, f_3, t) \approx 3!\mathcal{S}_{xx}(f_1, t)\mathcal{S}_{xx}(f_2, t)\mathcal{S}_{xx}(f_3, t)H_3(f_1, f_2, f_3, t) \tag{4.91}$$

Part III
Results

This part of the book reports on the experiments performed by using the wearable monitoring systems to gather data from healthy subjects and patients. Moreover, all the methodologies described in the previous chapters have been applied to these data. All the experimental evidences, which constitute the outcome of this part, are taken as input to drawing the final conclusions and discussions.

Chapter 5
Experimental Evidences on Healthy Subjects and Bipolar Patients

In this chapter, the experimental results on healthy subjects and bipolar patients are reported. The experimental protocols and the methodologies applied were described in detail in Chaps. 3 and 4, respectively.

The main objective of the study applied on healthy subjects was to characterize the autonomic response during a visual emotional elicitation, by using IAPS images, in order to recognize the elicited level of arousal, valence, and self-reported emotions. Results considering long-time series (whole session of image having the same level of arousal/valence) as well as short-time series (for each image) are reported in detail.

Concerning the bipolar patients study, the main goal was to assess the clinical mood state in order to develop an effective decision support system able to automatically recognize mood changes on the basis of ANS information. Long-time and short-time analyses were performed by using the standard analysis and the point-process nonlinear models, respectively.

In general, as the major part of the extracted parameters did not have normal distribution (checked using the Lilliefors test [330]), the results are always expressed in terms of median and median absolute deviation. Accordingly, non-parametric tests are used in order to detect statistically significative differences among the different classes. For instance, comparing more than 2 groups, the Kruskal–Wallis method [331, 332], i.e. a non-parametric one-way analysis of variance, is applied to test the null hypothesis that no difference exists among all groups. Moreover, to test the null hypothesis of no statistical difference between two groups, either the Mann–Whitney or Wilcoxon signed-rank tests is applied instead. Wilcoxon is used for matched pairs.

All of the algorithms were implemented by using *Matlab*© v7.2 endowed with additional toolboxes for pattern recognition (i.e. PRTool) [333] and time series analysis toolbox [334].

G. Valenza, E.P. Scilingo, *Autonomic Nervous System Dynamics for Mood and Emotional-State Recognition*, Series in BioEngineering,
DOI 10.1007/978-3-319-02639-8_5, © Springer International Publishing Switzerland 2014

Table 5.1 Feature sets gathered from standard and nonlinear methods for ANS signals analysis (from [31])

Feature set	Analysis	Signals
Standard	Time domain (MNN, SDNN, RMSSD, pNN50, TINN)	HRV
	Frequency domain (VLF, LF, HF, LF/HF)	HRV
	Frequency domain (Power in 0–0.1 Hz, 0.1–0.2 Hz, 0.2–0.3 Hz, 0.3–0.4 Hz, Central Frequency)	RSP, EDR
	Statistics (SEM, RSPR, MFD, SDFD, MSD, SDSD, SDBA, MAXRSP, MINRSP, DMMRSP, Skewness, Kurtosis)	RSP, EDR
	Statistics (Max Peak, Latency, MAD, MDNV, PNSDAS)	Phasic EDR
	High order spectra (MBI, VBI, MMB, PEB, NBE, NBSE)	HRV, RSP, EDR
Nonlinear methods	Deterministic chaos (m, Δ)	HRV, RSP, EDR
	Recurrence plot (DLE, RR, DET, LAM, TT, RATIO, ENTR, L_{max})	HRV, RSP, EDR
	Detrended fluctuaction analysis (α_1, α_2)	HRV, RSP, EDR

5.1 Results from the Healthy Subjects Study

5.1.1 Effective Arousal and Valence Levels Recognition Through Autonomic Nervous System Dynamics

The first goal of this study is to test the capability of an automatic classifier to discriminate the elicited arousal and valence levels, along with the neutral elicitation. A comparative analysis is performed considering only standard features and standard features joined with others extracted from nonlinear dynamic methods.

Accordingly, 89 standard features and 36 extracted from nonlinear dynamic methods are defined (see Table 5.1). All features are calculated for each neutral session (N) as well as for each arousal session (A_i).

Experimental results from 35 healthy subjects performing the experimental procedure described in Sect. 3.1 are shown in the form of confusion matrices and reported in Tables 5.2, 5.3, 5.4 and 5.5. The principal diagonal represents the percentage of the successful recognition of each class. More specifically, Tables 5.2 and 5.3 show the results of the four classes of different arousal (Arousal1, Arousal2, Arousal3 and Arousal4) along with the neutral one (Neutral), while Tables 5.4 and 5.5 report the results of the four classes of valence (Valence1, Valence2, Valence3 and Valence4) in addition to the neutral class (Neutral). In Tables 5.2 and 5.4 results of the QDC applied to standard features are shown, while in Tables 5.3 and 5.5 classification results are based on features extracted from non-linear dynamic methods.

These tables were obtained through the cross-validation technique, which was an average of 40 confusion matrices calculated on a randomly shuffled dataset.

Table 5.2 Confusion matrix of QDC Classifier for Arousal level recognition based on standard feature set reduced by PCA algorithm to 12 components (from [31])

QDC	Neutral	Arousal1	Arousal2	Arousal3	Arousal4
Neutral	**98.57 ± 1.78**	35.24 ± 16.66	40.47 ± 20.23	22.86 ± 17.83	24.28 ± 19.18
Arousal1	0.36 ± 1.09	**37.14 ± 17.44**	6.67 ± 8.98	3.33 ± 6.15	6.19 ± 8.94
Arousal2	0.36 ± 1.09	13.81 ± 13.25	**22.38 ± 18.26**	27.62 ± 20.86	25.71 ± 18.53
Arousal3	0.12 ± 0.65	6.67 ± 8.98	20.48 ± 20.09	**20.95 ± 19.40**	24.29 ± 18.05
Arousal4	0.59 ± 1.35	7.14 ± 11.10	10.00 ± 12.53	25.24 ± 23.03	**19.52 ± 18.18**

Table 5.3 Confusion matrix of QDC Classifier for Arousal level recognition based on features extracted from nonlinear methods reduced by PCA algorithm to 7 components (from [31])

QDC	Neutral	Arousal1	Arousal2	Arousal3	Arousal4
Neutral	**100.00 ± 0.00**	0.00 ± 0.00	0.00 ± 0.00	0.00 ± 0.00	0.00 ± 0.00
Arousal1	0.00 ± 0.00	**100.00 ± 0.00**	0.00 ± 0.00	0.00 ± 0.00	0.00 ± 0.00
Arousal2	0.00 ± 0.00	0.00 ± 0.00	**92.86 ± 10.73**	0.00 ± 0.00	4.64 ± 8.79
Arousal3	0.00 ± 0.00	0.00 ± 0.00	5.36 ± 8.37	**82.86 ± 14.17**	19.28 ± 16.67
Arousal4	0.00 ± 0.00	0.00 ± 0.00	1.78 ± 4.78	17.14 ± 14.17	**76.07 ± 16.93**

Table 5.4 Confusion matrix of QDC Classifier for Valence level recognition based on standard feature set reduced by PCA algorithm to 12 components (from [31])

QDC	Neutral	Valence1	Valence2	Valence3	Valence4
Neutral	**28.57 ± 18.54**	41.43 ± 22.66	18.57 ± 16.77	27.86 ± 15.70	22.14 ± 18.81
Valence1	27.14 ± 14.58	**12.86 ± 14.58**	5.00 ± 8.39	16.43 ± 19.81	3.57 ± 7.86
Valence2	9.28 ± 14.11	4.29 ± 11.45	**22.86 ± 12.61**	14.28 ± 13.11	17.14 ± 12.78
Valence3	27.86 ± 15.70	34.28 ± 24.26	15.00 ± 12.67	**28.57 ± 17.95**	28.57 ± 15.37
Valence4	7.14 ± 8.67	7.14 ± 10.86	38.57 ± 16.77	12.86 ± 13.03	**28.57 ± 14.66**

Table 5.5 Confusion matrix of QDC Classifier for Valence level recognition based on features extracted from nonlinear methods reduced by PCA algorithm to 13 components (from [31])

QDC	Neutral	Valence1	Valence2	Valence3	Valence4
Neutral	**96.79 ± 7.58**	3.93 ± 6.46	0.00 ± 0.00	0.00 ± 0.00	0.00 ± 0.00
Valence1	3.21 ± 7.58	**96.07 ± 6.46**	0.00 ± 0.00	0.00 ± 0.00	0.00 ± 0.00
Valence2	0.00 ± 0.00	0.00 ± 0.00	**87.14 ± 11.11**	0.00 ± 0.00	18.57 ± 11.30
Valence3	0.00 ± 0.00	0.00 ± 0.00	0.00 ± 0.00	**100.00 ± 0.00**	0.00 ± 0.00
Valence4	0.00 ± 0.00	0.00 ± 0.00	12.86 ± 11.11	0.00 ± 0.00	**81.43 ± 11.30**

Table 5.6 Median and absolute median deviation of ApEn and DLE and SDNN across all the sessions (from [46])

Session	ApEn	λ	SDNN
Neutral	0.6146 ± 0.1469	0.0014 ± 0.2061	0.0423 ± 0.0523
Arousal1	0.5318 ± 0.1349	-0.0919 ± 0.0891	0.0406 ± 0.0728
Neutral	0.6308 ± 0.0816	0.0038 ± 0.1894	0.0390 ± 0.0494
Arousal2	0.5613 ± 0.1110	-0.1072 ± 0.0719	0.0404 ± 0.1972
Neutral	0.5511 ± 0.1020	0.0045 ± 0.2217	0.0434 ± 0.0460
Arousal3	0.5330 ± 0.1089	-0.0970 ± 0.0798	0.0361 ± 0.1279
Neutral	0.5822 ± 0.1013	0.0041 ± 0.1482	0.0422 ± 0.0744
Arousal4	0.5128 ± 0.1120	-0.1259 ± 0.0742	0.0407 ± 0.2138

Each element of the principal diagonal of all matrices is reported as mean value and standard deviation of the classification result. All the other elements out of the principal diagonal represent the error of classification.

Each principal component, obtained by applying the PCA algorithm to the feature sets, accounts for a given amount of the total variance. The reduction process was stopped when the cumulative variance reached 95%. Therefore the number of principal components was different for standard dataset and dataset from nonlinear techniques and for arousal and valence (see captions of the tables for further details).

5.1.2 Approximate Entropy and Dominant Lyapunov Exponent Analysis on Heart Rate Variability

Given the crucial role of nonlinear dynamics in characterizing the ANS response during emotional elicitation, the complexity of HRV was studied in detail through Approximate Entropy (ApEn) and Dominant Lyapunov Exponent (DLE) analysis. Since, in the computation of the ApEn (see Chap. 4), the threshold is proportional to the standard deviation of the RR intervals, changes in ApEn could be related to changes in the standard deviation of the RR time series (SDNN) and not to the complexity of the signal [335]. Therefore, a statistical analysis on the SDNN changes throughout the sessions is provided as well.

In Tables 5.6, 5.7 and 5.8 the results from ApEn, DLE (i.e. λ) and SDNN calculation are shown in terms of median and median absolute deviation relative to each session. Firstly, the Kruskal–Wallis test is applied among all the neutral classes together and among all the arousal classes. In both cases, for all the considered features, the null hypothesis cannot be rejected implying that all the neutral classes belong to the same population as well as for the arousal classes ($p\text{-}value > 0.05$). Considering all the sessions, no statistical difference among all the sessions is obtained for the SDNN, while the null hypothesis for both ApEn and λ can be rejected with ($p\text{-}value < 0.05$). This means that the SDNN values are undistinguish-

Table 5.7 Number of subjects out of 35 characterized by DLE (adapted from [46])

Session	$DLE > 0$	$DLE < 0$
Neutral	**25 (71%)**	10 (29%)
Arousal1	2 (6%)	**33 (94%)**
Neutral	**22 (63%)**	13 (37%)
Arousal2	3 (9%)	**32 (91%)**
Neutral	**23 (66%)**	12 (34%)
Arousal3	5 (14%)	**30 (86%)**
Neutral	**25 (71%)**	10 (29%)
Arousal4	1 (3%)	**34 (97%)**

Bold indicates the highest values

able through all the sessions (ensuring the reliability of the ApEn findings) while at least one session is statistically different from the other ones in both ApEn and λ population.

Table 5.8 Results from the statistical analysis applying Kruskal–Wallis (K–W) and Rank-Sum (R-S) tests for the ApEn and DLE analysis on HRV (from [46])

Test	Features	Sessions	p-value	Notes
K–W	ApEn	All neutral	$p > 0.05$	No statistical difference among the neutral sessions
K–W	ApEn	All arousal	$p > 0.05$	No statistical difference among the arousal sessions
K–W	λ	All neutral	$p > 0.05$	No statistical difference among the neutral sessions
K–W	λ	All arousal	$p > 0.05$	No statistical difference among the arousal sessions
K–W	SDNN	All neutral	$p > 0.05$	No statistical difference among the neutral sessions
K–W	SDNN	All arousal	$p > 0.05$	No statistical difference among the arousal sessions
K–W	ApEn	All	$p < 0.05$	At least one session is statistically different from the other ones
K–W	λ	All	$p < 0.05$	At least one session is statistically different from the other ones
K–W	SDNN	All	$p > 0.05$	Features undistinguishable through all the sessions
R-S	ApEn	All neutral vs All arousal	$p < 0.01$	Statistical difference between neutral and arousal sessions
R-S	λ	All neutral vs All arousal	$p < 0.01$	Statistical difference between neutral and arousal sessions
R-S	SDNN	All neutral vs All arousal	$p > 0.05$	No statistical difference between neutral and arousal sessions

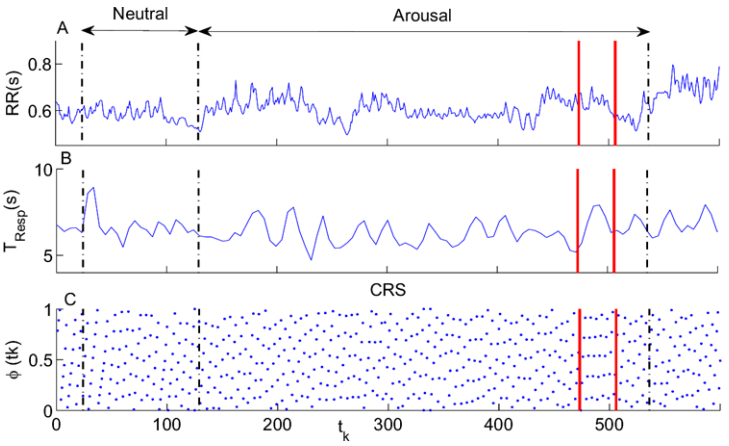

Fig. 5.1 Transient epochs within the data of a representative subject. The periods of cardiac acts (RR) and the respiratory cycles are shown in (**A**) and (**B**), respectively. Several phase locking events occurred. Here only the ratio 1:5, held for 30 heartbeats, was shown by way of illustration (**C**). t_k is the time where the R-peak in the kth heartbeat occurs (from [36])

Finally, the null hypothesis is tested between the two groups including all the neutral and arousal classes, respectively, using the Wilcoxon signed-rank test. Even in this case, the null hypothesis is rejected for both ApEn and λ ($p\text{-}value < 0.01$).

According to DLE findings, the median ApEn values tended to reduce in arousal sessions. Moreover, Table 5.7 reports on the number of subjects in which positive and negative DLE were found. The ApEn and DLE calculations are performed for each subject for the whole duration of each session.

5.1.3 Cardio-Respiratory Synchronization Analysis

Regarding the cardio-respiratory synchronization (CRS) analysis, Fig. 5.1 reports transient epochs within the data a representative subject which confirms the existence of synchronization. The periods of cardiac acts (RR) and the respiratory signal are shown in (A) and (B), respectively. In this Figure only the interval presenting the phase locking ratio 1:5 is marked by way of illustration, but other phase locking events occur during the arousal phase. It was chosen this ratio to be shown because it represents the longest (30 heartbeats) phase locking ratio over time and it was most visually recognizable in the CRS (C). Figure 5.2 reports two CRSs referring to the first neutral session, i.e. the upper figure, and the first arousal session, i.e. the lower figure. Concerning the cardio-respiratory synchronization analysis, about 70% of synchronization was found during the arousal elicitation sessions compared with 54% during the neutral sessions. The exact percentages, in terms of median and median deviation, for each session are reported in the column *%Synchro* of Table 5.9. In addition, in the same Table the values of medians and median deviations

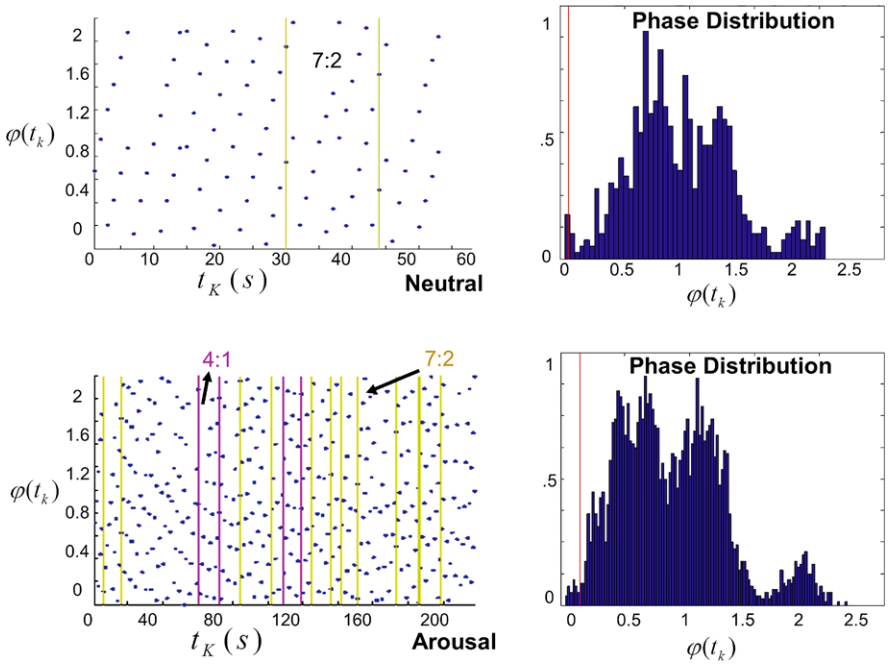

Fig. 5.2 The *upper* figure reports the CRS for the first neutral session, while the *lower* figure refers to the first arousal session of a subject. *Yellow vertical lines* delimit the transients where 7:2 synchronization occurs while the *magenta vertical lines* show the regions where 4:1 synchronization takes place (from [36])

of the standard features extracted from the HRV signal along with the LF/HF are reported. A detailed statistical analysis is performed on all the features extracted from cardiac and respiratory signals and results are reported in Table 5.10.

Applying the Kruskal–Wallis test to the standard features from HRV, i.e. MeanRR, SDRR, RMSSD, and pNN50, no statistical difference is obtained among all sessions, while the null hypothesis for both LF/HF ratios and *%Synchro* can be rejected with $p < 0.001$ and $p < 0.05$, respectively. This means that while standard features are undistinguishable through all sessions, the sympatho-vagal balance and the percentage of synchronization are features, which allow us to say that at least one session is statistically different from all of the other ones. In order to better refine the analysis for these two specific features, the null hypothesis is tested among all the neutral classes together first and among all the arousal classes afterwards. In both cases, the null hypothesis cannot be rejected implying that all neutral classes belong to the same population as well as for the arousal classes. Finally, the null hypothesis is tested between the two groups including all the neutral and arousal classes, respectively. There, the Mann–Whitney test, which is a nonparametric alternative for the t-test is used. The null hypothesis is rejected for both LF/HF ($p < 0.001$) and *%Synchro* ($p < 0.01$).

Table 5.9 Median and median absolute deviations of the features extracted throughout the sessions for the cardio-respiratory synchronization analysis (from [36])

Session	MeanRR	SDRR	RMSSD	pNN50	LF/HF	%Synchro
Neutral	0.77 ± 0.10	0.04 ± 0.05	0.04 ± 0.08	0.16 ± 0.15	3.68 ± 2.08	54.69 ± 24.45
Arousal1	0.79 ± 0.11	0.04 ± 0.07	0.04 ± 0.11	0.15 ± 0.14	4.28 ± 1.24	65.58 ± 21.41
Neutral	0.78 ± 0.10	0.04 ± 0.05	0.04 ± 0.07	0.13 ± 0.14	4.06 ± 1.84	59.02 ± 19.77
Arousal2	0.79 ± 0.16	0.04 ± 0.20	0.04 ± 0.28	0.16 ± 0.15	4.30 ± 1.01	70.48 ± 19.89
Neutral	0.78 ± 0.11	0.04 ± 0.05	0.04 ± 0.07	0.16 ± 0.12	4.00 ± 1.82	56.72 ± 22.58
Arousal3	0.80 ± 0.18	0.04 ± 0.13	0.03 ± 0.17	0.14 ± 0.14	4.31 ± 0.93	67.72 ± 24.59
Neutral	0.77 ± 0.11	0.04 ± 0.07	0.04 ± 0.11	0.17 ± 0.14	4.17 ± 1.79	54.05 ± 21.63
Arousal4	0.81 ± 0.17	0.04 ± 0.21	0.04 ± 0.30	0.18 ± 0.16	4.30 ± 0.65	68.31 ± 20.87

Table 5.10 Results from the statistical analysis applying Kruskal–Wallis (K–W) and Mann–Withney (M–W) tests for the cardio-respiratory synchronization analysis (from [36])

Test	Features	Sessions	p-value	Notes
K–W	MeanRR, SDRR	All	$p > 0.05$	Features undistinguishable through all the sessions
K–W	RMSSD, pNN50	All	$p > 0.05$	Features undistinguishable through all the sessions
K–W	LF/HF	All	$p < 0.001$	At least one session is different from the other ones
K–W	%Synchro	All	$p < 0.05$	At least one session is different from the other ones
K–W	LF/HF	All neutral	$p > 0.05$	No difference among the neutral sessions
K–W	LF/HF	All arousal	$p > 0.05$	No difference among the arousal sessions
K–W	%Synchro	All neutral	$p > 0.05$	No difference among the neutral sessions
K–W	%Synchro	All arousal	$p > 0.05$	No difference among the arousal sessions
M–W	LF/HF	All neutral vs All arousal	$p < 0.001$	Difference between neutral and arousal sessions
M–W	%Synchro	All neutral vs All arousal	$p < 0.01$	Difference between neutral and arousal sessions

5.1.4 Using Cardio-Respiratory Synchronization Information for Emotion Recognition

Experimental results on emotion recognition (see Sect. 5.1.1) reports on the capability of the classifier to discriminate the five different arousal and five different

Table 5.11 Comparison of the arousal levels recognition accuracy for the feature set α and the proposed feature set β (from [38] "© Institute of Physics and Engineering in Medicine. Published on behalf of IPEM by IOP Publishing Ltd. All rights reserved.")

QDC	Dataset	N	A1	A2	A3	A4
N	α	$\mathbf{100 \pm 0.0}$	0.0 ± 0.0	0.0 ± 0.0	0.0 ± 0.0	0.0 ± 0.0
	β	$\mathbf{100 \pm 0.0}$	5.4 ± 9.6	1.4 ± 5.7	4.9 ± 11.1	8.1 ± 13.1
A1	α	0.0 ± 0.0	$\mathbf{100 \pm 0.0}$	0.0 ± 0.0	0.0 ± 0.0	0.0 ± 0.0
	β	0.0 ± 0.0	$\mathbf{94.6 \pm 9.6}$	0.0 ± 0.0	0.0 ± 0.0	0.0 ± 0.0
A2	α	0.0 ± 0.0	0.0 ± 0.0	$\mathbf{92.9 \pm 10.7}$	0.0 ± 0.0	4.6 ± 8.8
	β	0.0 ± 0.0	0.0 ± 0.0	$\mathbf{98.6 \pm 5.7}$	0.0 ± 0.0	0.0 ± 0.0
A3	α	0.0 ± 0.0	0.0 ± 0.0	5.3 ± 8.4	$\mathbf{82.9 \pm 14.2}$	19.3 ± 16.7
	β	0.0 ± 0.0	0.0 ± 0.0	0.0 ± 0.0	$\mathbf{95.1 \pm 11.1}$	0.0 ± 0.0
A4	α	0.0 ± 0.0	0.0 ± 0.0	1.8 ± 4.8	17.1 ± 14.2	$\mathbf{76.1 \pm 16.9}$
	β	0.0 ± 0.0	0.0 ± 0.0	0.0 ± 0.0	0.0 ± 0.0	$\mathbf{91.9 \pm 13.1}$

valence classes. Relying on the CMA model of emotion [89], in fact, it is possible to associate a certain emotion to a specific combination of arousal and valence levels (see an example in Fig. 2.1). Therefore, in further applications, given a certain elicitation it would be possible to evaluate the proper arousal and valence levels whose combination results in one of the 25 different regions of the CMA.

Given the significant role of Cardio-Respiratory (CR) coupling (see Sect. 5.1.3) during the emotional stimulation, it is expected to increase the accuracy of the emotion recognition system described in Sect. 5.1.1 [31] using CR information.

The features set obtained by means of monovariate analysis is only taken as reference and labeled as α. The proposed feature set, which is comprised of the union set of α and the features coming from bivariate analysis (CRS) was labeled as β. After the feature extraction phase, the PCA algorithm is applied to each dataset. The reduction process is stopped when the cumulative variance reached 95%. The discrimination results are shown in Tables 5.11 and 5.12 for the arousal and the valence, respectively. The QDC performances are expressed in form of confusion matrix calculated after 40 steps of cross-fold validation. The neutral elicitation is labeled as N, the arousal levels as A_i with $i = \{1, 2, 3, 4\}$, and the valence levels as V_i with $i = \{1, 2, 3, 4\}$. It is straightforward to notice that the inclusion of the CR features improves the classification accuracy in both the arousal and valence recognition problem.

Table 5.12 Comparison of the valence levels recognition accuracy for the feature set α and the proposed feature set β (from [38] "© Institute of Physics and Engineering in Medicine. Published on behalf of IPEM by IOP Publishing Ltd. All rights reserved.")

QDC	Dataset	N	V1	V2	V3	V4
N	α	$\mathbf{96.8 \pm 7.5}$	3.9±6.4	0.0 ± 0.0	0.0 ± 0.0	0.0 ± 0.0
	β	$\mathbf{100 \pm 0.0}$	3.1 ± 4.5	0.0 ± 0.0	0.0 ± 0.0	0.0 ± 0.0
V1	α	3.2± 7.5	$\mathbf{96.1 \pm 6.4}$	0.0 ± 0.0	0.0 ± 0.0	0.0 ± 0.0
	β	0.0 ± 0.0	$\mathbf{94.7 \pm 4.5}$	0.0 ± 0.0	0.0 ± 0.0	0.0 ± 0.0
V2	α	0.0 ± 0.0	0.0 ± 0.0	$\mathbf{87.1 \pm 11.1}$	0.0 ± 0.0	18.6 ± 11.2
	β	0.0 ± 0.0	2.2 ± 4.5	$\mathbf{91.7 \pm 9.8}$	0.0 ± 0.0	0.0 ± 0.0
V3	α	0.0 ± 0.0	0.0 ± 0.0	0.0 ± 0.0	$\mathbf{100 \pm 0.0}$	0.0 ± 0.0
	β	0.0 ± 0.0	0.0 ± 0.0	2.0 ± 9.8	$\mathbf{90.1 \pm 4.7}$	5.1 ± 9.8
V4	α	0.0 ± 0.0	0.0 ± 0.0	12.9 ± 11.1	0.0 ± 0.0	$\mathbf{81.4 \pm 11.2}$
	β	0.0 ± 0.0	0.0 ± 0.0	6.3 ± 9.8	8.9 ± 4.7	$\mathbf{94.9 \pm 9.8}$

5.1.5 Instantaneous Bispectral Characterization of the Autonomic Nervous System Through Point-Process Nonlinear Models

In this section, the developed point-process NARI model is validated in data gathered from 10 healthy subjects undergoing a fast Tilt-Table protocol [47], i.e. postural changes. The study, fully described in [30], was conducted at the Massachusetts Institute of Technology (MIT) General Clinical Research Center (GCRC) and was approved by the MIT Institutional Review Board and the GCRC Scientific Advisory Committee. After preprocessing the data with a point-process based R–R interval (RR) error detection and correction algorithm [336], a preliminary model selection analysis is also conducted for the experimental datasets. Specifically, using the first 5-min RR recordings, AIC analysis indicated $6 \leq p \leq 8$ and $1 \leq q \leq 2$ as optimal orders. A representative tracking result is shown in Fig. 5.3, and its respective KS plots and Autocorrelation plots are illustrated in Fig. 5.4 for the nonlinear model. Almost all the obtained KS plots were inside the boundaries with small KS distances (i.e. 0.0811 ± 0.0532). The outcomes from an established nonlinearity test [337] further validated that the nonlinear terms estimated by our model are not a result of an over-fitting identification.

Once the optimal model has been established, the linear and nonlinear indices are evaluated for all subjects and averaged the instantaneous (5 ms resolution) identification indices both within each "rest" and "tilt" epochs, and among all subjects. The statistical difference between "rest" and "tilt" are expressed in terms of p-value as computed by Rank-Sum test [338]. The results are shown in Table 5.13. It is straightforward to notice that in terms of statistical difference between the rest and tilt conditions, the bispectral features provide significative results in spite of the discrimination obtained using the spectral ones.

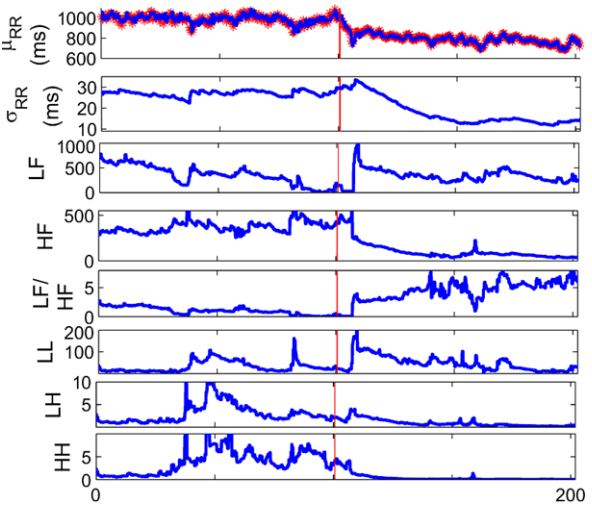

Fig. 5.3 Instantaneous heartbeat statistics computed from a representative subject (N. 1) of the Tilt-Table protocol using a NARI model. The estimated $\mu_{RR}(t)$ is superimposed on the recorded R–R series. Instantaneous heartbeat Power spectra in Low frequency (LF), High frequency (HF) and the sympatho-vagal balance from a representative subject of the Tilt-Table protocol are shown along with instantaneous heartbeat Bispectral statistics (from [47])

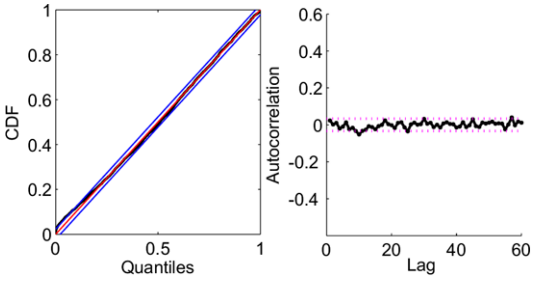

Fig. 5.4 KS plot (**left**) and Autocorrelation plot (**right**) from a representative subject of the Tilt-Table protocol. The *dashed lines* in all plots indicate the 95% confidence bounds (from [47])

5.1.6 Instantaneous Emotional Assessment Through Nonlinear Point-Process Models

The emotion recognition system proposed in the previous sections, although effective, requires relatively long-time series of multivariate records. Reducing such a

Table 5.13 Results from the Tilt-Table experimental dataset, i.e. tilt (from [47])

Statistical index	Rest	Tilt-Table	p-value
μ_{RR} (ms)	884.86 ± 96.82	777.21 ± 55.13	**0.003849**
σ_{RR} (ms)	21.54 ± 7.98	16.51 ± 4.41	0.068878
Power LF (ms^2)	322.71 ± 258.96	322.27 ± 165.28	0.558337
Power HF (ms^2)	192.67 ± 131.14	122.36 ± 65.01	0.141238
PowerBal.	1.35 ± 0.83	1.23 ± 1.14	0.739734
LL (10^6)	24.70 ± 18.51	30.04 ± 14.07	0.704275
LH (10^6)	168.90 ± 126.80	73.13 ± 22.52	0.055603
HH (10^6)	441.00 ± 378.98	172.17 ± 129.92	**0.028176**

dimensionality would bring beneficial results in computational costs and number of sensors needed. Moreover, these methods are not able to provide accurate characterizations in short-time series (e.g., for each image showed for less than 10 seconds).

To overcome these limitations, the novel personalized probabilistic framework based on the point-process theory (see Chap. 4) was applied to characterize the instantaneous emotional state of an healthy subject through analysis and modeling of heartbeat dynamics exclusively. Due to the intrinsic non-linearity and non-stationariety of the RR intervals, a specific nonlinear point-process model was developed. Features from an equivalent cubic input–output model were extracted from the instantaneous spectrum, and bispectrum of the considered RR intervals, and given as input to a support vector machine for classification [339].

The ECG signal is analyzed off-line to extract the RR intervals [24], then further processed to correct for erroneous and ectopic beats with a previously developed algorithm [320]. First, the presence of nonlinear behaviors in the heartbeat series is tested by using a well-established time-domain test based on high-order statistics [337]. The null hypothesis assumes that the time series are generated by a linear system. The number of laps is set to $M = 8$, and a total of 500 bootstrap replications for every test. Experimental results are shown in Table 5.14.

The nonlinearity test gave significant results ($p < 0.05$) on 27 out of 30 subjects (see Table 5.14). In light of this result, a quadratic Nonlinear Autoregressive Integrative (NARI) model was applied. Its main novelty relies on the possibility of linking a regression on the derivative RR series based on an Inverse Gaussian (IG) probability structure [30, 212, 213] to an equivalent nth-order input–output Wiener–Volterra Model based on the Wiener-Volterra representation [32, 314], allowing for the estimation of the nth-order polyspectra of the signal [310]. For this analysis, up to the third-order input–output nonlinearities were considered to obtain the instantaneous estimation of the dynamic bispectrum and trispectrum [311, 312]. After a transformation from the autoregressive to the input–output domain, from the linear and nonlinear terms of the NARI representation it is possible to extract crucial cardiovascular instantaneous information related to the second-order (i.e., spectral) and third-order (i.e., bispectral) statistics, respectively. Indices from a representative subject are shown in Fig. 5.5. Importantly, the NARI model as applied to the considered data provides excellent results in terms of goodness-of-fit, with KS distances never above 0.056 (see Table 5.14), and the independence test verified for all subjects.

Concerning the emotional pattern recognition, a two-class problem is considered for the arousal, valence and self-reported emotion: Low–Medium (L–M) and Medium–High (M–H). The arousal classification was linked to the capability of the point-process NARI methodology in distinguishing the L–M arousal stimuli from the M–H ones, with the neutral sessions associated to the L–M arousal class. Regarding valence, the L–M was distinguished from the M–H valence regardless the images belonging to the neutral classes. This choice is justified by the fact that the neutral images can be equally associated to the L–M or M–H valence classes. For the self-reported emotions, labels given by the self-assessment manikin (SAM) report are used. After the visual elicitation, in fact, each subject is asked to fill out a SAM

Table 5.14 Experimental results from the point-process NARI model: KS statistics, nonlinearity test, and accuracy of classification of the SVM (in percentage)

Subjects	KS dist.	p-value	Linear → Nonlinear		Linear → Nonlinear		Linear → Nonlinear	
1	$<10^{-6}$	0.0362	65.45 → 63.64		78.45 → 78.46	√	84.37 → 81.25	
2	$<10^{-6}$	0.0397	73.13 → 74.63	√	83.61 → 85.25	√	79.03 → 85.48	√
3	$<10^{-6}$	0.0321	66.15 → 58.46		87.69 → 92.31	√	75.00 → 73.44	
4	<0.01	0.0372	47.83 → 60.87	√	80.00 → 90.77	√	54.69 → 68.75	√
5	<0.05	0.0250	70.91 → 69.09		89.23 → 95.38	√	70.31 → 60.94	
6	<0.005	0.0470	70.31 → 67.19		79.69 → 90.62	√	80.95 → 87.30	√
7	<0.05	0.0331	70.18 → 64.91		94.74 → 98.25	√	72.13 → 78.69	√
8	<0.002	0.0335	56.52 → 67.39	√	85.94 → 92.19	√	84.13 → 82.54	
9	<0.05	0.0474	59.57 → 53.19		61.54 → 67.69	√	62.50 → 75.00	√
10	$<10^{-6}$	0.0302	67.74 → 61.29		87.30 → 85.71		78.69 → 70.49	
11	<0.03	0.0311	73.21 → 76.78	√	81.25 → 90.62	√	79.36 → 80.95	√
12	<0.02	0.0216	64.62 → 63.08		79.69 → 87.50	√	68.25 → 66.67	
13	<0.004	0.0306	53.23 → 72.58	√	87.69 → 81.54		57.81 → 75.00	√
14	<0.002	0.0463	81.36 → 83.05	√	76.92 → 84.62	√	82.81 → 87.50	√
15	<0.004	0.0130	72.73 → 67.27		87.69 → 86.15		73.44 → 75.00	√
16	<0.008	0.0168	51.79 → 66.07	√	73.85 → 60.00		65.62 → 78.12	√
17	>0.05	0.0464	80.65 → 82.26	√	91.80 → 88.52		86.88 → 78.69	
18	<0.03	0.0298	70.59 → 67.65		78.46 → 73.85		79.69 → 90.62	√
19	$<10^{-6}$	0.0357	68.33 → 61.67		93.85 → 80.00		70.31 → 75.00	√
20	<0.002	0.0514	65.71 → 67.14	√	73.84 → 76.92	√	60.94 → 70.31	√
21	<0.01	0.0550	62.50 → 71.43	√	76.92 → 93.85	√	87.50 → 90.62	√
22	>0.05	0.0309	62.72 → 72.88	√	96.92 → 92.31		75.00 → 73.44	
23	<0.05	0.0395	92.16 → 84.31		78.46 → 75.38		96.87 → 92.19	
24	<0.01	0.0427	78.57 → 71.43		83.08 → 87.69	√	78.12 → 79.69	√
25	<0.05	0.0455	61.02 → 64.41	√	68.75 → 76.56	√	69.84 → 73.02	√
26	$<10^{-6}$	0.0558	61.67 → 66.67	√	58.06 → 72.58	√	58.06 → 74.19	√
27	>0.05	0.0315	76.81 → 72.46		90.77 → 80.00		85.94 → 82.81	
28	$<10^{-6}$	0.0494	79.63 → 74.07		84.37 → 75.00		87.30 → 82.54	
29	$<10^{-6}$	0.0463	73.44 → 70.31		78.12 → 78.12	√	66.67 → 73.02	√
30	$<10^{-6}$	0.0347	55.88 → 63.23	√	57.81 → 67.19	√	59.68 → 74.19	√

test associating either a positive or a negative emotion to each of the seen images. During this phase, the images were presented in a different randomized order with respect to the previous sequence. For each of the three mentioned classifications, 80% of the available data was used for training the pattern recognition algorithm, whereas the remaining 20% was associated to the test set. 40-fold cross-validation steps were performed in order to obtain unbiased, Gaussian distributed classification

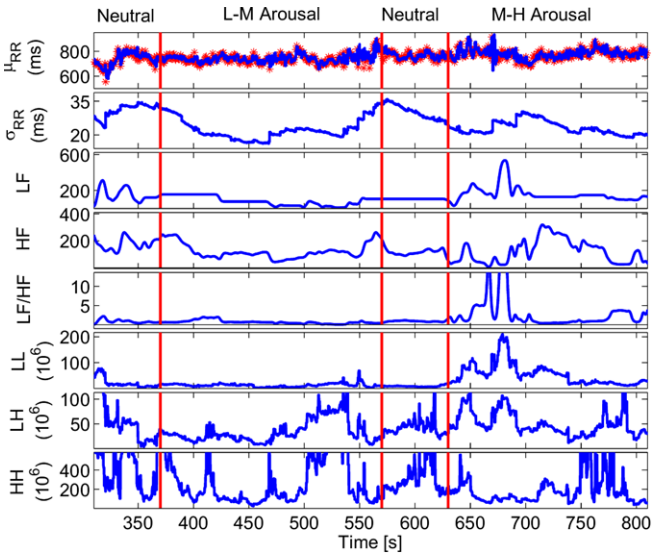

Fig. 5.5 Instantaneous HRV indices computed from a representative subject (N. 12) using the proposed NARI model during the passive emotional elicitation (two neutral sessions alternated to a L–M and a M–H arousal sessions). In the *first panel*, the estimated $\mu_{RR}(t, \mathcal{H}_t, \xi(t))$ is superimposed on the recorded R–R series. Below, the instantaneous heartbeat Power spectra evaluated in Low frequency (LF) and in High frequency (HF), the sympatho-vagal balance (LF/HF) and several bispectral statistics are reported

results. Features are classified using a well-known Support Vector Machine [340]. Results are summarized based on recognition accuracy, i.e. the percentage of correct classification among all classes.

First, five linear-derived features were used in the SVM classifier: the mean and standard deviation of the IG distribution (corresponding to the instantaneous point process definitions of mean and standard deviation of the RR intervals [30]), the power in the low frequency (LF) band, the power in the high frequency (HF) band, and the LF/HF ratio. Then, nonlinear features derived from the instantaneous bispectral analysis, namely the mean and the standard deviation of the bispectral invariants, mean magnitude, phase entropy, normalized bispectral entropy, normalized bispectral squared entropy, sum of logarithmic bispectral amplitudes, and nonlinear sympatho-vagal interactions are added to the linear-derived feature set for further classification. The recognition accuracy of the short-term positive-negative emotions improves with the use of the nonlinear measures in 14 cases, with $> 60\%$ of successfully recognized samples for all of the subjects and a maximum of 84% for subject 23.

Concerning the L–M and M–H arousal classification, the recognition accuracy of the short-term emotional data improves in 19 cases, with $> 66\%$ of successfully recognized samples for all of the subjects and a maximum of 98% for subject 7. Finally, the L–M and M–H valence classification the recognition accuracy of the short-term emotional data is improved in 19 cases, with $> 60\%$ of successfully rec-

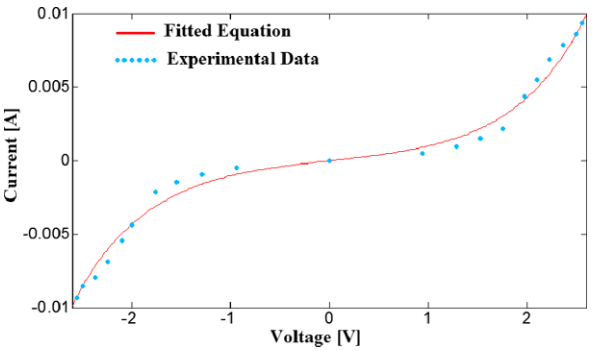

Fig. 5.6 Fitting of Butler–Volmer equation (from [22])

Table 5.15 Butler–Volmer coefficients (from [22])

α	j_0 (A/m^2)	R_T ($\Omega \times$ m^2)
3.022×10^{-2}	3.639×10^{-4}	2358.78

ognized samples for all of the subjects and a maximum of 92% for subject 23 (see Table 5.14).

5.1.7 Electrodermal Response Analysis and Sensorized Glove Assessment

5.1.7.1 Textile Electrode Performance

Textile electrode performance assessment are presented for both textile electrode characterization and EDR signals evaluation. Figure 5.6 shows the experimental data fitting of the Butler–Volmer equation, from which α (transfer coefficient), j_0 (exchange current density), and R_T (charge transfer resistance) are estimated and reported in Table 5.15. In addition, outside the region of validity of the Butler–Volmer equation, a limiting current density J_{SAT} is experimentally detected and resulted to be 0.0103 [A/m^2]. The goodness of fit is about of 0.969, calculated by $Adj(R2)$, which confirmed the good agreement between the theoretical and experimental data. Figures 5.7 and 5.8 report the magnitude and phase of the textile electrode impedance calculated in the frequency bandwidth of the EDR, where the impedance magnitude decreases as frequency increases and phase is pretty linear implying a constant group delay and no distortion introduction. A comparative performance evaluation of EDRs is performed by calculating the Spearman correlation coefficient between signals coming from standard and textile electrodes placed in crossed-finger configuration. More specifically, tonic and phasic components of EDR are compared in addition to the whole signal. The choice of a non-parametric index is justified by non-gaussianity of the data. In Table 5.16, the mean value and the standard deviation of the correlation coefficient are reported.

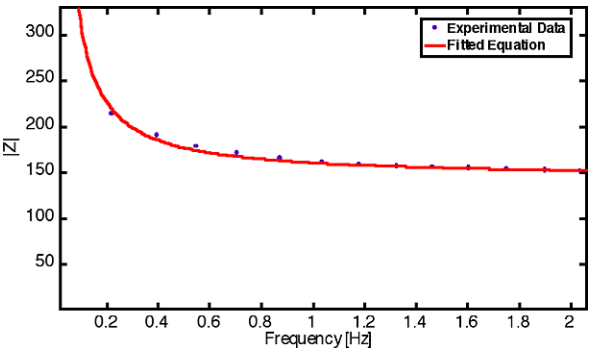

Fig. 5.7 Fit of the magnitude of the textile electrode impedance (from [22])

5.1.7.2 Electrodermal Response-Based Arousal and Valence Recognition

Data were acquired by means of the glove shown in Fig. 3.6 using only the index and middle fingers. As reported in Sect. 5.1.1, experimental results are shown in form of confusion matrix from the QDC classifier when only standard features are used (α) rather than they are used in combination with features extracted from non-linear methods (β). In Table 5.17 classification results of the four classes of different arousal (A1, A2, A3 and A4) and the neutral class (N) are shown on the principal diagonal of the matrix. It is obtained by the cross-validation technique, which is an average of forty confusion matrix calculated on a randomly shuffled dataset. In each element constituting the diagonal, it has been reported mean value and standard deviation of the classification result for that class, respectively. In all other elements the error of classification is reported as well. Each principal component, obtained from applying the PCA algorithm to the feature sets, accounts for a given amount

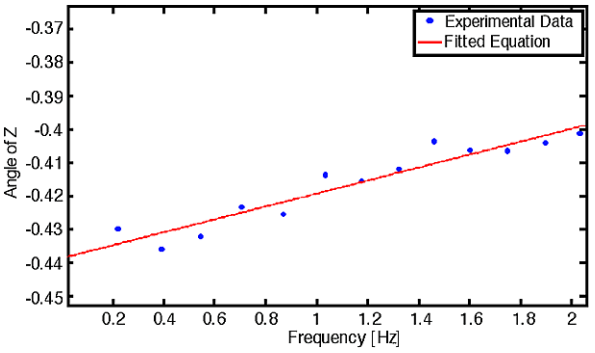

Fig. 5.8 Phase of the textile electrode impedance (from [22])

Table 5.16 Spearman correlation for tonic and phasic skin conductance, and whole EDRs in crossed-finger configuration (from [22])

Spearman coefficient	Tonic	Phasic	Total EDR
ρ	0.9570 ± 0.0241	0.9947 ± 0.0013	0.9604 ± 0.0311

Table 5.17 Confusion matrix of QDC Classifier for Arousal level recognition, α indicates standard feature set with a PCA-reduction to 19 components; β indicates feature set, by nonlinear methods, with a PCA-reduction to 7 components (from [22])

QDC	Dataset	N	A1	A2	A3	A4
N	α	**95.7 ± 3.9**	33.6 ± 18.7	33.6 ± 17.5	23.6 ± 16.2	20.7 ± 16.4
	β	**100 ± 0**	10.0 ± 9.4	3.8 ± 2.1	5.3 ± 3.3	9.2 ± 12.5
A1	α	2.7 ± 3.8	**26.4 ± 22.8**	10.7 ± 13	5.7 ± 8.5	4.2 ± 11.4
	β	0 ± 0	**90.0 ± 9.4**	0 ± 0	0 ± 0	0 ± 0
A2	α	0.9 ± 1.9	27.1 ± 13	**25.7 ± 22**	43.6 ± 26.4	30.7 ± 26.7
	β	0 ± 0	0 ± 0	**96.2 ± 2.1**	0 ± 0	0 ± 0
A3	α	0.3 ± 1.1	3.6 ± 6.3	17.1 ± 15.8	**11.4 ± 9.9**	27.1 ± 18.5
	β	0 ± 0	0 ± 0	0 ± 0	**94.7 ± 3.3**	1.6 ± 4.4
A4	α	0.3 ± 1.1	9.3 ± 16.9	12.8 ± 17.9	15.7 ± 19	**17.1 ± 20.5**
	β	0 ± 0	0 ± 0	0 ± 0	0 ± 0	**89.2 ± 13.8**

of the total variance. The reduction process was stopped when the cumulative variance reached 95%. Therefore the number of principal components is different for standard dataset and the joint dataset (see caption of the table for further details).

5.1.8 Eye Tracking and Pupil Area Variation

In this paragraph, a first study aiming at investigating eye tracking and pupil area variation in response to stimulation using images form IAPS is reported. The association between eye information and emotional image categories was studied by using an innovative head-mounted eye tracking system (HATCAM, see Chap. 3) able to acquire pupil variation together with eye gaze trajectory and time of fixation as well, during exposition of subjects to affective images. The main goal was to identify characteristic features from pupil size variation and eye tracking and by means of classification methods to distinguish the neutral from arousal elicited states. Let $L_{ij}(x, y)$ be the set of eye-gaze points from the frame i of the image j, where x and y are spatial coordinates. The recurrence quantification analysis (RQA) was applied to the set $G_m(x, y)$ defined as:

$$G_m(x, y) = \bigcup_i L_{ij}(x, y) \tag{5.1}$$

A subset of the healthy subjects participating the study described in Chap. 3 is considered. Specifically, ten subjects (nine males and one female) volunteered to participate in the experiment. All subjects do not suffer from evident mental pathologies. Six subjects had dark eyes and 4 had bright eyes. The average age was of 26.8 with a standard deviation of 1.5. The experiment was performed in a room with illumination condition achieved by white neon lighting equally distributed in the room with

Fig. 5.9 Example of the points of gaze detected during a neutral elicitation. Gaze points are marked in *red* (from [58, 59])

Fig. 5.10 Example of the points of gaze detected during a arousal elicitation. Gaze points are marked in *red* (from [58, 59])

a power of 50 lumens. Subjects were asked to sit on a comfortable chair in front of a screen at a fixed distance of 70 cm. The HATCAM system was also equipped with a chin-support in order to avoid unwanted head movements. They were presented with a sequence of images, gathered from the IAPS database, while wearing headsets for acoustical insulation. The slideshow is comprised of 5 sessions of images N, A, N, A, N, where N is a session of 5 neutral images, and A are sets of 5 images having maximum level of arousal and the lowest valence, i.e. high negative affective impact. During the experimental test all the subjects were asked to look at the picture which appeared on the screen for 10 seconds. Each trial lasted about 25 minutes.

Figures 5.9 and 5.10 show the map of points of gaze over two sample images, having neutral and the highest value of arousal, respectively. Gaze points are marked in red. Already at glance, the neutral image (Fig. 5.9) shows a more sparse spatial distribution of the gaze points than the arousal image, in which gaze points are mainly concentrated in confined areas.

By way of illustration, Fig. 5.11 reports an example of neutral image also showing the eye gaze pattern. No negatively valenced images are intentionally reported because of high visual impact. In Fig. 5.12 a 3D representation of the eye gaze points over a neutral image is reported. The z-axis represents how many times each pixel was fixated during the presentation time of ten seconds. On each image, the gaze points are reported. Already at glance, most of neutral images showed a more sparse spatial distribution of the gaze points than the images with arousal, in which gaze points were mainly concentrated into confined areas. A more quantitative anal-

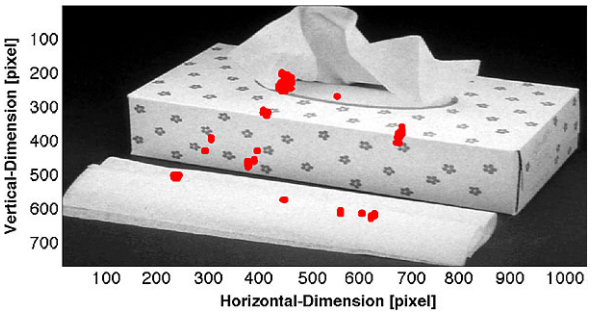

Fig. 5.11 Example of the points of gaze detected during a neutral elicitation. Gaze points are marked up in *red* (from [58, 59])

ysis was done extracting the above described features from the distribution of eye gaze patterns and using them as input of the MLP classifier.

RQA analysis is used to quantify the gaze point distribution for each frame of each image. All the extracted features from RQA and pupil area variation are not normally distributed, as confirmed by the Lilliefors test [330], which returns a p-value ($p < 0.05$) rejecting the null hypothesis of normality. Accordingly, the Kruskal–Wallis test [331] is used, which is a non parametric one-way analysis of variance by ranks for testing equality of population medians. Kruskal–Wallis is performed on ranked data, so the measurement observations are converted to their ranks in the overall data set. This test does assume an identically-shaped and scaled distribution for each group, except for any difference in medians. The null hypothesis is stated as the probability that the samples come from identical populations, regardless their distributions. In place of the mean of distributions, the median is considered as a measure of location [341]. Having only two sets of features, one for arousal and one for neutral, Kruskal–Wallis test returned the probability that the two

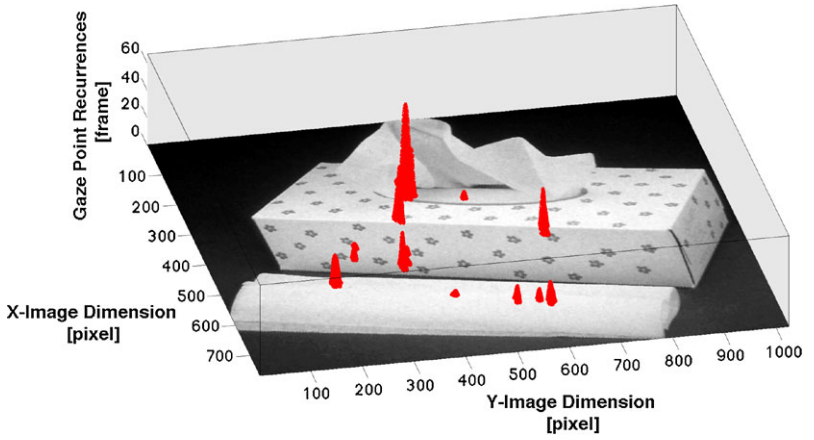

Fig. 5.12 3D representation of the gaze points over the image across the recurrence times each pixel was fixated (from [58, 59])

Table 5.18 Features extracted from RQA using the eye-gaze data (from [58, 59])

Features	Neutral	Arousal
RR*	0.0018 ± 0.0002	0.0019 ± 0.0002
DET**	0.7311 ± 0.0782	0.6373 ± 0.0798
TT**	2.5862 ± 0.9024	2.0345 ± 0.4368
L**	2.9184 ± 0.4564	2.6513 ± 0.3181
ENTR**	1.2592 ± 0.2306	1.0501 ± 0.2041
L^{**}_{max}	5.0000 ± 1.2800	5.0000 ± 1.0583
T^{**}_{max}	1.9600 ± 0.3509	1.5600 ± 0.3501
Pupil	195.39 ± 19.689	197.27 ± 17.106
LGP**	480.0000 ± 208.5236	331.5000 ± 174.1567
MVA**	33.0000 ± 8.8630	27.0000 ± 7.8800

Table 5.19 Confusion matrix of the k-NN classifier using RQA and pupil size features (from [58, 59])

	Neutral	Arousal
Neutral	**90.2273 ± 5.9622**	20.1136 ± 10.8881
Arousal	9.7727 ± 5.9622	**79.8864 ± 10.8881**

Table 5.20 Confusion matrix of MLP classifier by using the whole set of eye-gaze and pupil size features (from [58, 59])

	Neutral	Arousal
Neutral	**93.9394 ± 4.2855**	20.4545 ± 3.2141
Arousal	6.0606 ± 4.2855	**79.5455 ± 3.2141**

samples were not belonging to the same population, in other words, if there was a statistical difference between the two samples.

Median and Median absolute deviation of all RQA features are reported in Table 5.18. Statistical differences between neutral and arousal elicitation were found ($^{*}p < 0.01$ and $^{**}p < 0.001$).

In Table 5.19, the confusion matrix obtained from k-NN classifier after 40 fold-cross-validation steps is shown.

In Table 5.20, the confusion matrix obtained from MLP classifier after twenty fold-cross-validation steps is shown.

5.2 Modeling the Cardio-Respiratory Coupling During Arousing Elicitation

All methodology proposed in this chapter for effective emotion recognition system deals with monovariate and bivariate non-parametric and nonlinear techniques. In fact, given the experimental data, i.e. ANS signals, several transformations were applied in order to obtain a reliable data-driven feature set able to train our automatic

classification algorithm. Based on previous findings [31, 36, 46], a set of equations model of CR coupling during sympathetic elicitation is proposed. This model is a simply adaptation of the theories of weakly coupled oscillators [39–41] with external driving. Accordingly, this model can constitute a general tool to be easily embedded in other model-based emotion recognition systems. In a previous study [46], the HRV nonlinear dynamics through the well-known DLE [282] was studied (see Sect. 5.1.2). It has been found that, starting from positive values kept also during the neutral elicitation sessions, the DLE became negative during the arousal session with statistical significance ($p < 0.05$). Accordingly, it is reasonable hypothesize a relationship between the DLE and the CR synchronization findings, especially from a biophysics point-of-view. In fact, the physiological signals recorded during the presentation of pictures with arousal contents present a clear loss of DLE (with change of the sign) as well as a CR phase synchronization increase [36]. The connection between DLE and synchronization is well-characterized for nonlinear and also chaotic systems [39, 40]. In fact, if two or more nonlinear oscillatory processes (e.g. heart beat and respiratory activity) are weakly coupled, they can become phase synchronized and such a synchronization manifests itself in the Lyapunov spectrum of the system [39]. Such a coupling leads to a decrease of the $n\phi_1 - m\phi_2$ differences. Moreover, considering an external force (i.e. perturbation) applied to the systems, the DLE is expected to be negative, as result of a stable value of the phase with respect to the phase of the external force, in the time domain [40]. The novelty of this model regards only the fact that it is possible to adapt the nonlinear model of weakly coupled oscillators to the CR system relying on previously defined equations [38]. Let us consider the HRV as the representation in the Fourier domain of the RR interval series, i.e., the weighted summation of complex functions having frequencies $f_{RR} = \omega_{RR}/2\pi$. Likewise, let us consider the respiration dynamics in the frequency domain but with only one component, which corresponds to the respiratory frequency $f_{RSP} = \omega_{RSP}/2\pi$. Therefore, the RR and RSP phase dynamics can be written as follows:

$$\dot{\phi_{RR}} = \omega_{RR} + F(RR, t) \tag{5.2}$$

$$\dot{\phi_{RSP}} = \omega_{RSP} + F(RSP, t) \tag{5.3}$$

where $F(RR, t)$ and $F(RSP, t)$ stand for factors depending on the amplitude of RR and RSP, respectively. When the two oscillators become coupled, then it is possible to write:

$$\begin{cases} \dot{\phi_{RR}} = \omega_{RR} + F_{RR}(RR, t) + \varepsilon G(\phi_{RSP}, \phi_{RR}, \psi) \\ \dot{\phi_{RSP}} = \omega_{RSP} + F_{RSP}(RSP, t) + \varepsilon G(\phi_{RR}, \phi_{RSP}, \psi) \end{cases} \tag{5.4}$$

The simplest non-trivial case is given by $G(\phi_{RR}, \phi_{RSP}, \psi) = \sin[(\phi_{RSP} + \phi_{RR}) - \psi] = \sin(\Delta\phi_{CR})$, where $\Omega = d\psi/dt$ represents the dominant oscillation of an external stimulus (i.e. external force, perturbation). Eq. 5.4 becomes:

$$\frac{d\Delta\phi_{CR}}{dt} = \{\omega_{RR} + \omega_{RSP} - \Omega\} + 2\varepsilon \sin(\Delta\phi_{CR}) + \left\{F(RR, t) + F(RSP, t)\right\} \tag{5.5}$$

This equation is similar to the simple Langevin equation describing phase locking of periodic oscillators in the presence of noise [342]. In the presented experimental framework, it is possible to consider a specific $\Omega = \Omega_{GN} = d\psi_{IAPS}/dt$ assuming its amplitude as function of the arousal level and, the frequency of elicitation of the $\dot{\phi}_{RR}$ and $\dot{\phi}_{RSP}$ systems as function of the valence level. It is possible to write the formal solution of this equation assuming the $\{F(RR,t) + F(RSP,t)\}$ to be Gaussian δ-correlated: $\{F(RR,t) + F(RSP,t)\}\{F(RR,t') + F(RSP,t')\} = 2D\delta(t-t')$. Therefore, it could be solved by using the Fokker–Planck equation where the main quantities that would characterize such a synchronization are, precisely, the averaged frequency $\langle \Delta\dot{\phi}_{CR} \rangle$ and the Lyapunov Exponent. Briefly, the Fokker–Planck equation can be written as follows:

$$\frac{\partial W}{\partial \Delta\phi_{CR}} = \frac{\partial}{\partial \Delta\phi_{CR}}\Big[\big(\{\omega_{RR} + \omega_{RSP} - \Omega\} + 2\varepsilon \sin(\Delta\phi_{CR})\big)W\Big] + D\frac{\partial^2 W}{\partial \Delta\phi_{CR}^2} \tag{5.6}$$

Taking the Fourier-representation of the stationary solution:

$$W(\Delta\phi_{CR}) = \sum W_k e^{ik\Delta\phi_{CR}} \tag{5.7}$$

It is possible to write the continuous-fraction representation of the first Fourier mode:

$$W_1 = \frac{(2\pi)^{-1}}{(2i/\varepsilon)(\{\omega_{RR} + \omega_{RSP} - \Omega\} - iD) + \frac{1}{(2i/\varepsilon)(\{\omega_{RR}+\omega_{RSP}-\Omega\}-i2D)+\cdots}} \tag{5.8}$$

Therefore, the CR synchronization is mainly characterized by means of the averaged frequency:

$$\langle \Delta\dot{\phi}_{CR} \rangle = \{\omega_{RR} + \omega_{RSP} - \Omega\} + 2\pi\varepsilon\, \mathrm{Im}(W_1) \tag{5.9}$$

and the Lyapunov Exponent:

$$\left\langle \frac{d \ln \delta\Delta\phi_{CR}}{dt} \right\rangle = -2\pi\varepsilon\, \mathrm{Re}(W_1). \tag{5.10}$$

5.3 Results from the Study on Bipolar Patients

According to the developed mania–depression model (see Sect. 3.2.2), the goal of these studies is to test the ability of the developed methodologies and classifiers in discriminating the mood states of bipolar patients.

5.3.1 Long-Term Analysis

This analysis concerns with a long-term monitoring in a naturalistic environment of three bipolar patients. According to the experimental procedure described in Sect. 3.2.1, three patients enrolled for the preliminary validation phase of the PSYCHE project were included in this study. In detail, patient 1 (hereinafter BP1) is a 38 year-old female, patient 2 (hereinafter BP2) is a 55 year-old male, and patient 3 is a 37 year-old female (hereinafter BP3). Before entering the study, each patient signed an informed consent approved by the ethical committee of the University of Pisa.

The acquired signals are preliminarily processed, i.e. cleaned from the parts of the signals with artifacts, segmented and filtered. Afterwards, the significant features are extracted from each signal, combined in a unique feature space, and then reduced using the PCA method. Finally, the features are classified using various machine learning methods [234]. Several classifiers such as the linear discriminant classifier (LDC), the quadratic discriminant classifier (QDC), a mixture of Gaussian (MOG), the k-nearest neighbor (k-NN), the Kohonen self organizing map (KSOM), the multi-layer perceptron (MLP), and the probabilistic neural network (PNN) were tested. In order to choose the best classification algorithm, a statistical comparison was performed using the analysis of variance (ANOVA) test [303] to test the null hypothesis that no differences exist among all the classification algorithms. Since this study deals with the long-term acquisition of ANS signals, the non-stationary nature of such signals must be considered to perform a proper feature extraction phase. Accordingly, features were extracted within moving time windows of length W of the artifact-free signal. Each acquisition (see Table 5.21) can be seen as a concatenation of equally-long (i.e. W) segments of biosignals. The multidimensional points of the feature space associated to each acquisition have the same class label. General statistics and specific features (hereinafter called *standard features*) as well as features extracted from nonlinear dynamic techniques (e.g. entropy measures, recurrence plot, etc.) were considered. A summary of the selected features extracted from the RR and RSP signals is reported in Table 5.22. These measures were chosen following concepts, guidelines and previous studies reported in the current literature in both the psycho-physiological and bioengineering domains. Specifically, the RR standard features were mainly suggested by the guidelines reported in [24, 98], and the nonlinear measures were profitably used in my previous work [31].

Table 5.21 reports for each patient the initial and final time of each acquisition along with the percentages of the signal cleaned from the movement artifacts. After the MAR step, each signal was visually checked in order to identify physiological (ectopic or arrhythmic beats) or algorithmic artifacts (i.e. errors due to misdetection of the R-peaks). As it can be seen, good percentages of the retained signals were achieved, thus confirming the robustness of the wearable system even during long-term monitoring in a natural environment.

A class label was associated to each point in the feature space, according to the model described in Sect. 3.2.2 and schematically reported in Fig. 3.5. Accordingly, Table 5.23 reports the mood states of the patients during each acquisition.

Table 5.21 Percentage of biosignals retained after the MAR step (from [54])

Subj. ID	Original signal length	Retained signal length	% Retained
BP1-ACQ. 1	15h40m33s	10h20m8s	82.3453
BP1-ACQ. 2	16h30m6s	12h54m30s	70.3354
BP1-ACQ. 3	13h22m52s	11h36m24s	94.7302
BP1-ACQ. 4	15h17m29s	12h40m33s	79.1542
BP2-ACQ. 1	12h15m39s	8h22m16s	68.2755
BP2-ACQ. 2	15h14m3s	11h48m35s	77.5215
BP2-ACQ. 3	11h59m31s	10h5m36s	84.1692
BP2-ACQ. 4	10h16m26s	7h5m2s	68.9507
BP2-ACQ. 5	12h54m12s	10h40m42s	82.7556
BP2-ACQ. 6	16h19m50s	8h56m1s	54.7045
BP3-ACQ. 1	17h36m7s	15h51m40s	90.1105
BP3-ACQ. 2	14h49m5s	11h24m28s	76.9848

The *original signal length* column refers to the amount of data recorded for each acquisition until the wearable system battery ran out. The *retained signal length* column refers to the amount of artifact-free data retained for the post-processing analyses.

The mood states evaluated in this work are the remission-euthymia, (ES), mild depression (MD), severe depression (SD), and mild mixed state (MS). Some descriptive statistics about the most relevant indexes, also used for the classification, are reported in Tables 5.24, 5.25, and 5.26. To average among all the values, the median values over all the acquisitions for each class were considered according to the outcome of the Kolmogorov–Smirnov test for normality ($p < 0.05$, i.e. data are not normally distributed). The values are expressed as median and its respective absolute deviation (i.e. for a feature X, $X = \text{median}(X) \pm \text{MAD}(X)$ where $\text{MAD}(X) = |X - \text{median}(X)|$).

The dimension of this dataset was reduced by applying the PCA algorithm. Since each principal component accounts for a given amount of the total variance, the optimal reduced dimension was selected as the one which gives the cumulative variance equal to 95% at least. It was found that a reduced dimension of 7 components is sufficient to explain such a value of variance. In this study, only an intra-subject classification was performed because of the small number of patients involved as well as the small number of examples for some classes. Moreover, such an approach falls within the area of personalized health care systems, which are preferred in the field of mental disorders.

Confusion matrices from several commonly-used algorithms such as LDC, QDC, MOG, k-NN, KSOM, MLP, and PNN are collected. Taking into account the elements of the main diagonal, i.e. r_{ij} with $i = j$, a statistical analysis was performed for each $i = j = \{1, 2\}$ by means of the ANOVA test.

Concerning BP1 and BP2, the *post-hoc* analysis, using the Bonferroni correction, gave a significative p-value ($p < 0.05$) for both elements r_{11} and r_{22} showing

Table 5.22 Selected features extracted from RR and RSP signals for the long-term bipolar patients study (from [54])

Typology	Biosignal	Feature
Standard measures	RR	μ_{RR}
		σ_{RR}
		RMSSD
		pNN50%
		TINN
		LF
		HF
		LF/HF
	RSP	RSPR
		MFD
		SDFD
		MSD
		SDSD
		MAXRSP
		MINRSP
		DMMRSP
		Skewness
		Kurtosis
		Power in 0–0.1 Hz
		Power in 0.1–0.2 Hz
		Power in 0.2–0.3 Hz
		Power in 0.3–0.4 Hz
High order spectra	RR & RSP	MBI
		VBI
		MMB
		PEB
		NBE
		NBSE
Nonlinear dynamics	RR	DLE
		ApEn
		RecR
		DET
		LAM
		TT
		AV
		ENTR
		L_{max}
		DFA α_1
		DFA α_2

Table 5.23 Clinical labels associated to each bipolar patient during each long-term acquisition (from [54])

ID	ACQ. 1	ACQ. 2	ACQ. 3	ACQ. 4	ACQ. 5	ACQ. 6
BP1	MD	SD	MD	ES		
BP2	MD	MD	MD	MD	MD	ES
BP3	MS	ES				

that the best accuracy was obtained by means of the MLP neural network and, thus, it is the most suitable classifier for the considered application, i.e. mood recognition/discrimination. Regarding the three confusion matrices of BP3, the MLP gave comparable results ($p > 0.05$) in terms of r_{11} values obtained by means of KSOM, and in terms of r_{22} values obtained by means of QDC. Otherwise, significative p-values ($p < 0.05$) were obtained pointing out the MLP better accuracy. Note that the k-NN, LDC, MOG and PNN gave poor results for all of the patients. In fact,

Table 5.24 Selected descriptive statistics of the features from the bipolar patient BP1 (from [54])

BP1 features	MD	SD	ES
μ_{RR}	0.7559 ± 0.0615	0.7507 ± 0.0826	0.8224 ± 0.1267
σ_{RR}	0.0317 ± 0.0172	0.0350 ± 0.0120	0.0685 ± 0.0250
RMSSD	0.0340 ± 0.0168	0.0424 ± 0.0181	0.0446 ± 0.0104
pNN50%	4.8128 ± 3.8649	3.9537 ± 2.4831	20.3980 ± 8.4363
TINN	0.2100 ± 0.1150	0.2825 ± 0.0975	0.3100 ± 0.1000
LF	2.6900 ± 2.2989	2.8248 ± 2.4202	0.0026 ± 0.0021
HF	3.6341 ± 2.9069	4.1721 ± 3.6044	8.4589 ± 3.1042
LF/HF	0.7388 ± 0.3289	0.6517 ± 0.2305	3.0415 ± 2.2429
ApEn	0.8640 ± 0.1186	0.8624 ± 0.1076	0.7077 ± 0.1145
DFA α_1	0.9758 ± 0.1691	0.8489 ± 0.1670	1.3865 ± 0.2047
DFA α_2	0.8288 ± 0.1798	0.6992 ± 0.1522	0.9661 ± 0.1615

Values are expressed as $X = \text{median}(X) \pm \text{MAD}(X)$

Table 5.25 Selected descriptive statistics of the features from the bipolar patient BP2 (from [54])

BP2 features	MD	ES
μ_{RR}	0.7687 ± 0.0661	0.8192 ± 0.0988
σ_{RR}	0.0313 ± 0.0107	0.0319 ± 0.0136
RMSSD	0.0364 ± 0.0150	0.0274 ± 0.0129
pNN50%	3.4424 ± 2.3524	4.3256 ± 3.4817
TINN	0.2575 ± 0.0825	0.1800 ± 0.0650
LF	2.6926 ± 1.7427	4.4200 ± 3.2629
HF	2.4233 ± 2.0904	1.9436 ± 1.6271
LF/HF	1.0468 ± 0.5698	2.9063 ± 1.9288
ApEn	0.7891 ± 0.1226	0.7902 ± 0.1030
DFA α_1	0.9322 ± 0.2053	1.2849 ± 0.2125
DFA α_2	0.8364 ± 0.1575	0.7839 ± 0.1537

Values are expressed as $X = \text{median}(X) \pm \text{MAD}(X)$

at least one of the two elements of the main diagonal of the confusion matrix was $< 67\%$.

The MLP results are shown in Tables 5.27, 5.28, 5.29, 5.30, and 5.31. An MLP was implemented having three layers of neurons. The first layer, the input one, was formed by 7 neurons, one for each of the reduced dimension of the feature space. The third layer, the output one, was formed by 2 neurons, one for each of the considered classes to be recognized. The second layer, the hidden one, was constituted by an empirically estimated number of neurons. Specifically, this number was chosen as the superior limit of the half difference between the number of the input and output neurons, i.e. 5. Insufficient recognition was obtained by considering the 3-class problem (i.e. ES vs MD vs SD) on patient BP1.

Table 5.26 Selected descriptive statistics of the features from the bipolar patient BP3 (from [54])

BP3 features	MS	ES
μ_{RR}	0.9698 ± 0.0244	0.7505 ± 0.0653
σ_{RR}	0.0979 ± 0.0108	0.0218 ± 0.0072
RMSSD	0.0606 ± 0.0062	0.0221 ± 0.0108
pNN50%	33.9872 ± 5.2543	1.0959 ± 1.0959
TINN	0.4375 ± 0.0500	0.1650 ± 0.0850
LF	0.0062 ± 0.0019	13.4740 ± 8.9033
HF	0.0013 ± 0.0006	7.6230 ± 4.9012
LF/HF	5.4873 ± 2.5745	1.7222 ± 0.9657
ApEn	0.6399 ± 0.0517	0.8115 ± 0.0922
DFA α_1	1.5118 ± 0.0914	1.0785 ± 0.2299
DFA α_2	0.9476 ± 0.1344	0.8489 ± 0.1629

Values are expressed as $X = \text{median}(X) \pm \text{MAD}(X)$

5.3.2 *Long-Term Analysis: The Role of History-Dependence*

Although effective in characterizing patients' mood states, the approach proposed in the previous paragraph presents two main limitations: first, the temporal dynamics

Table 5.27 Intra-subject classification on BP3 data (from [54])

Conf. mat. MLP	Class ES	Class MS
Class ES	$\mathbf{97.96 \pm 2.27}$	3.24 ± 3.06
Class MS	2.04 ± 2.27	$\mathbf{96.76 \pm 3.06}$

Class ES: 126 examples. Class MS: 162 examples. Total: 288 examples

Table 5.28 Intra-subject classification on BP2 data (from [54])

Conf. mat. MLP	Class ES	Class MD
Class ES	$\mathbf{68.31 \pm 6.49}$	11.13 ± 3.23
Class MD	31.69 ± 6.49	$\mathbf{88.87 \pm 3.23}$

Class ES: 216 examples. Class MD: 412 examples. Total: 628 examples

Table 5.29 Intra-subject classification on BP1 data (from [54])

Conf. mat. MLP	Class ES	Class MD-SD
Class ES	$\mathbf{74.58 \pm 7.34}$	7.65 ± 2.05
Class MD-SD	25.42 ± 7.34	$\mathbf{92.35 \pm 2.05}$

Class ES: 131 examples. Class MD: 415 examples. Total: 546 examples

Table 5.30 Intra-subject classification on BP1 data (from [54])

Conf. mat. MLP	Class ES	Class MD
Class ES	**79.00 ± 7.12**	12.00 ± 3.82
Class MD	21.00 ± 7.12	**88.00 ± 3.82**

Class ES: 131 examples. Class MD: 283 examples. Total: 414 examples

Table 5.31 Intra-subject classification on BP1 data (from [54])

Conf. mat. MLP	Class ES	Class SD
Class ES	**93.75 ± 3.81**	5.25 ± 3.84
Class SD	6.25 ± 3.81	**94.75 ± 3.84**

Class ES: 131 examples. Class MD: 132 examples. Total: 263 examples

of patient's mood episodes is not taken into account (patients passing from depression to euthymia through mixed-state would be evaluated as patients passing from mixed-state to depression through euthymia); second, patients experiencing more than two mood states were assessed by performing comparative evaluations for each couple of mood states, i.e., 2-class pattern recognition problem.

Here, a novel approach is employed to overcome such limitations. In particular, patients' mood changes are modeled as a discrete-time stochastic process, i.e., the so-called Markov property [306–308]. Each recording is associated to a specific mood state and its evaluation depends also on the previous state.

Once all HRV features are extracted, for each patient, the feature set related to the kth acquisition can be defined as a multidimensional vector $X_{nk}(T_m)$ representing n features evaluated within the time window T_m. In order to consider the process of mood states as Markov chain, i.e., $\Pr\{X_{nk} = x|(X_{n(k-1)} = x_{k-1})\}$, a simple rescaling procedure is applied. Specifically, for each feature vector the matrix $Y_{nk}(T_m) = [X_{nk}(T_m) - \text{median}(X_{n(k-1)})]/\,\text{MAD}(X_{n(k-1)})$ is calculated, where $\text{MAD}(X) = \text{median}(|X - \text{median}(X)|)$.

This model is justified by the hypothesis that the transition from a clinical mood state to another is dependent on the past history of mood fluctuations. The obtained feature set $Y_{nk}(T_m)$ is taken as input of the Leave-One-Out (LOO) procedure [343] applied on a Support Vector Machine (SVM)-based pattern recognition [340]. nu-SVM (nu = 0.5) having a radial basis kernel function with $\gamma = n^{-1}$ was used. A mood label, given by psychological clinical assessment, was associated to each point in the feature space $Y_{nk}(T_m)$. All the classification results were expressed as recognition accuracy in detailed confusion matrices [302].

To test this novel approach, another dataset of bipolar patients is taken into account. Details on the patients' acquisitions as well as mood state information are reported in Table 5.32.

Tables 5.33–5.40 show the recognition accuracy in terms of confusion matrices obtained through the LOO procedure on nu-SVMs. Since no patients have a hy-

Table 5.32 Clinical labels associated to each patient during each acquisition

ID	ACQ. 1	ACQ. 2	ACQ. 3	ACQ. 4	ACQ. 5	ACQ. 6
BP1	MC	MC	MC	ES	ES	
BP2	MC	MS	MC	MC		
BP3	MC	MC	MC	ES	ES	
BP4	DP	DP	DP	DP	DP	ES
BP5	DP	DP	MC	DP	MC	
BP6	MC	MC	MC	ES	ES	
BP7	DP	DP	ES			
BP8	MS	MS	DP	DP	DP	ES

Mood states are associated to Euthymic state (ES), Mania (MC), Mixed-state (MS), and Depression (DP)

Table 5.33 Confusion matrix of SVM classifier for BP1

BP1	Mania	Euthymic
Mania	88.64	11.36
Euthymic	29.20	70.80

Table 5.34 Confusion matrix of SVM classifier for BP3

BP3	Mania	Euthymic
Mania	97.78	2.22
Euthymic	11.11	88.89

Table 5.35 Confusion matrix of SVM classifier for BP2

BP2	Mania	Mixed-State
Mania	86.46	13.54
Mixed-state	3.75	96.25

Table 5.36 Confusion matrix of SVM classifier for BP4

BP4	Depression	Euthymic
Depression	99.68	0.32
Euthymic	8.05	91.95

pomaniac episode we assign only four labels: mania, depression, mixed state and euthymia.

As shown in Table 5.33, the subjective ANS patterns of BP1 and BP3 are well-distinguished reaching more than 88% of accuracy in recognizing the maniac state.

Table 5.37 Confusion matrix of SVM classifier for BP5

BP5	Depression	Mania
Depression	74.87	25.13
Mania	3.77	96.23

Table 5.38 Confusion matrix of SVM classifier for BP6

BP6	Mania	Euthymic
Mania	93.98	6.02
Euthymic	7.49	92.51

Table 5.39 Confusion matrix of SVM classifier for BP7

BP7	Depression	Euthymic
Depression	97.47	2.53
Euthymic	13.33	86.67

Table 5.40 Confusion matrix of SVM classifier for BP8

BP8	Mixed-state	Depression	Euthymia
Mixed-state	78.08	13.70	8.22
Depression	4.51	93.90	1.59
Euthymia	7.53	8.22	84.25

Regarding BP2, more than 86% and 96% of accuracy has been reached in distinguishing mania from mixed-state patterns.

The two mood patterns of BP4 result strongly different obtaining a recognition accuracy as high as 99.68%.

Despite about 25% of the depressive patterns were confused with the maniacal ones, the mania states of BP5 were recognized with more than 96% of accuracy.

Patient BP6 and BP7 showed accuracies greater than 86% in recognizing a severe pathological behavior before reaching the euthymic condition.

Finally, BP8 showed mood swings among three states such as mixed-state, depression, and euthymia, distinguished with satisfactory accuracies (see Table 5.40).

In order to generalize these results we tested the classifier when data were normalized with respect to a casual mood status among the fluctuations or without applying the normalization procedure. The accuracy resulted to be lower than the proposed normalized approach.

5.3.3 *Long-Term Analysis: The Role of Nonlinear Heartbeat Dynamics Through Multiscale Entropy Analysis*

As reported in Chap. 2, many evidences in the literature on nonlinear dynamics of physiological signals show that complexity is a marker of health status of biological systems, and it is modulated by external stimuli, aging and presence of disease. Here, the hypothesis that heartbeat nonlinear dynamics is modulated by different pathological mental states is tested through MultiScale Entropy (MSE) analysis of heart rate variability (HRV) series.

To this aim, a total amount of 16 night recordings, 6 out of which were associated to the label depression, 5 to label hypomania, and 5 to label euthymia were analyzed. All clinical states have been evaluated according DSM-IV-TR criteria [344] and all patients were recruited in the out-patient university clinic of Strasbourg, France. The night-recordings of HRV series were acquired using the comfortable sensing t-shirt with integrated fabric electrodes and sensors developed in the frame of the European project PSYCHE (see Chap. 3).

MSE was calculated on each acquisition of each patient estimating up to the twentieth scale factor. For all scale factors, results are expressed as median and its respective absolute deviation (i.e. for a feature X, $X = \text{median}(X) \pm \text{MAD}(X)$ where $\text{MAD}(X) = \text{median}(|X - \text{median}(X)|)$). The m value is fixed for all cases to the standard value $m = 2$. The objective r_{max} value has been taken as reference for the MSE radius estimation.

Kruskal–Wallis test revealed statistical differences between the groups at all scales. In particular, when scale is equal to 1 and for scale values comprised between 7 and 19, the null hypothesis of having no difference was rejected with $p < 0.01$. At scales 2, 3, 4 and 6 the null hypothesis was rejected with $p < 0.05$, while at the remaining scale 5, the obtained p-value is less than 0.06.

Moreover, the Complexity Index (CI) [211] of each series was evaluated as the area under the curve of the MSE graph. Here, CI is calculated on short time scales, from 1 to 8. Results of the CI index for the three groups (euthymic, depressed, hypomanic) are as follows:

- Euthymic State: 15.18 ± 3.85
- Depressed State: 11.71 ± 1.50
- Hypomanic State: 9.14 ± 1.18

The Kruskal–Wallis test revealed statistical differences between the three mood states on both short ($p < 0.03$) and higher time scales ($p < 0.001$).

Therefore, it has been demonstrated that complexity level can be used as marker of mental states being able to discriminate among depressive, hypomaniac and euthymic states, according to findings from the current literature that the healthier the higher complexity.

Table 5.41 Clinical labels associated to each patient during each acquisition (from [54, 55])

ID	ACQ. 1	ACQ. 2	ACQ. 3	ACQ. 4	ACQ. 5
BP1	Euth				
BP2	Depr				
BP3	Depr	Euth			
BP4	Depr	Depr			
BP5	Depr	Depr	Depr	Depr	Euth

5.3.4 Short-Term Analysis

In this study, the goal was to discriminate depressive from euthymic ANS patterns using the short-term emotional-related elicitation protocol described in Sect. 3.2.1. Five patients were monitored over a period up to 90 days within the European funded project PSYCHE. Details on patient's acquisitions and associated mood states, either euthymia (Euth) or Depression (Depr), are reported in Table 5.41.

5.3.4.1 Cardiovascular Assessment

Using the short-term data, experimental results concerning the discrimination of depressive and euthimic cardiovascular patterns, which were obtained by HRV analyses [57], are reported here.

Accuracies obtained by using the standard analysis were compared with those obtained using the novel point-process nonlinear model proposed in Sect. 4.6.1.

The engagement of the nonlinear terms of the NARI model was further validated by performing a comparative analysis demonstrating how the inclusion of instantaneous HOS features indeed improves the accuracy and reduces the uncertainty (variance) in recognizing ANS depressive patterns. Experimental results are shown in terms of statistical inference and confusion matrices [345].

For each subject, the NARI model was applied to the RR series detected from the recorded ECG. The optimal model order was chosen by means of the Akaike Information Criterion (AIC) [30] applied to the first 5-min RR recordings. The AIC analysis indicated $6 \leq p \leq 8$ and $1 \leq q \leq 2$ as optimal orders. All the KS distances were < 0.05 (range: 0.0345 ± 0.0068). No less than 97% of the autocorrelation points were inside the boundaries.

The linear and nonlinear indices, described in Sect. 4.6.3, were evaluated for all of the patient's acquisition. The instantaneous identification (5 ms resolution) was averaged within a time window of 1 second. Representative tracking results are shown in Figs. 5.13 and 5.14 for BP1 (Euthymic phase) and BP2 (Depressive phase), respectively.

A preliminary statistical analysis was performed in order to evaluate the feature contribution as intra-subject analysis. Statistical inferences were performed to test the null hypothesis of no significative differences occurring among different mood

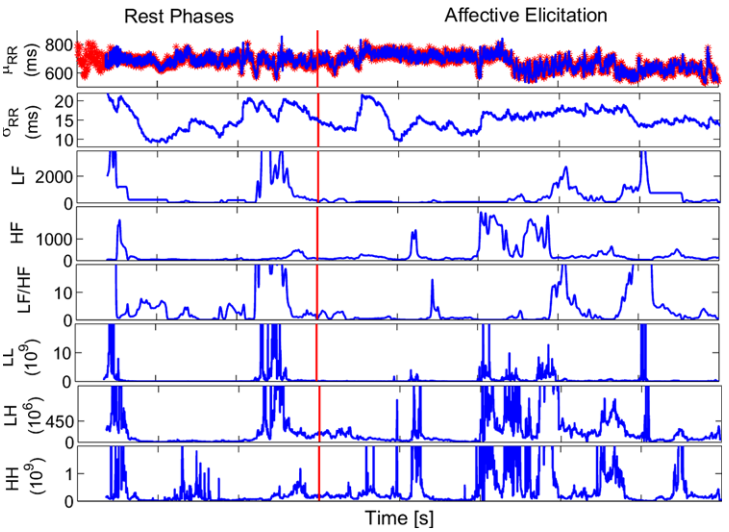

Fig. 5.13 Instantaneous HRV statistics computed from Subject 1 during the euthymic state. The estimated $\mu_{RR}(t, \mathcal{H}_t, \xi(t))$ is superimposed on the recorded RR series. Following below, the instantaneous heartbeat standard deviation, the instantaneous heartbeat spectral Low frequency (LF) and High frequency (HF) powers and their ratio. Finally, *bottom rows* report on the three bispectral statistics

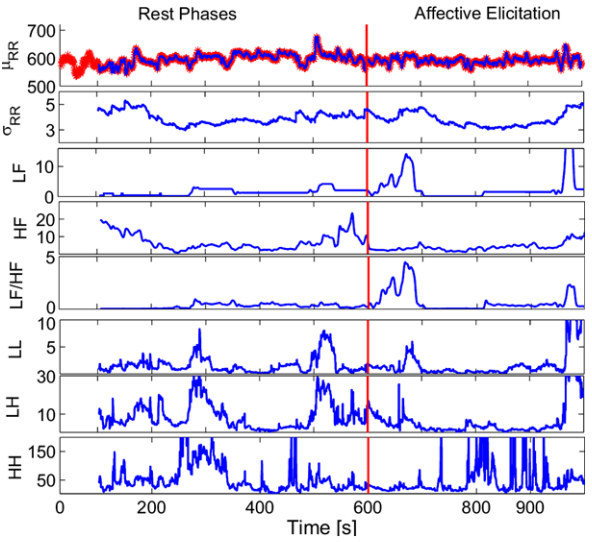

Fig. 5.14 Instantaneous HRV statistics computed from Subject 2 during the depressive state. The estimated $\mu_{RR}(t, \mathcal{H}_t, \xi(t))$ is superimposed on the recorded RR series. Following below, the instantaneous heartbeat standard deviation, the instantaneous heartbeat spectral Low frequency (LF) and High frequency (HF) powers and their ratio. Finally, *bottom rows* report on the three bispectral statistics

states. Such analyses were performed on patients having more than one acquisition, i.e., BP3, BP4, and BP5. First, the whole feature pattern (linear and nonlinear) was treated as multivariate distribution and tested by means of non-parametric multivariate analysis of variance (npMANOVA). Such a test revealed statistical differences

among acquisitions for all the three patients (BP3: $p < 10^{-6}$; BP4: $p < 0.005$; BP5: $p < 10^{-6}$). No significative conclusions can be drawn from this analysis, which is therefore insufficient for an effective discriminative task.

As a consequence, further monovariate statistical analyses were performed to evaluate difference among acquisitions for each of the extracted features. Non-parametric Kruskal–Wallis and Rank-Sum tests were used to investigate the inter-subject variability among the 5 acquisitions of BP5 and the 2 acquisitions of BP3 and BP4, respectively. These results are summarized in Tables 5.42, 5.43, and 5.44. All the features coming from the linear (L) and nonlinear (NL) coefficients were taken into account. Significative p-values in all cases but the LF/HF ratio of BP4 have been obtained. Remarkably, this is the only patient having more than one acquisition having all the same mood label.

Moreover, an inter-subject analysis was performed to reveal the mood pattern, which would be in common among patients. Discrimination of the mood states was performed using the well-known MLP Neural Network [346]. All results are expressed in the form of confusion matrix, after 40-fold cross validation.

The MLP accuracy was compared by creating two feature sets. The first set, α, is composed by $\mu_{RR}(t, \mathcal{H}_t, \xi(t))$, σ_{RR}, and the spectral indices LF, HF, and LF/HF. The second set, β, includes the nonlinear LL, LH, and HH indices which will be joined to the α set for future evaluations.

Looking at the values in Tables 5.42 and 5.43, it is straightforward to notice that the inclusion of BP4 and BP5 strongly increases inter-subject variability.

In order to evaluate the effects of such an uncertainty, reflected on mood state classification, a comparative classification analysis was performed considering either three or five patients within the input feature set.

In all cases, in order to take into account the imbalanced number of available examples per class, two different learning rates were considered in the MLP training phases giving the euthymic examples three times more penalty with respect to the depressive example ones.

MLP results using the NARI model are summarized in Tables 5.45 and 5.46. In particular, Table 5.45 shows the recognition accuracy by considering three patients only, namely BP1, BP2 and BP3. In this case, better results were obtained using the joined dataset $\alpha + \beta$. Such an improvement is consistent with all considered classes (mood states), reaching more than 97% of correct recognition.

Table 5.46 shows the recognition accuracy by considering all five subjects. Using dataset α, correct recognition of the euthymic state is below 75%, whereas using dataset $\alpha + \beta$ accuracy increases up to 99%. To further justify the point-process NARI approach, the linear and nonlinear features of the α and β sets were estimated by more standard AR models (see Sect. 4.3.1.1) and then tested the MLP capability of mood discrimination. The relative confusion matrices are shown in Table 5.47. In this case, neither using the α feature set nor using the joined $\alpha + \beta$ set a sufficient satisfactory recognition was reached.

Table 5.42 Results for the intra-subject Euthymia–Depression Discrimination

BP5	ACQ1 (Depr)	ACQ2 (Depr)	ACQ3 (Depr)	ACQ4 (Depr)	ACQ5 (Euth)	p-val.
μ_{RR} (ms)	708.46 ± 6.47	764.01 ± 11.47	733.67 ± 13.94	660.95 ± 14.45	590.86 ± 6.93	$<10^{-6}$
σ_{RR} (ms)	31.82 ± 7.07	47.13 ± 13.09	84.59 ± 29.12	22.74 ± 5.82	15.28 ± 3.67	$<10^{-6}$
LF (ms^2)	21.56 ± 15.29	40.80 ± 34.84	28.49 ± 27.96	2.38 ± 2.05	1.51 ± 0.89	$<10^{-6}$
HF (ms^2)	12.37 ± 7.88	23.41 ± 12.32	36.28 ± 18.85	6.88 ± 3.11	4.75 ± 2.17	$<10^{-6}$
LF/HF	1.01 ± 0.81	1.60 ± 1.29	0.69 ± 0.65	0.40 ± 0.30	0.41 ± 0.21	$<10^{-6}$
LL (10^6)	10.32 ± 8.94	42.85 ± 36.54	29.73 ± 26.34	2.85 ± 2.05	1.23 ± 0.76	$<10^{-6}$
LH (10^6)	28.20 ± 20.06	61.78 ± 44.17	73.22 ± 50.80	17.87 ± 11.98	5.43 ± 3.46	$<10^{-6}$
HH (10^6)	104.27 ± 68.47	117.11 ± 75.44	140.95 ± 81.53	90.81 ± 54.20	31.89 ± 16.26	$<10^{-6}$

p-values are obtained from the Kruskal–Wallis test

Table 5.43 Results for the intra-subject Euthymia–Depression Discrimination

BP4	Derivation	ACQ1 (Depr)	ACQ2 (Depr)	p-val.
μ_{RR} (ms)	L-NL	734.46 ± 15.94	655.34 ± 5.92	$<10^{-6}$
σ_{RR} (ms)	L-NL	146.39 ± 67.50	39.86 ± 7.62	$<10^{-6}$
LF (ms^2)	L	197.54 ± 186.57	23.90 ± 18.67	$<10^{-6}$
HF (ms^2)	L	53.42 ± 30.45	18.47 ± 9.49	$<10^{-6}$
LF/HF	L	3.16 ± 2.86	1.29 ± 1.16	>0.05
LL (10^6)	NL	65.83 ± 53.67	17.35 ± 11.52	$<10^{-6}$
LH (10^6)	NL	83.46 ± 58.22	75.44 ± 34.19	$<10^{-6}$
HH (10^6)	NL	121.09 ± 64.45	124.64 ± 71.65	$<10^{-6}$

p-values are obtained from the Rank-Sum test

Table 5.44 Results for the intra-subject Euthymia–Depression Discrimination

BP3	Derivation	ACQ1 (Depr)	ACQ2 (Euth)	p-val.
μ_{RR} (ms)	L-NL	632.61 ± 9.44	628.13 ± 18.84	$<10^{-6}$
σ_{RR} (ms)	L-NL	304.79 ± 97.86	237.73 ± 104.25	$<10^{-6}$
LF (ms^2)	L	11.45 ± 10.14	104.77 ± 86.99	$<10^{-6}$
HF (ms^2)	L	42.69 ± 21.98	107.00 ± 53.63	$<10^{-6}$
LF/HF	L	0.27 ± 0.23	0.99 ± 0.75	$<10^{-6}$
LL (10^6)	NL	3.92 ± 2.92	35.54 ± 27.75	$<10^{-6}$
LH (10^6)	NL	12.61 ± 9.88	83.34 ± 48.59	$<10^{-6}$
HH (10^6)	NL	67.53 ± 48.78	136.46 ± 73.80	$<10^{-6}$

p-values are obtained from the Rank-Sum test

Table 5.45 Results for the inter-subject Euthymia–Depression Discrimination in patients BP1, BP2, and BP3

MLP-3 patients	Dataset	Euthymia	Depression
Euthymia	α	93.26 ± 2.98	5.88 ± 1.99
	$\alpha + \beta$	**99.33 ± 0.46**	2.41 ± 0.94
Depression	α	6.74 ± 2.98	94.12 ± 1.99
	$\alpha + \beta$	0.67 ± 0.46	**97.59 ± 0.94**

5.3.4.2 Electrodermal Response Assessment

EDR changes are exploited for assessing the bipolar patient's mood state during the emotional stimulation. Patients are identified with the abbreviations Pz01, Pz02 and Pz03. Pz01 and Pz03 performed the experiment two times, while the patient Pz02 performed the experiment five times. Details on the clinical evaluations of the patients are reported in Table 5.48. The extracted features considered were the mean value, maximum value and Area Under the Curve (AUC) of the driver signals

Table 5.46 Results for the inter-subject Euthymia–Depression Discrimination in all patients

MLP-5 patients	Dataset	Euthymia	Depression
Euthymia	α	74.44 ± 18.21	1.09 ± 1.92
	$\alpha + \beta$	$\mathbf{99.56 \pm 0.39}$	0.01 ± 0.06
Depression	α	25.55 ± 18.21	98.91 ± 1.92
	$\alpha + \beta$	0.44 ± 0.40	$\mathbf{99.98 \pm 0.06}$

Table 5.47 Results for the inter-subject Euthymia–Depression Discrimination using standard techniques in all patients

MLP-5 patients	Dataset	Euthymia	Depression
Euthymia	α	25.00 ± 25.32	15.50 ± 16.00
	$\alpha + \beta$	32.50 ± 31.11	21.50 ± 19.42
Depression	α	75.00 ± 25.32	84.50 ± 16.00
	$\alpha + \beta$	67.50 ± 31.11	78.50 ± 19.42

within a window response of 5 s. AUC is conceived as an optimum indicator of sympathetic activity [247]. An intra-subject statistical inference analysis was performed by means of non parametric tests due to the non-gaussianity of the sample sets. Concerning subjects Pz01 and Pz03, the features of each pair of acquisition were compared by a Rank-Sum test to show whether the data belonged to the same population or not. The Subject Pz02 had more than two available acquisitions. Therefore a multiple comparison analysis applying the Mann–Whitney U-test with a Bonferroni adjustment for every pair of Pz02's acquisitions was carried out. The procedure was repeated for both the tonic and phasic driver features. The classification process was used to perform a recognition of the clinical mood states (i.e. depression state, mixed-state and euthymic state). In order to perform the classification, a k-Nearest Neighbor classifier was used.

The clinical evaluations of the patients under examination are shown in Table 5.49.

The Mann–Whitney test was performed on the features extracted from the phasic driver signal, in order to compare the two acquisitions of both patients Pz01 and Pz03. A p-value less than 10^{-6} showing a strong statistical difference was obtained. A Kruskal–Wallis test was performed on the acquisitions of subject Pz02 showing that the null hypothesis of equal medians among the acquisitions can be

Table 5.48 Clinical evaluations of the patients (from [55])

	Acq.1		Acq.2		Acq.3	
	Mood state	Anxiety	Mood state	Anxiety	Mood state	Anxiety
Pz01	Depressed	High	Euthymic	Low	×	×
Pz02	Mixed-state	High	Mixed-state	Low	Depressed	High
Pz03	Mixed-state	High	Depressed	Low	×	×

Table 5.49 Clinical evaluations of the patients (from [55])

	Acq.4		Acq.5	
	Mood state	Anxiety	Mood state	Anxiety
Pz01	×	×	×	×
Pz02	Depressed	Low	Euthymic	Low
Pz03	×	×	×	×

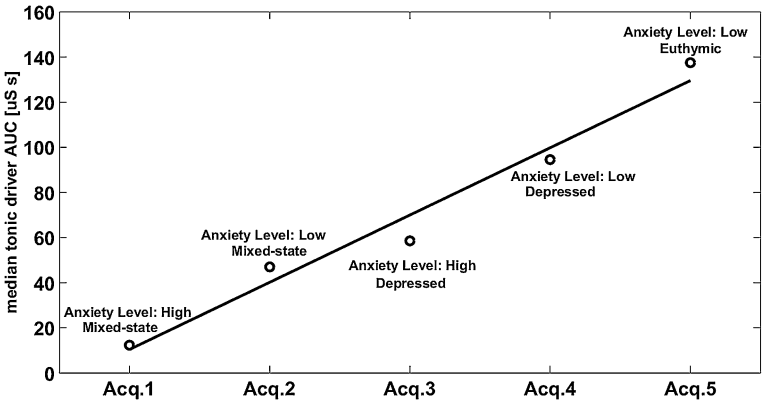

Fig. 5.15 Linear regression of tonic-driver-AUCs of Pz02 (from [55])

rejected with a p-value less than 10^{-6}. A post-hoc test using Bonferroni adjustment was carried out to investigate on all pairwise comparisons. All the pairs resulted statistically different with a p-value less than 10^{-6}. Similar results were achieved analyzing the features extracted from the tonic driver signal of patients Pz01, Pz03. It was obtained, indeed, a strong statistical difference with a p-value less than 10^{-6}. Kruskal–Wallis test on the acquisitions of subject Pz02 showed that at least one acquisition was statistically different from the others, while the post-hoc test with Bonferroni adjustment showed that there were statistically significant differences among all pairs of acquisitions (with a p value less than 10^{-6}) except for the pair Acq.4 vs Acq.5 ($p = 0.108$). Moreover, among the features, AUC of the tonic driver (tonic-driver-AUC) showed an interesting behavior across the different acquisitions on Pz02. Figure 5.15 reports the median tonic-driver-AUC versus the different acquisitions. Already at a glance it is worthwhile noting a linear monotonic trend, which is confirmed by a linear regression analysis which provided a correlation coefficient of 0.9886 and a p-value of 0.0015. An inter-subject analysis was performed grouping those acquisitions with the same clinical label. The features corresponding to the three groups, i.e. *Depressed*, *Mixed-state* and *Euthymic*, were used as dataset for a pattern recognition by means of the k-NN classifier. More in detail, k-NN classifier was used as supervised machine learning to solve the two class problem for the recognition of Euthymic vs Depressed (see Table 5.50), Euthymic vs Mixed-

Table 5.50 Confusion matrix of Depression state vs Euthymic state (from [55])

	Euthymic	Depressed
Euthymic	**90.50 ± 1.89**	11.69 ± 1.54
Depressed	9.50 ± 1.89	**88.31 ± 1.54**

Table 5.51 Confusion matrix of k-NN classifier for Mixed-state vs Euthymic state (from [55])

	Euthymic	Mixed-state
Euthymic	**76.22 ± 3.11**	18.73 ± 3.24
Mixed-state	23.78 ± 3.11	**81.27 ± 3.24**

Table 5.52 Confusion matrix of k-NN classifier for Mixed-state vs Depressed state (from [55])

	Depressed	Mixed-state
Depressed	**82.08 ± 2.82**	16.91 ± 2.37
Mixed-state	17.92 ± 2.82	**83.09 ± 2.37**

state (see Table 5.51) as well as Depressed vs Mixed-state (see Table 5.52), it is worthwhile noting that all classifications are greater than 76%.

Part IV
Conclusions and Future Works

In this final part, conclusions and future directions of research are drawn in agreement with the experimental evidences found out from the studies on healthy subjects and bipolar patients.

Chapter 6
Conclusions and Discussion on Mood and Emotional-State Recognition Using the Autonomic Nervous System Dynamics

This book demonstrated how electrophysiological signals related to the autonomic nervous system (ANS) dynamics can be source of reliable and effective markers for mood and emotional state recognition.

It has been pointed out that the methodological approach for signal processing and status classification is a crucial step to obtain significative performances. In all of the presented studies, standard signal processing techniques as well as nonlinear measures have been taken into account. According to the significant complex behavior with strong nonlinear and nonstationary dynamic properties of ANS signals, such nonlinear measures have been proven as important quantifiers of cardiovascular control dynamics with prognostic value in both population of healthy subjects and patients. Therefore, these measures should be always taken into account in ANS modeling and analysis [137].

Accordingly,

it is reasonable to represent the cardiovascular system as a nonlinear dynamical system and study it by means of "perturbation" analysis.

It means that the analysis will take into account observations during initial stable conditions (i.e. during rest) and after fast perturbations (i.e., the emotional elicitation). As a matter of fact, high accuracies can be achieved only retaining information on the nonlinear dynamics of such physiological systems. The use of nonlinear system-derived approaches was very important for an effective emotion recognition, in both arousal and valence recognition.

Healthy subjects as well as patients with mood disorders were considered in order to drawn these considerations.

G. Valenza, E.P. Scilingo, *Autonomic Nervous System Dynamics for Mood and Emotional-State Recognition*, Series in BioEngineering,
DOI 10.1007/978-3-319-02639-8_6, © Springer International Publishing Switzerland 2014

Studies on Healthy Subjects Thirty-five healthy subjects were presented with sets of elicitation images gathered from the IAPS database according to a specific protocol (see Chap. 3). Such affective stimuli were characterized by the Circumplex Model of Affects (CMA) [89], in which the affective states are conceptualized by the terms of valence and arousal. Valence represents the extent to which an emotion is perceived as being pleasant or unpleasant. Arousal indicates the intensity of the emotion.

First, the possibility of recognizing the elicited five levels of arousal (including one neutral level) and five levels of valence (including one neutral level as well) by using ANS signals such as HRV, RSP, and EDR has been shown. The results demonstrated that the classification through standard features was acceptable only for the neutral class, while all arousal and valence classes were misclassified. These results highlight that standard feature sets were insufficient to discriminate close levels of arousal or valence. On the contrary, when features extracted from nonlinear dynamic methods were considered, the classification process was able to recognize each level of arousal and valence as well as the neutral class. Accordingly, good classification results are only supported by nonlinear derived features, providing an important contribution to the state of the art, where usually affective state recognition is performed with much less granularity. Results are very satisfactory, although in order to have more statistical significance the number of subjects should be increased. This problem is partially overtaken doing a cross validation in the classification process, i.e. randomizing the subjects for training and test sets. It makes the classification independent from the sequence of the subjects involved. In addition the 40 steps of cross validation make the distributions of the results Gaussian, and explainable with only two parameters (mean and variance) as reported in all the tables. When the classifier is applied to features extracted from nonlinear dynamic methods, results are much higher than those standards. In addition, full successful recognition (100%) was obtained on the Neutral and Arousal1 for arousal level recognition and on the Valence3 for valence level recognition. A possible explanation of these results could be found in the intrinsic nonlinear behavior of the physiological responses, although the issue is inevitably open. The literature reports many attempts to find out correspondences between nonlinear dynamic systems and physiological responses, but often they are only mathematical tricks far from a clear physiological interpretation [32, 347]. These findings only demonstrated the importance of nonlinear temporal patterns for emotion recognition [348, 349], but without claiming any specific theory. Moreover, they are consistent with Scherer's theory, which argues that synchronization of periodic systems is fundamental to emotion, [350].

Aiming at deeply investigating the ANS nonlinear dynamics, techniques derived from nonlinear system identification and chaos theory were applied to identify patterns and mechanisms that are not detectable with traditional statistics based on linear models. It is already documented in the literature that HRV exhibits chaotic behavior dynamics in rest conditions. It has been pointed out how ApEn decreases when switching from neutral to arousal sessions, and DLE is positive for all the neutral sessions and negative during arousal sessions. A statistical analysis has been performed in order to study the statistical significance of the changes in ApEn and

DLE across all sessions and within similar sessions. Moreover, the percentage of subjects exhibiting a more complex behavior in the HRV is significantly higher during all the neutral sessions. Statistical results showed that all the samples of the neutral sessions, as well as of the arousal sessions, can be considered originating from the same distribution, but all neutral sessions considered as a whole and the arousal sessions considered as a whole differ significantly. These results deserve to be discussed. First of all, several physiological adaptation phenomena are involved during the affective elicitation, so the system could react in a similar way during the switching between a neutral and an elicitation with low arousal or high arousal. It has been previously demonstrated how it is necessary to consider the HRV along with both the respiration activity and the electrodermal response in order to well characterize different (and similar) affective elicitation (see [31]). Concerning the SDNN, no statistical difference ($p > 0.05$) was found, meaning that ApEn findings depend only on the change in the complexity behavior and not on the SDNN value used for the calculation of the ApEn itself.

These encouraging results led to extend the study of nonlinear dynamics also for the CR systems interactions. In fact, nowadays, it is well accepted that the cardiovascular system and its relationship with respiration is truly a complex system. Accordingly, a methodology able to characterize the nonlinear interaction of the cardiovascular and the respiratory system in a multivariate manner, even for noisy and non-stationary data, was chosen. Specifically, since two or more weakly coupled nonlinear oscillatory processes can become phase locked, the cardio-respiratory synchronization was studied in the mentioned protocol involving healthy subjects during an affective emotional visual elicitation protocol. CR synchronization was quantified by using the concept of phase synchronization of chaotic oscillators, i.e. the CRS. This technique allowed estimating the synchronization ratio $m : n$ as the presence of n heartbeats in each m respiratory cycle. A clearly reduced synchronization was observed during the presentation of neutral images and an increased synchronization during the presentation of images with significant arousal contents, although no significant statistical differences could be gleaned from among different arousal levels. The result remained stable and congruent throughout all subjects and was not affected by gender. This new result can truly improve the knowledge of the physiology behind affective elicitation and emotional processing. In fact, changes in synchronization activity seem to agree with other kinds of stimulation [43, 145, 351, 352]. The effectiveness of the presented visual stimuli was ensured by the statistically significant changes in the sympatho-vagal balance (i.e. LF/HF ratio). More specifically, the coherent changes of this value with the affective stimuli suggest that the findings on the synchronization are reasonably related to the affective experimental setup excluding habituation phenomenons. For the sake of completeness, standard morphological features were also calculated from HRV such as MeanRR, SDRR, RMSSD, pNN50. No statistical differences were found across the sessions. Similar patterns in cardiovascular findings among different emotional elicitation are not new in the current literature (e.g. see [353]). Consistently with some prior investigations, in fact, the similarity in cardiovascular responses may reflect a generalized emotional response to the affective stimuli. From a physiological point

of view, the outcome of this work could be related to the literature which reports on the mechanisms of short-term cardio-respiratory coupling [34, 354–356]. It is thought to be due to the following mechanisms: reflection of respiratory blood pressure waves via baroreceptor feedback loop in the heart rate [34], respiratory phase-dependent modulation of baroreflex information processing, and central coupling between respiratory neurons on the one hand, and sympathetic and/or parasympathetic neurons on the other hand. Mainly, these mechanisms refer to the Respiratory Sinus Arrhythmia (RSA) [34]. Moreover, it was found that the activity and rhythm of certain sympathetic efferents are closely related to the cardiovascular–respiratory rhythm [33]. Accordingly, an increase of synchronization during arousal elicitation with respect to the neutral elicitation, in which sympathetic activity should be dominant (see the LF/HF ratio results in Table 5.9) was found. From an engineering point of view, cardio-respiratory synchronization could be profitably used as an important multivariate marker to be included in a feature set for discriminating between neutral and arousal elicitation in the field of affective computing. In fact, it has been demonstrated that a combination of features coming from multiple physiological signals increases performance of emotion recognition systems [92, 180, 259, 349]. Moreover, considering the nonlinear behavior and interaction of the physiological system truly improves the accuracy of such systems [31, 357]. It is worthwhile noting that the results of this work are in agreement with the current literature supporting the hypothesis that temporal patterns are important for emotion recognition [349]. In principle, it is possible to apply such an approach to any stimulus acting to the CR systems that produces a sympathetic activation (a statistically significant sympathetic activation was found during the arousal sessions by evaluating changes in the sympatho-vagal balance, i.e., LF/HF ratio, of the HRV [36]).

Moreover, based on the experimental evidences on DLE and CRS, a theoretical nonlinear model on cardiopulmonary oscillators has been reported. It relies on the previously defined theory of weakly coupled oscillators [39–41] driven by external force. It has been hypothesized that the external force is given to the CR systems through the ANS activity modulation on the sympathetic and parasympathetic nerves. Although chaotic behavior cannot be demonstrated in such a bio-system because of the strong physiological noise, the theory reported here aims at giving an useful tool for the assessment of the CR phase synchronization and the DLE changes in HRV. These experimental findings and theorization are in agreement with the *chaos–destroying* synchronization, i.e., when a periodic external force acts on a chaotic system destroys chaos and a periodic regime appears [358]. In the case of an irregular forcing, the driven system follows the behavior of the force [359], which has been experimentally demonstrated by the evaluation of the ANS response as a whole system [31]. In such a case, in fact, the CR system seems to react to the visual elicitation by producing ANS linear and nonlinear markers able to follow the stimulus changes.

In order to improve the accuracy of the previously developed emotion recognition system, bivariate measures related to the CR phase synchronization, were combined to the monovariate measures (feature set α). The obtained feature space dimension was reduced using the PCA method and a QDC algorithm performed the

pattern recognition phase. Also in this case, results are very satisfactory. Despite the reference set α, the proposed feature set β gave a recognition accuracy grater than 90% for all classes in both arousal and valence discrimination. Moreover, the performed cross validation process, i.e. randomizing the subjects for training and test set, ensured that the classification was independent from the specific subjects involved. Although the proposed methodology definitely goes beyond the state-of-the-art, less performances in identifying one arousal class, i.e., the $A1$, and two valence class, i.e., $V1$ and $V3$ were reported. From the literature, it is possible to consider the CMA plane as an orthonormal space in which each point is a combination of arousal and valence values. Hence, these classification findings allowed the finely identification of 25 regions. Although this is a great achievement, it is noteworthy mentioning that they may not represent 25 different emotional states.

Considering the healthy subject assessment during the presentation of a single image, a novel methodology (the point-process NARI model) able to assess in an instantaneous, personalized, and automatic fashion whether the subject is experiencing a positive or a negative emotion was presented. Remarkably, the NARI model was validated with an experimental ECG dataset with healthy subjects undergoing a tilt-table procedure [47]. Results demonstrate that the NARI algorithm confirms the characterization of the tilt effect on standard and instantaneous indices of the sympatho-vagal balance, while simultaneously tracking significant changes in the inherent nonlinearity of heartbeat dynamics with tilt. Moreover, the NARI model was applied on the recognition of two levels, i.e. low-medium and medium-high, of arousal and valence in order to performed for a comprehensive characterization of the emotional status. As mentioned above, such assessments were performed considering only the cardiovascular dynamics through the RR interval series on short-time emotional stimuli (each image was kept for < 10 seconds). To achieve such a result, an ad-hoc mathematical framework based on point-process theory has been defined. The point-process framework is able to parametrize the heartbeat dynamics in continuous time without using any interpolation methods. Therefore, instantaneous measures of HR and HRV [30, 212] for robust short-time emotion recognition are made possible by the definition of a physiologically-plausible IG probability. An innovative aspect of the methodological approach is also the use of the derivative RR series [309, 313] to fit the model. This choice allowed us to remarkably improve the tracking of the affective-related non-stationary heartbeat dynamics. The novel fully autoregressive structure of our model accounts for the pioneering short-time affective characterization having knowledge related to both linear and nonlinear heartbeat dynamics. In fact, the quadratic autoregressive nonlinearity associated to the most likely heartbeat accounts for the input–output HOS such as the instantaneous bispectrum and trispectum. Unlike other paradigms developed in the literature for estimating human emotional states [7], this approach is purely parametric and the analytically-derived indices can be evaluated in a dynamic and instantaneous fashion. As currently used standard signal processing methods would be unable to give reliable and effective results because of resolution or estimation problems, the methodology proposed here represents a pioneering approach in the current literature and can open new avenues in the field of affective computing. Although the

recognition accuracy proposed in this work relates to only two levels of arousal, valence and self-reported emotion, oversimplifying the complete characterization of the affective state of a subject, the emotional assessment in short-time events using cardiovascular information only is a very challenging task never solved before. Using only heartbeat dynamics, the two basic levels of both arousal and valence were effectively distinguished, thus allowing for the assessment of four basic emotions. An important advantage is that the proposed framework is fully personalized, i.e. it does not require data from a representative population of subjects. From a physiological perspective, the inherent nonlinearties of the cardiovascular systems (e.g. the nonlinear neural signaling on the sinoatrial node [29]) have been also confirmed by our experimental results. According to the nonlinearity tests [337], in fact, 27 out of the 30 RR series resulted to be the outputs of a nonlinear system. Of note, the results from goodness-of-fit tests were all positive, demonstrating that the proposed NARI model always performs a good prediction of the nonlinear heartbeat dynamics. In agreement with previous results [31], here instantaneous nonlinear features have been introduced and improved the accuracy in the majority of the population (> 15 subjects). In addition, these experimental results support previous studies where instantaneous HRV indices extracted by means of a point process model provided a set of dynamic signatures able to characterize the dynamic range of cardiovascular responses under different physiological conditions [30]. Therefore, the novel instantaneous nonlinear features could provide better assessment and improved reliability during such physiological responses.

In this book, novel wearable systems able to perform ANS monitoring in a naturalistic environment have been also presented. The possibility of using a fabric glove including textile electrodes to acquire EDR has been investigated. Firstly, textile electrodes have been electrically characterized, then they are used to acquire EDR in a dedicated affective computing experiment similar to the one mentioned above characterizing the elicited levels of arousal and valence. More specifically, a set of features was extracted from the EDR and used as input to a classifier to recognize five arousal classes. Electrode characterization has been performed calculating the voltage-current characteristics as well as the electric impedance of the textile electrode and finding that the electric behavior is comparable with standard electrodes. In addition, an acquisition protocol was designed and realized, where signals from textile and standard electrodes are simultaneously acquired, in order to verify if textile electrodes were suitable for EDR acquisition. The results have been very satisfactory and showed that textile electrodes can be used likewise standard electrodes without loss of information. Nevertheless, further work has to be done in order to carefully address the issue of contact quality and contact area stability of textile electrodes as well as experimentally verify that finger movement does not strongly affect the signal quality. Indeed, a sensing glove allows us to investigate emotion fluctuations during naturalistic elicitation. Next works will aim at evaluating the movement artifact effect on the quality of the EDR acquired during dynamic tasks. Moreover, eye tracking and pupil size variation has been investigated in response to emotional elicitation induced by IAPS images. In particular, the goal was to identify a set of features from pupil size variation and eye tracking in order to

distinguish between neutral to arousal states. An innovative wearable and wireless head-mounted eye tracking system (HATCAM) was used to acquire pupil variation together with eye-gaze trajectory as well as time of fixation. In addition, a novel methodology was adopted to characterize differences between neutral and arousal elicitation, in eye-gaze acquisitions, by means of features extracted from RQA. This choice is motivated by the analogy between the bi-dimensional image containing eye-gaze points and the matrix commonly used for Recurrence Plot [276]. Both, indeed, are matrixes of zero and ones. In addition to the features from RQA, the elliptic area of pupil and the fixation time were also included in the feature space for arousal and neutral classification. Pattern recognition was performed by means of k-Nearest Neighbor (k-NN) classifier. After the k-NN training process, the performance of the classification task was evaluated by using the confusion matrix. It was randomized for 40-fold cross-validation steps to avoid bias. Results are reported in Table 5.20. As it can be seen results are very satisfactory. The percentage of successful recognition is about 90% for neutral images and about 80% for images at high arousal. It means that eye gaze, both in terms of pupil tracking and size, can be a viable means to discriminate different affective states.

Since the extracted eye information is regulated by the autonomic nervous system, the results of this experiment suggest that the autonomic nervous system responds differently to emotionally arousing than to emotionally neutral stimuli. These results are in line with the previous results [31], that showed changes in the autonomic activity in terms of skin conductance responses, respiration and heart rate variability behavior, during exposition to IAPS images with different arousal content. Even though our results showed a significative information from eye gaze pattern, however, they did not show significant pupil size differences among IAPS stimulation. In the literature there are discordant works about the pupil size variation upon affective stimuli. In the study of [125] it is reported that pupil size may not be sensitive enough to discriminate emotional responses, while [126] and [123] showed experimental evidence about this affective-dependence variation. In my study, pupil size does not seem to have a relevant role, but it could also be explained in terms of low resolution of the camera used in the HATCAM system, which did not detect the fine pupil responses, or of a possible failure in providing right controlled stimuli, considering also that there are several factors affecting the variation of pupil size. [128] listed several different sources of pupil size variation, including, for example, the light reflex, different stimulus parameters (e.g. visual and chemical), and information-processing load. However, besides the role of pupil size, our results are very satisfactory and very promising for the use of eye information pattern in the context of pervasive monitoring. This would extend the perceptually intelligent abilities of an engine to perceive and analyze human behavior. In human behavior positive emotions have been argued to increase creativity, to help in creating richer associations for memorized material, and to realize more efficient decision-making machines [360, 361]. In addition, by using suitable emotion-related cues, it could be also possible to modulate the user emotional reactions that could be used also as possible therapy in mental disease management.

Studies on Bipolar Patients Concerning the studies on bipolar patients, an effective mood recognition system based on a pervasive, long-term and short-term monitoring of ANS-related physiological signals in bipolar patients has been presented. This approach was supported by several studies that have shown how mood disorders are correlated with several dysfunctions of the ANS, both in the sympathetic and parasympathetic systems [203–205].

For this reason, a comfortable, textile-based sensorized t-shirt was used to perform the acquisition of the RR as well as the RSP. Alongside the acquisition, a personalized classification system together with the related signal processing chain was implemented in order to robustly estimate the mood state of the patient. The above concepts are those behind the PSYCHE project.

As for the healthy subjects studies, both generic (i.e. statistics and nonlinear) and specific features were extracted from the pre-processed signals and then a label describing the mood state was associated to each point of the feature set, corresponding to a specific region of a bidimensional space in which mania and depression have been sampled and combined to characterize the bipolar disorder. It is worthwhile noting that no effective mood recognition system using long-term monitoring of ANS signals of bipolar patients based on an ad-hoc mood model has ever been proposed in the current scientific literature.

Experimental results have been performed following three bipolar patients from the first hospitalization to the end of the therapy, i.e. euthymia condition. For each patient, the study included up to a maximum of 6 evaluations over a 90 day-period. Each acquisition was obtained during long-term monitoring with up-to 16 hours of data. A classification accuracy of up to 95% for the intra-subject problem was achieved.

The very high accuracy for intra-subject classification has two direct relapses from a clinical and research point of view. From the clinical point of view, it documents the reliability of the PSYCHE platform for the monitoring of the mood status at the level of the single subject. For the first time a system that accurately detects the mood state in bipolar patients was presented. After an adequate training (performed for instance during hospitalization in a ward or even in a day-hospital facility) the system could be used at home by the patient as a feasible monitor of the clinical conditions and could provide the patient himself and clinicians helpful clues, e.g. for a potential relapse, remission and, in general, mood change. Form a research point of view it is also worth noting that this result suggests that a discrete combination of psychophysiological features can be a specific marker of the mood status in bipolar disorders.

As a preliminary evaluation, it is necessary to mention some limitations in this study. In fact, the whole PSYCHE system relies on the patient mood label given by the physician during the training phase. Therefore, an error in such an evaluation could be crucial for the further assessment biasing the decision support. In addition, more data coming from a statistical representative and homogeneous population of a bipolar patient is needed for the validation of the system in terms of generalization, robustness and reliability.

As mentioned in the method section, another possible limitation of the study is the fact that it relies on an ad-hoc mood model without a clinical validation. The

model is a summarized pattern sets of mood states relying on clinical observations. It resulted to be an effective and viable means to fulfill the PSYCHE project mission, which is to predict and classify the clinical status. A more detailed and validated model will be defined when a higher number of participants will be available for the analysis. However, it is worthwhile underlining that diagnosis in psychiatry still suffers, in general, from a lack of validity, i.e. clinical diagnoses are not supported by the evidence of neurobiological changes. Therefore, a validated model for clinical assessment is quite far from being achieved. However, it is interesting to note that it was possible to distinguish the non-pathological clinical status (remission-euthymia, i.e., class ES) from the pathological ones (mild depression, i.e., class MD; severe depression, i.e., class SD; mild mixed state, i.e., class MS;) in all of the bipolar patients considered.

Moreover, the classification accuracy is greater in distinguishing euthymia from severe clinical states (severe depression and mixed state) (Tables 5.27 and 5.31) than euthymia from the milder ones (mild depression) (Tables 5.28 and 5.30). It is possible to hypothesize that the differences in accuracy mirror the distances in clinical status and in its psychophysiological correlates. Such results were presented and evaluated by means of confusion matrices. This choice was motivated by the effectiveness and conciseness of their values allowing for the straightforward calculation of widely used statistical measures such as the sensitivity, specificity, ROC curves, area under the curve etc. Nevertheless, results only emphasize the whole cardio-respiratory pattern of the different mood states instead of identifying the actual biomarkers. Indeed, this investigation will be performed in the next developments of this work. These satisfactory results are very promising in the frame of the PSYCHE project. In addition, the methodology proposed here can be easily applied to data coming from other systems collecting cardio-respiratory signs (e.g. standard Holter with respiratory belt). Moreover, other previously proposed platforms for data collection and health assessment, e.g. [362–364], can be adapted after the integration of the proposed biosignal processing chain.

Another personalized approach which identifies mood states as intra-subject analysis taking into account the temporal dynamics of the illness has also been presented. This approach has been suggested also by clinical observations: is widely accepted that clinical status is different in different moment of the course of bipolar illness. For instance one can diagnose a depressive episode in a patient that just enter in the episode and in the one who is going to remit the very day after. Although for the rigid diagnostic criteria the two episodes are equal, from a clinical point of view it is very different. Following this logic here we demonstrate on a psychophisological base this clinical descriptive evidence.

Finally, a multiscale entropy (MSE) analysis has been presented. The complexity of the heartbeat dynamics in bipolar patients through MSE analysis of HRV series. The choice of such a specific analysis is justified by the fact that MSE has been proven a powerful tool in translational psychiatry discerning patients with major depressive syndrome from healthy subjects [211], in spite of a high inter-subject variability. In particular, significant lower complexity has been found in the depressive patients with respect to the healthy subjects. Accordingly, the experimental

hypothesis was to extend the discerning capability of MSE analysis by studying multiple pathological mental states associated to mood states. Using the objective MSE estimation, an interesting complexity modulation coherent with both the current literature and different mood states was found. In particular, higher complexity at all scales is associated to the euthymic state, whereas the depressive and hypomanic states show decreased complexity values ($p < 0.01$).

Studies on Bipolar Patients: Short-Term Studies Concerning the investigation on the bipolar patients short-term protocol, a novel experimental/methodological approach has been proposed for the assessment of instantaneous ANS patterns of depression in bipolar patients. The novel point-process NARI approach allows the mathematical representation of the cardiovascular system as a nonlinear dynamical system characterized by means of a perturbation analysis, i.e., analysis before and after short-time emotional elicitation.

Five patients, experiencing depressive and euthymic episodes, were enrolled to participate in a dedicated affective elicitation protocol. A comfortable, textile-based sensorized t-shirt (namely the PSYCHE platform) was used to perform noninvasive recordings of physiological variables, and a novel point-process NARI model was implemented and applied to the RR series derived from the ECG in order to produce novel instantaneous features. In particular, standard features in both the time (i.e. $\mu_{RR}(t, \mathcal{H}_t, \xi(t))$ and σ_{RR}), and the frequency domain (i.e. LF, HF, and LF/HF) along with higher order nonlinear features, i.e. LL, LH, and HH, were extracted from the processed RR series. The NARI model was used to characterize the mean of an IG distribution representing the inter-beat probability function. Such approach allows for the instantaneous estimation of all HRV measures without any interpolation method [30]. The method is also personalized, fully parametric, and able to improve nonstationary identification [309]. All the mentioned features coming from the NARI representation of the heartbeat dynamics were investigated by using a statistical inference and a pattern recognition methods in intra- and inter-subject analyses, respectively. Multivariate statistical analysis by using an npMANOVA approach revealed significant within-subject differences among different mood states, whereas monovariate analyses pointed-out that only the LF/HF is statistically similar between two depressive phases. Pattern recognition algorithms (MLP) were then applied to the estimated features to classify the mood state of the patients (i.e. "euthymia" or "depression"), and two feature sets were compared. The first set, α, was comprised of only the standard feature set, whereas the nonlinear indices were added to the second set, β.

A comparative classification analysis was performed in order to evaluate the effects on the inter-subject variability. Considering the three patients with fewer acquisitions, i.e., BP1, BP2 and BP3, we demonstrated that both datasets α and $\alpha + \beta$ gave satisfactory results reaching more than 93% of correct recognition per class, although the $\alpha + \beta$ showed highest accuracy (see Table 5.45). On the other hand, considering all five subjects, a classification accuracy of up to about 74% for the α set, and up to about 99% for the $\alpha + \beta$ set was achieved for the euthymic class (see Table 5.46). Therefore, it is clear that the high inter-subject variability strongly

affects the information given by the linear contribution (dataset α) of the model whereas it does not affect the nonlinear one (dataset $\alpha + \beta$). Moreover, the discrimination accuracy obtained with traditional signal processing techniques was not sufficient for a reliable assessment.

Given their preliminary nature, these results are very promising. A common pattern of instantaneous heartbeat features was found despite the inter-subject variability. Our results also show that the inclusion of nonlinear indices gives improved results and smaller variance with respect to the classification performed by using only the standard features. The final result (99.56% accuracy) went beyond expectations, also considering that the few misclassified samples can be easily interpreted as either algorithmic/mathematical artifacts or physiological outliers, i.e. events not related to mood markers for whatever reason.

The presented point-process nonlinear analysis represents a pioneering study in the field of mood assessment in bipolar patients. In our approach, the acquisition paradigm (including high and low arousing IAPS and TAT) was considered as a whole, without subdividing the protocol in separate epochs. More than a limitation, the overall results give additional strength to this approach. Indeed it is not a matter of specific emotional response but more in general the reactivity of the ANS to be affected in bipolar disorders. The fact that it was possible to detect changes in ANS during the protocol as compared to a relaxed baseline is enough to say that ANS reactions are studied despite subjective measurements of emotional arousal or valence related to the used cues.

EDR was analyzed in three bipolar patients recruited in the frame of the European project PSYCHE. For each patient, mood state fluctuated at least once along with a change in the anxiety level. Two patients were monitored with two acquisitions and one subject with five acquisitions.

A deconvolution analysis was applied to the EDR signal. Several features were extracted in order to quantify the phasic and tonic electrodermal activity. The preliminary results showed a statistically significant difference for all the acquisitions from the same subject, which is consistent with the corresponding clinical diagnosis. More specifically, for the subjects Pz01 and Pz03 that had only two acquisitions, in two different mood states, statistical test showed that both mood states were effectively recognized as statistically different. Instead referring to the subject PZ02, who underwent five acquisitions, each state was recognized as statistically different according to the different mood states and anxiety levels.

Only between Acq.4 and Acq.5 of subject Pz02 the Mann–Whitney test showed a p-value greater than 0.05 for the features extracted from the tonic driver component. Acq.4 and Acq.5 had two different clinical labels but the same level of anxiety, but they resulted to be equivalent from a statistical point of view. This may result from the very short time-window occurring between the two acquisitions (six days only) or by the same anxiety level. Much work has to be done in order to gain a closer understanding on this aspect.

Moreover, subject Pz02 showed a monotonic trend of tonic-driver-AUC which is the component that is not related to the stimulus. In particular, the transition from the mixed-state with a high level of anxiety (2) to the euthymic state with a low level

of anxiety (1) showed a linear trend modeled through a linear regression with a high correlation coefficient. Even in this case, this behavior, although very interesting, deserves to be investigated more in depth. Nevertheless, in the other subjects (who had only two acquisitions available, i.e. a number insufficient for a linear regression model) tonic electrodermal activity showed an increase in the presence of a mood change from a depressed state to an euthymic state and from a mixed-state to a depressed state, combined with a lower level of anxiety.

An inter-subject analysis was performed attempting to classify the acquisitions accompanied by the label *euthymic*, *depressed* and *mixed-state* by means of a pairwise comparison between the three class. All the three possible comparisons showed a high discrimination percentage ($> 76\%$). The preliminary results support the hypothesis of a relationship between mood state, anxiety level and electrodermal activity. Although preliminary these results are very satisfactory and encouraging.

Chapter 7
Book Summary and Perspectives for Future Research

In this chapter, the scientific contributions of this book are summarized as follows:

- An experimental procedure for a standardized emotional elicitation has been reported. Data from thirty-five healthy subjects presented with sets of elicitation images gathered from the IAPS database have been acquired. The affective stimuli were characterized by the Circumplex Model of Affects in which the affective states are conceptualized by the terms of valence and arousal.
- The effectiveness of the presented visual stimuli was ensured by the statistically significant changes in the sympatho-vagal balance (i.e. LF/HF ratio).
- The elicited five levels of arousal (including one neutral level) and five levels of valence (including one neutral level as well) have been effectively recognized only by using standard features together with nonlinear features extracted from ANS signals such as HRV, RSP, and EDR.
- The ANS nonlinear dynamics has been deeply investigated through ApEn and DLE analyses of HRV. ApEn decreases when switching from neutral to arousal sessions, and DLE is positive for all the neutral sessions and negative during arousal sessions.
- The nonlinear interaction of the cardiovascular and the respiratory system was quantified by using the concept of phase synchronization of chaotic oscillators, i.e. the CRS. A clearly reduced synchronization during the presentation of neutral images and an increased synchronization during the presentation of images with significant arousal contents were observed. No significant statistical differences could be gleaned from among different arousal levels.
- Based on the experimental evidences on DLE and CRS, a theoretical nonlinear model on cardiopulmonary oscillators has been developed. It relies on the previously defined theory of weakly coupled oscillators driven by external force.
- In order to improve the accuracy of the previously developed emotion recognition system, bivariate measures related to the CR phase synchronization were combined to the monovariate measures. Despite the reference set of monovariate features, the newly proposed feature set gave a recognition accuracy grater than 90% for all classes in both arousal and valence discrimination.

G. Valenza, E.P. Scilingo, *Autonomic Nervous System Dynamics for Mood and Emotional-State Recognition*, Series in BioEngineering,
DOI 10.1007/978-3-319-02639-8_7, © Springer International Publishing Switzerland 2014

- A novel methodology, i.e. the point-process NARI model, able to assess in an instantaneous, personalized, and automatic fashion whether the subject is experiencing a positive or a negative emotion have been developed.
- Such a nonlinear point-process model was validated with an experimental ECG dataset with healthy subjects undergoing a tilt-table procedure. Results demonstrated that the NARI algorithm confirms the characterization of the tilt effect on standard and instantaneous indices of the sympatho-vagal balance, while simultaneously tracking significant changes in the inherent nonlinearity of heartbeat dynamics with tilt.
- The novel fully autoregressive structure of the NARI model accounts for the pioneering short-time affective characterization having knowledge related to both linear and nonlinear heartbeat dynamics. In fact, the quadratic autoregressive nonlinearity associated to the most likely heartbeat accounts for the input-output HOS such as the instantaneous bispectrum and trispectum.
- According to the nonlinearity tests, 27 out of the 30 RR series resulted to be the outputs of a nonlinear system. Of note, the results from goodness-of-fit tests were all positive, demonstrating that the proposed NARI model always performs a good prediction of the nonlinear heartbeat dynamics.
- Concerning the instantaneous emotional pattern recognition, a two-class problem (Low–Medium (L–M) vs Medium–High (M–H) levels) was considered for the arousal, valence and self-reported emotion. The novel point-process NARI model was applied to extract linear and nonlinear features.
- The recognition accuracy of the short-term positive-negative emotions is improved with the use of the nonlinear measures in 14 cases, with $> 60\%$ of successfully recognized samples for all of the subjects and a maximum of 84%.
- The recognition accuracy of the short-term arousal classification is improved with the use of the nonlinear measures in 19 cases, with $> 66\%$ of successfully recognized samples for all of the subjects and a maximum of 98%.
- The recognition accuracy of the short-term valence classification is improved with the use of the nonlinear measures in 19 cases, with $> 60\%$ of successfully recognized samples for all of the subjects and a maximum of 92%.
- Novel wearable systems able to perform ANS monitoring in a naturalistic environment have been developed. Specifically, a fabric glove including textile electrodes to acquire EDR and a wireless head-mounted eye tracking system (HATCAM) have been described.
- A novel personalized monitoring systems for care in mental health has been presented as the core platform of a research carried outing the frame of the European funded project FP7-ICT-247777 PSYCHE.
- Textile electrodes characterization has been performed calculating the voltage-current characteristics as well as the electric impedance of the textile electrode and finding that the electric behavior is comparable with standard electrodes.
- EDR signals from textile and standard electrodes were simultaneously acquired, in order to verify if textile electrodes were suitable for EDR acquisition. The results have been very satisfactory and showed that textile electrodes can be used likewise standard electrodes without loss of information.

- A novel methodology has been proposed to characterize differences between neutral and arousal elicitation, in eye-gaze acquisitions, by means of features extracted from RQA along with the elliptic area of pupil and the fixation time. The percentage of successful recognition is about 90% for neutral images and about 80% for images at high arousal. It means that eye gaze, both in terms of pupil tracking and size, can be a viable means to discriminate different affective states.
- An effective mood recognition system based on a pervasive, long-term and short-term monitoring of ANS-related signals in bipolar patients has been presented. For this reason, a comfortable, textile-based sensorized t-shirt was used to perform the acquisition of the RR as well as the RSP. Alongside the acquisition, a personalized classification system together with the related signal processing chain was implemented in order to robustly estimate the mood state of the patient. The above concepts are those behind the PSYCHE project.
- Generic (i.e. statistics and nonlinear) and specific features were extracted from the pre-processed signals and then a label describing the mood state was associated to each point of the feature set, corresponding to a specific region of a bidimensional space in which mania and depression have been sampled and combined to characterize the bipolar disorder.
- A classification accuracy of up to 95% for the intra-subject problem was achieved following three bipolar patients from the first hospitalization to the end of the therapy, i.e. euthymia condition. Each acquisition was obtained during long-term monitoring with up-to 16 hours of data.
- A novel history-dependent approach based on HRV long-term analysis allowed improved results in terms of recognition accuracies on all the considered mood states.
- The study of heartbeat nonlinear dynamics through MSE analysis of long-term HRV series allowed the inter-subject discrimination of three mental states associated to the bipolar disorder. It is possible to raise the hypothesis of using features from HRV complexity analysis as effective biomarker for mental disorders.
- For the first time, a system that accurately detects the mood state in bipolar patients was presented. The classification accuracy was greater in distinguishing euthymia from severe clinical states (severe depression and mixed state) than euthymia from the milder ones (mild depression).
- Concerning the investigation on the bipolar patients short-term protocol, a novel experimental/methodological approach for the assessment of instantaneous ANS patterns of depression in bipolar patients has been proposed.
- The novel point-process NARI model was implemented and applied to the RR series derived from the bipolar patients' ECG in order to produce novel instantaneous features as standard features in both the time (i.e. $\mu_{RR}(t, \mathcal{H}_t, \xi(t))$ and σ_{RR}), and the frequency domain (i.e. LF, HF, and LF/HF) along with higher order nonlinear features, i.e. LL, LH, and HH.
- A classification accuracy of up to about 74% was obtained using the standard feature set, and up to about 99% using the standard and nonlinear feature set in distinguishing euthymia from other depressive state.

- The high patients' inter-subject variability strongly affects the information given by the linear contribution of the cardiovascular dynamics whereas it does not affect the nonlinear one.
- Patients' EDR was also analyzed in three bipolar patients performing the short-term protocol. The mood state fluctuated at least once along with a change in the anxiety level.
- By applying the deconvolution analysis to the EDR signal and extracting several features, a statistically significant difference for all the acquisitions from the same subject has been observed.
- A specific bipolar patient showed a monotonic trend of tonic-driver-AUC which is the component that is not related to the stimulus. In particular, the transition from the mixed-state with a high level of anxiety (2) to the euthymic state with a low level of anxiety (1) showed a linear trend modeled through a linear regression with a high correlation coefficient.
- An inter-subject analysis was performed attempting to classify the acquisitions accompanied by the label *euthymic*, *depressed* and *mixed-state* by means of a pairwise comparison between the three class. All the three possible comparisons showed a high discrimination percentage ($> 76\%$). The preliminary results support the hypothesis of a relationship between mood state, anxiety level and electrodermal activity.

Some future research directions exploiting the outcomes of the works reported in this book are listed below.

- Study the ANS cross-recurrence by means of a cross Recurrence Plots analysis, especially performed between EDR and HRV.
- Investigate the implementation of the standard and nonlinear algorithms in portable devices such as microcontroller, ARM, DSP, FPGA, etc.
- Apply other nonlinear quantifiers to the ANS signals in order to better characterize the emotional elicitation.
- Improve the point-process NARI model performances using the Laguerre expansion of the kernels.
- Include on further multivariate estimates within the NARI model, since the proposed point-process framework allows the inclusion of physiological covariates such as respiration or blood pressure measures [365].
- Extract novel instantaneous indices from the multivariate point-process model such as features from the dynamic cross-spectrum, cross-bispectrum, respiratory sinus arrhythmia, and baroreflex sensitivity in order to better characterize and understand the human emotional states in short-time events.
- Apply all the developed algorithms to a wide range of experimental protocols in order to validate such tools for underlying patho-physiology evaluation, as well as explore new applications on emotion recognition that consider a wider spectrum of emotional states.
- Exploit eye gaze together with peripheral physiological signals in healthy subjects and in the field of mental care.
- Define novel features for eye-gaze and pupil size variation information.

- Increase the number of bipolar patients enrolled and create a database containing a wide set of acquisitions on which an effective data mining machine could effectively run. The statistical significance will also result improved.
- Explore additional aspects of the linear and nonlinear identification as related to depression/bipolar states.
- Evaluate which part of the proposed short-term protocol is more informative for mood recognition in bipolar disorders.
- Explore more carefully the physiological meaning of the dynamic autonomic signatures both in the context of the underlying mood state, and as a result of the different stimuli administered within the dedicated protocol.
- Investigate if these specific features can be used as a preclinical marker, meaning that they start to change even before the subject mood changes. In this case, it would be possible to use the PSYCHE platform to have an early, pre-symptomatic diagnosis of mood episodes.
- Extend the proposed approaches within the PSYCHE project, including several other available variables (e.g. voice, activity index, sleep pattern alteration, electrodermal response, biochemical markers).

References

1. R. Zajonc, On the primacy of affect. Am. Psychol. **39**(2), 117–123 (1984)
2. C. Darwin, P. Ekman, P. Prodger, *The Expression of the Emotions in Man and Animals* (Oxford University Press, Oxford, 2002)
3. J. Gross, R. Muñoz, Emotion regulation and mental health. Clinical Psychology: Science and Practice **2**(2), 151–164 (1995)
4. R. Lazarus, J. Averill, Emotion and cognition: with special reference to anxiety, in *Anxiety: Current Trends in Theory and Research*, vol. 2 (1972), pp. 242–284
5. A. Damasio, *Descartes' Error: Emotion, Reason, and the Human Brain* (Quill, New York, 2000)
6. D. Sauter, F. Eisner, P. Ekman, S. Scott, Cross-cultural recognition of basic emotions through nonverbal emotional vocalizations. Proc. Natl. Acad. Sci. USA **107**(6), 2408–2412 (2010)
7. R. Calvo, S. D'Mello, Affect detection: an interdisciplinary review of models, methods, and their applications. IEEE Trans. Affect. Comput. **1**(1), 18–37 (2010)
8. S. Ramakrishnan, Recognition of emotion from speech: a review, in *Speech Enhancement, Modeling and Recognition Algorithms and Applications* (2012), p. 121
9. Y. Tang, Y. Ma, Y. Fan, H. Feng, J. Wang, S. Feng, Q. Lu, B. Hu, Y. Lin, J. Li et al., Central and autonomic nervous system interaction is altered by short-term meditation. Proc. Natl. Acad. Sci. USA **106**(22), 8865–8870 (2009)
10. P. Petrantonakis, L. Hadjileontiadis, Emotion recognition from EEG using higher order crossings. IEEE Trans. Inf. Technol. Biomed. **14**(2), 186–197 (2010)
11. K. Ko, H. Yang, K. Sim, Emotion recognition using EEG signals with relative power values and Bayesian network. Int. J. Control. Autom. Syst. **7**(5), 865–870 (2009)
12. Y. Lin, C. Wang, T. Jung, T. Wu, S. Jeng, J. Duann, J. Chen, EEG-based emotion recognition in music listening. IEEE Trans. Biomed. Eng. **57**(7), 1798–1806 (2010)
13. P. Petrantonakis, L. Hadjileontiadis, A novel emotion elicitation index using frontal brain asymmetry for enhanced EEG-based emotion recognition. IEEE Trans. Inf. Technol. Biomed. **15**(5), 737–746 (2011)
14. K. Park, H. Choi, K. Lee, J. Lee, K. An, E. Kim, Emotion recognition based on the asymmetric left and right activation. Internat. J. Med. Med. Sci. **3**(6), 201–209 (2011)
15. S. Hsieh, M. Hornberger, O. Piguet, J. Hodges, Brain correlates of musical and facial emotion recognition: evidence from the dementias. Neuropsychologia **50**(8), 1814–1822 (2012)
16. E. Ruiz-Padial, J. Vila, J. Thayer, The effect of conscious and non-conscious presentation of biologically relevant emotion pictures on emotion modulated startle and phasic heart rate. Int. J. Psychophysiol. **79**(3), 341–346 (2011)
17. M. Tamietto, L. Castelli, S. Vighetti, P. Perozzo, G. Geminiani, L. Weiskrantz, B. De Gelder, Unseen facial and bodily expressions trigger fast emotional reactions. Proc. Natl. Acad. Sci. USA **106**(42), 17661–17666 (2009)

DOI 10.1007/978-3-319-02639-8, © Springer International Publishing Switzerland 2014

18. A. Heller, T. Johnstone, A. Shackman, S. Light, M. Peterson, G. Kolden, N. Kalin, R. Davidson, Reduced capacity to sustain positive emotion in major depression reflects diminished maintenance of fronto-striatal brain activation. Proc. Natl. Acad. Sci. USA **106**(52), 22445–22450 (2009)
19. G. Valenza, M. Carboncini, A. Virgillito, I. Creatini, L. Bonfiglio, B. Rossi, A. Lanatà, E. Scilingo, EEG complexity drug-induced changes in disorders of consciousness: a preliminary report, in *Engineering in Medicine and Biology Society, EMBC, 2011 Annual International Conference of the IEEE* (IEEE Press, New York, 2011), pp. 3724–3727
20. A. Greco, M.C. Carboncini, A. Virgillito, A. Lanatà, G. Valenza, E.P. Scilingo, Quantitative EEG analysis in minimally conscious state patients during postural changes. Paper presented at the Proceeding of the IEEE Engineering in Medicine and Biology International Conference, 2013
21. E. Scilingo, A. Gemignani, R. Paradiso, N. Taccini, B. Ghelarducci, D. De Rossi, Performance evaluation of sensing fabrics for monitoring physiological and biomechanical variables. IEEE Trans. Inf. Technol. Biomed. **9**(3), 345–352 (2005)
22. A. Lanatà, G. Valenza, E. Scilingo, A novel EDA glove based on textile-integrated electrodes for affective computing. Med. Biol. Eng. Comput. **50**, 1163–1172 (2012)
23. G. Valenza, A. Lanatà, E. Scilingo, D. De Rossi, Towards a smart glove: arousal recognition based on textile electrodermal response, in *Engineering in Medicine and Biology Society (EMBC), 2010 Annual International Conference of the IEEE* (IEEE Press, New York, 2010), pp. 3598–3601
24. A. Camm, M. Malik, J. Bigger, G. Breithardt, S. Cerutti, R. Cohen, P. Coumel, E. Fallen, H. Kennedy, R. Kleiger et al., Heart rate variability: standards of measurement, physiological interpretation, and clinical use. Circulation **93**(5), 1043–1065 (1996)
25. U. Rajendra Acharya, K. Paul Joseph, N. Kannathal, C. Lim, J. Suri, Heart rate variability: a review. Med. Biol. Eng. Comput. **44**(12), 1031–1051 (2006)
26. G. Valenza, A. Lanatà, M. Ferro, E.P. Scilingo, Real-time discrimination of multiple cardiac arrhythmias for wearable systems based on neural networks. Paper presented at the Computer in Cardiology, 2008
27. A. Armato, E. Nardini, A. Lanatà, G. Valenza, C. Mancuso, E.P. Scilingo, D. De Rossi, An FPGA based arrhythmia recognition system for possible wearable applications. Paper presented at the 9th International Conference on Intelligent System Design and Application, 30 Nov–2 Dec 2009, Pisa, Italy
28. A. Lanatà, G. Valenza, E.P. Scilingo, The contribution of the phase spectrum in automatic multiple cardiac arrhythmias recognition in wearable systems. Paper presented at the 2010 3rd International Symposium on Applied Sciences in Biomedical and Communication Technologies, ISABEL 2010
29. K. Sunagawa, T. Kawada, T. Nakahara, Dynamic nonlinear vago-sympathetic interaction in regulating heart rate. Heart and Vessels **13**(4), 157–174 (1998)
30. R. Barbieri, E. Matten, A. Alabi, E. Brown, A point-process model of human heartbeat intervals: new definitions of heart rate and heart rate variability. Am. J. Physiol., Heart Circ. Physiol. **288**(1), H424 (2005)
31. G. Valenza, A. Lanatà, E. Scilingo, The role of nonlinear dynamics in affective valence and arousal recognition. IEEE Trans. Affect. Comput. **3**(2), 237–249 (2012)
32. V. Marmarelis, *Nonlinear Dynamic Modeling of Physiological Systems* (Wiley, New York, 2004)
33. H. Koepchen, D. Klussendorf, D. Sommer, Neurophysiological background of central neural cardiovascular–respiratory coordination: basic remarks and experimental approach. J. Auton. Nerv. Syst. **3**(2–4), 335–368 (1981)
34. C. Davies, J. Neilson, Sinus arrhythmia in man at rest. J. Appl. Physiol. **22**(5), 947 (1967)
35. G. Parati, M. Rienzo, G. Mancia, Dynamic modulation of baroreflex sensitivity in health and disease. Ann. N.Y. Acad. Sci. **940**(1), 469–487 (2001)
36. G. Valenza, A. Lanatà, E. Scilingo, Oscillations of heart rate and respiration synchronize during affective visual stimulation. IEEE Trans. Inf. Technol. Biomed. **16**(4), 683–690 (2012)

37. M. Rosenblum, J. Kurths, A. Pikovsky, C. Schafer, P. Tass, H. Abel, Synchronization in noisy systems and cardiorespiratory interaction. IEEE Eng. Med. Biol. Mag. **17**(6), 46–53 (1998)
38. G. Valenza, A. Lanatá, E.P. Scilingo, Improving emotion recognition systems by embedding cardiorespiratory coupling. Physiol. Meas. **34**(4), 449 (2013)
39. M. Rosenblum, A. Pikovsky, J. Kurths, Phase synchronization of chaotic oscillators. Phys. Rev. Lett. **76**(11), 1804–1807 (1996)
40. A. Pikovsky, M. Rosenblum, G. Osipov, J. Kurths, Phase synchronization of chaotic oscillators by external driving. Physica D **104**(3–4), 219–238 (1997)
41. A. Pikovsky, M. Rosenblum, J. Kurths, *Synchronization: A Universal Concept in Nonlinear Sciences*, vol. 12 (Cambridge University Press, Cambridge, 2003)
42. A. Stefanovska, H. Haken, P. McClintock, M. Hožič, F. Bajrović, S. Ribarič, Reversible transitions between synchronization states of the cardiorespiratory system. Phys. Rev. Lett. **85**(22), 4831–4834 (2000)
43. R. Bartsch, J. Kantelhardt, T. Penzel, S. Havlin, Experimental evidence for phase synchronization transitions in the human cardiorespiratory system. Phys. Rev. Lett. **98**(5), 54102 (2007)
44. D. Kenwright, A. Bahraminasab, A. Stefanovska, P. McClintock, The effect of low-frequency oscillations on cardio-respiratory synchronization. Eur. Phys. J., B Cond. Matter Phys. **65**(3), 425–433 (2008)
45. Y. Shiogai, A. Stefanovska, P. McClintock, Nonlinear dynamics of cardiovascular ageing. Phys. Rep. **488**(2), 51–110 (2010)
46. G. Valenza, P. Allegrini, A. Lanatà, E. Scilingo, Dominant Lyapunov exponent and approximate entropy in heart rate variability during emotional visual elicitation. Front. Neuroeng. **5** (2012). doi:10.3389/fneng.2012.00003
47. G. Valenza, L. Citi, E. Scilingo, R. Barbieri, Instantaneous bispectral characterization of the autonomic nervous system through a point-process nonlinear model, in *World Congress on Medical Physics and Biomedical Engineering*, Beijing, China, May 26–31, 2012 (Springer, Berlin, 2013), pp. 530–533
48. G. Valenza, L. Citi, E. Scilingo, R. Barbieri, Using Laguerre expansion within point-process models of heartbeat dynamics: a comparative study, in *Engineering in Medicine and Biology Society (EMBC), 2012 Annual International Conference of the IEEE* (IEEE Press, New York, 2012), pp. 29–32
49. L. Citi, G. Valenza, R. Barbieri, Instantaneous estimation of high-order nonlinear heartbeat dynamics by Lyapunov exponents, in *Engineering in Medicine and Biology Society (EMBC), 2012 Annual International Conference of the IEEE* (IEEE Press, New York, 2012), pp. 13–16
50. G. Valenza, L. Citi, E. Scilingo, R. Barbieri, Point-process nonlinear models with Laguerre and Volterra expansions: instantaneous assessment of heartbeat dynamics. IEEE Trans. Signal Process. **61**(11), 2914–2926 (2013)
51. L. Citi, G. Valenza, P.L. Purdon, E.N. Brown, R. Barbieri, Monitoring heartbeat nonlinear dynamics during general anesthesia by using the instantaneous dominant Lyapunov exponent. Paper presented at the Proceeding of the International IEEE Engineering in Medicine and Biology Conference, San Diego (CA), USA, 2012
52. G. Valenza, L. Citi, R. Barbieri, Instantaneous nonlinear assessment of complex cardiovascular dynamics by Laguerre–Volterra point process models. Paper presented at the Proceeding of the IEEE Engineering in Medicine and Biology International Conference, 2013
53. R. Barbieri, L. Citi, G. Valenza, M. Guerrisi, S. Orsolini, C. Tessa, S. Diciotti, N. Toschi, Increased instability of heartbeat dynamics in Parkinson's disease. Paper presented at the Computers in Cardiology, Zaragoza (Spain) 2013
54. G. Valenza, C. Gentili, A. Lanatà, E. Scilingo, Mood recognition in bipolar patients through the psyche platform: preliminary evaluations and perspectives. Artif. Intell. Med. **57**(1), 49–58 (2013)
55. A. Greco, A. Lanatà, G. Valenza, G. Rota, N. Vanello, E. Scilingo, On the deconvolution analysis of electrodermal activity in bipolar patients, in *Engineering in Medicine and Biology*

Society (EMBC), 2012 Annual International Conference of the IEEE (IEEE Press, New York, 2012), pp. 6691–6694
56. N. Vanello, A. Guidi, C. Gentili, S. Werner, G. Bertschy, G. Valenza, A. Lanatà, E. Scilingo, Speech analysis for mood state characterization in bipolar patients, in *Engineering in Medicine and Biology Society (EMBC), 2012 Annual International Conference of the IEEE* (IEEE Press, New York, 2012), pp. 2104–2107
57. G. Valenza, L. Citi, C. Gentili, A. Lanatà, M. Mauri, E. Scilingo, R. Barbieri, A point-process nonlinear model approach for autonomic assessment of depressive states in bipolar patients. Paper presented at the Proceeding of the 7^{th} International Workshop on Biosignal Interpretation, Como, Italy, 2012
58. A. Lanatà, G. Valenza, E. Scilingo, Eye gaze patterns in emotional pictures. J. Ambient Intell. Humaniz. Comput. 1–11 (2012). doi:10.1007/s12652-012-0147-6
59. A. Lanatà, A. Armato, G. Valenza, E. Scilingo, Eye tracking and pupil size variation as response to affective stimuli: a preliminary study, in *Pervasive Computing Technologies for Healthcare (PervasiveHealth), 2011 5th International Conference on* (IEEE Press, New York, 2011), pp. 78–84
60. A. Lanatà, G. Valenza, E. Scilingo, Electrodermal responses through textile electrodes. Cloth. & Textiles Res. J. **14**(4), 81–88 (2010)
61. J. Russell, J.M. Carroll, On the bipolarity of positive and negative affect. Psychol. Bull. **125**(1), 3–30 (1999)
62. D. Watson, D. Wiese, J. Vaidya, A. Tellegen, The two general activation systems of affect: structural findings, evolutionary considerations, and psychobiological evidence. J. Pers. Soc. Psychol. **76**(5), 820–838 (1999)
63. D. Watson, L. Clark, On traits and temperament: general and specific factors of emotional experience and their relation to the five-factor model. J. Pers. **60**(2), 441–476 (1992)
64. C. Darwin, *The Expression of the Emotions in Man and Animals* (Oxford University Press, New York, 1872), with an introduction, afterword, and commentaries by Paul Ekman
65. P. Ekman, 1. Universal facial expressions of emotion, in *Culture and Personality: Contemporary Readings* (1974), pp. 8–15
66. P. Ekman, Basic emotions, in *Handbook of Cognition and Emotion* (1999), pp. 45–60
67. S. Tompkins, *Affect Imagery Consciousness: Volume I: The Positive Affects* (Springer, Berlin, 1962)
68. C. Izard, *The Face of Emotion*, vol. 23 (Appleton-Century-Crofts, New York, 1971)
69. R. Plutchik, Emotions: a general psychoevolutionary theory, in *Approaches to Emotion* (1984), pp. 197–219
70. P. Ekman, Cross-cultural studies of facial expression, in *Darwin and Facial Expression: A Century of Research in Review* (1973), pp. 169–222
71. J. Watson, *Behaviorism* (Transaction Publishers, Scotts Valley, 1997)
72. A. Ortony, T. Turner, What is basic about basic emotions. Psychol. Rev. **97**(3), 315–331 (1990)
73. W. Wundt, *Grundriss der Psychologie*, 7th rev edn. (Engelman, Liepzig, 1905), *[Fundamentals of Psychology]*
74. H. Schlosberg, Three dimensions of emotion. Psychol. Rev. **61**(2), 81–88 (1954)
75. C. Osgood, *The Measurement of Meaning* (University of Illinois Press, Champaign, 1975)
76. J. Davitz, *The Language of Emotion* (Academic Press, New York, 1969)
77. P. Lang, M. Bradley, B. Cuthbert, Emotion, motivation, and anxiety: brain mechanisms and psychophysiology. Biol. Psychiatry **44**(12), 1248–1263 (1998)
78. J. Panskepp, *Affective Neuroscience: The Foundations of Human and Animal Emotions* (Oxford University Press, London, 1998)
79. C. Breazeal, Emotion and sociable humanoid robots. Int. J. Hum.-Comput. Stud. **59**(1–2), 119–155 (2003)
80. J. Russell, A circumplex model of affect. J. Pers. Soc. Psychol. **39**(6), 1161–1178 (1980)
81. J. Russell, A. Mehrabian, Evidence for a three-factor theory of emotions* 1. J. Res. Pers. **11**(3), 273–294 (1977)

82. M. Arnold, *An Excitatory Theory of Emotion* (McGraw-Hill, New York, 1950)
83. N. Frijda, *The Emotions* (Cambridge University Press, Cambridge, 1986)
84. A. Ortony, G. Clore, A. Collins, *The Cognitive Structure of Emotions* (Cambridge University Press, Cambridge, 1990)
85. K. Scherer, P. Ekman, *Approaches to Emotions* (Lawrence Erlbaum Associates Publishers, Hillsdale, 1984)
86. C. Lisetti, P. Gmytrasiewicz, Can a rational agent afford to be affectless? A formal approach. Appl. Artif. Intell. **16**, 1–33 (2002)
87. K. Scherer, A. Schorr, T. Johnstone, *Appraisal Processes in Emotion: Theory, Methods, Research* (Oxford University Press, Oxford, 2001)
88. A. Egges, S. Kshirsagar, N. Magnenat-Thalmann, A model for personality and emotion simulation, in *Knowledge-Based Intelligent Information and Engineering Systems* (Springer, Berlin, 2003), pp. 453–461
89. J. Posner, J. Russell, B. Peterson, The circumplex model of affect: an integrative approach to affective neuroscience, cognitive development, and psychopathology. Dev. Psychopathol. **17**(3), 715–734 (2005)
90. F. Nasoz, K. Alvarez, C. Lisetti, N. Finkelstein, Emotion recognition from physiological signals for presence technologies international journal of cognition. Int. J. Cognit. Technology & Work **6**(1), 4–14 (2003)
91. R. Picard, *Affective Computing* (MIT Press, Cambridge, 2000)
92. R. Picard, E. Vyzas, J. Healey, Toward machine emotional intelligence: analysis of affective physiological state. IEEE Trans. Pattern Anal. Mach. Intell. **23**(10), 1175–1191 (2001)
93. J. Kim, E. André, Emotion recognition based on physiological changes in music listening. IEEE Trans. Pattern Anal. Mach. Intell. **30**(12), 2067–2083 (2008)
94. C. Katsis, N. Katertsidis, D. Fotiadis, An integrated system based on physiological signals for the assessment of affective states in patients with anxiety disorders. Biomed. Signal Process. Control **6**(3), 261–268 (2010)
95. P. Ekman, R. Levenson, W. Friesen, Autonomic nervous system activity distinguishes among emotions. Science **221**(4616), 1208–1210 (1983)
96. R. Levenson, Autonomic nervous system differences among emotions. Psychol. Sci. **3**(1), 23 (1992)
97. J. Saul, Beat-to-beat variations of heart rate reflect modulation of cardiac autonomic outflow. Physiology **5**(1), 32 (1990)
98. U. Rajendra Acharya, K. Paul Joseph, N. Kannathal, C. Lim, J. Suri, Heart rate variability: a review. Med. Biol. Eng. Comput. **44**(12), 1031–1051 (2006)
99. F. Atyabi, M. Livari, K. Kaviani, M. Tabar, Two statistical methods for resolving healthy individuals and those with congestive heart failure based on extended self-similarity and a recursive method. J. Biol. Phys. **32**(6), 489–495 (2006)
100. L. Glass, Synchronization and rhythmic processes in physiology. Nature **410**(6825), 277–284 (2001)
101. C. Poon, C. Merrill, Decrease of cardiac chaos in congestive heart failure. Nature **389**(6650), 492–495 (1997)
102. M. Rosenstein, J. Collins, C. De Luca, A practical method for calculating largest Lyapunov exponents from small data sets. Physica D **65**(1–2), 117–134 (1993)
103. M. Kobayashi, T. Musha, $1/f$ fluctuation of heartbeat period. IEEE Trans. Biomed. Eng. **6**, 456–457 (2007)
104. S. Pincus, Approximate entropy as a measure of system complexity. Proc. Natl. Acad. Sci. USA **88**(6), 2297 (1991)
105. C. Peng, S. Havlin, J. Hausdorff, J. Mietus, H. Stanley, A. Goldberger, Fractal mechanisms and heart rate dynamics*: long-range correlations and their breakdown with disease. J. Electrocardiol. **28**, 59–65 (1995)
106. J. Eckmann, S. Kamphorst, D. Ruelle, Recurrence plots of dynamical systems. Europhys. Lett. **4**, 973 (1987)

107. N. Marwan, N. Wessel, U. Meyerfeldt, A. Schirdewan, J. Kurths, Recurrence-plot-based measures of complexity and their application to heart-rate-variability data. Phys. Rev. E **66**(2), 26702 (2002)
108. J. Richman, J. Moorman, Physiological time-series analysis using approximate entropy and sample entropy. Am. J. Physiol., Heart Circ. Physiol. **278**(6), H2039 (2000)
109. I. Hagerman, M. Berglund, M. Lorin, J. Nowak, C. Sylvén, Chaos-related deterministic regulation of heart rate variability in time-and frequency domains: effects of autonomic blockade and exercise. Cardiovasc. Res. **31**(3), 410 (1996)
110. P. Venables, M. Christie, Electrodermal activity, in *Techniques in Psychophysiology* (1980), pp. 3–67
111. W. Winton, L. Putnam, R. Krauss, Facial and autonomic manifestations of the dimensional structure of emotion* 1. J. Exp. Soc. Psychol. **20**(3), 195–216 (1984)
112. P. Lang, M. Greenwald, M. Bradley, A. Hamm, Looking at pictures: affective, facial, visceral, and behavioral reactions. Psychophysiology **30**(3), 261–273 (1993)
113. H. McCurdy, Consciousness and the galvanometer. Psychol. Rev. **57**(6), 322–327 (1950)
114. M. Bradley, P. Lang, Affective reactions to acoustic stimuli. Psychophysiology **37**(2), 204–215 (2000)
115. P. Gomez, B. Danuser, Affective and physiological responses to environmental noises and music. Int. J. Psychophysiol. **53**(2), 91–103 (2004)
116. I. Christie, B. Friedman, Autonomic specificity of discrete emotion and dimensions of affective space: a multivariate approach. Int. J. Psychophysiol. **51**(2), 143–153 (2004)
117. M.P. Tarvainen, A.S. Koistinen, M. Valkonen-Korhonen, J. Partanen, P.A. Karjalainen, Analysis of galvanic skin responses with principal components and clustering techniques. IEEE Trans. Biomed. Eng. **48**(10), 1071–1079 (2001)
118. G. Lohse, E. Johnson, A comparison of two process tracing methods for choice tasks, in *System Sciences, 1996, Proceedings of the Twenty-Ninth Hawaii International Conference on*, vol. 4 (IEEE Press, New York, 2002), pp. 86–97
119. J. Andreassi, *Psychophysiology Human Behavior and Physiological Response* (Lawrence Erlbaum Associates Publishers, New York, 2006)
120. S. Christianson, E. Loftus, H. Hoffman, G. Loftus, Eye fixations and memory for emotional events. J. Exp. Psychol. Learn. Mem. Cogn. **17**(4), 693 (1991)
121. M. Bradley, D. Sabatinelli, P. Lang, J. Fitzsimmons, W. King, P. Desai, Activation of the visual cortex in motivated attention. Behav. Neurosci. **117**(2), 369 (2003)
122. M. Calvo, P. Lang, Gaze patterns when looking at emotional pictures: motivationally biased attention. Motiv. Emot. **28**(3), 221–243 (2004)
123. T. Partala, V. Surakka, Pupil size variation as an indication of affective processing. Int. J. Hum.-Comput. Stud. **59**(1–2), 185–198 (2003)
124. J. Beatty, B. Lucero-Wagoner, *The Pupillary System* (Cambridge University Press, Cambridge, 2000)
125. I. Loewenfeld, Comment on Hess' findings. Surv. Ophthalmol. **11**, 293–294 (1966)
126. E. Hess, Pupillometrics: a method of studying mental, emotional and sensory processes, in *Handbook of Psychophysiology* (1972), pp. 491–531
127. M. Janisse, Pupil size, affect and exposure frequency. Soc. Behav. Pers. **2**(2), 125–146 (1974)
128. E. Hess, S. Petrovich, Pupillary behavior in communication, in *Nonverbal Behavior and Communication* (Erlbaum, Hillsdale, 1987), pp. 327–348
129. A. Angelone, N. Coulter, Respiratory sinus arrhythmia: a frequency dependent phenomenon. J. Appl. Physiol. **19**(3), 479 (1964)
130. J. Hirsch, B. Bishop, Respiratory sinus arrhythmia in humans: how breathing pattern modulates heart rate. Am. J. Physiol., Heart Circ. Physiol. **241**(4), H620 (1981)
131. L. Bernardi, F. Salvucci et al., Evidence for an intrinsic mechanism regulating heart rate variability in the transplanted and the intact heart during submaximal dynamic exercise? Cardiovasc. Res. **24**(12), 969 (1990)
132. A. Guyton, J. Hall, *Textbook of Medical Physiology* (Saunders, London, 1981)

133. D. Jewett, Activity of single efferent fibres in the cervical vagus nerve of the dog, with special reference to possible cardio-inhibitory fibres. J. Physiol. **175**(3), 321 (1964)
134. E. Toledo, M. Rosenblum, C. Schäfer, J. Kurths, S. Akselrod, Quantification of cardiorespiratory synchronization in normal and heart transplant subjects, in *Int. Symp. on Nonlinear Theory and Applications*, vol. 1 (1998), pp. 171–174
135. N. Koshiya, J. Smith et al., Neuronal pacemaker for breathing visualized in vitro. Nature **400**(6742), 360–363 (1999)
136. H. Seidel et al., Analyzing entrainment of heartbeat and respiration with surrogates. IEEE Eng. Med. Biol. Mag. **17**(6), 54–57 (1998)
137. P. Grassberger, I. Procaccia, Measuring the strangeness of strange attractors. Physica D **9**(1–2), 189–208 (1983)
138. G. Wu, N. Arzeno, L. Shen, D. Tang, D. Zheng, N. Zhao, D. Eckberg, C. Poon, Chaotic signatures of heart rate variability and its power spectrum in health, aging and heart failure. PLoS ONE **4**(2), e4323 (2009)
139. L. Glass, M. Mackey, *From Clocks to Chaos: The Rhythms of Life* (Princeton University Press, Princeton, 1988)
140. C. Schafer, M. Rosenblum, J. Kurths, H. Abel, Heartbeat synchronized with ventilation. Nature **392**(6673), 239 (1998)
141. E. Toledo, S. Akselrod, I. Pinhas, D. Aravot, Does synchronization reflect a true interaction in the cardiorespiratory system? Med. Eng. Phys. **24**(1), 45–52 (2002)
142. M. Prokhorov, V. Ponomarenko, V. Gridnev, M. Bodrov, A. Bespyatov, Synchronization between main rhythmic processes in the human cardiovascular system. Phys. Rev. E **68**(4), 041913 (2003)
143. D. Von Bonin, M. Frühwirth, P. Heuser, M. Moser, Effects of speech therapy with poetry on heart rate variability and well-being. Forsch. Komplement.med. Klass. Nat.heilkd. (Gedruck. Ausg.) **8**(3), 144 (2001)
144. D. Cysarz, D. von Bonin, H. Lackner, P. Heusser, M. Moser, H. Bettermann, Oscillations of heart rate and respiration synchronize during poetry recitation. Am. J. Physiol., Heart Circ. Physiol. **287**(2), H579 (2004)
145. D. Cysarz, A. Büssing, Cardiorespiratory synchronization during zen meditation. Eur. J. Appl. Physiol. **95**(1), 88–95 (2005)
146. L. Pecora, T. Carroll, Synchronization in chaotic systems. Phys. Rev. Lett. **64**(8), 821–824 (1990)
147. P. Tass, M. Rosenblum, J. Weule, J. Kurths, A. Pikovsky, J. Volkmann, A. Schnitzler, H. Freund, Detection of $n : m$ phase locking from noisy data: application to magnetoencephalography. Phys. Rev. Lett. **81**(15), 3291–3294 (1998)
148. F. Mormann, K. Lehnertz, P. David, Mean phase coherence as a measure for phase synchronization and its application to the EEG of epilepsy patients. Physica D **144**(3–4), 358–369 (2000)
149. R. Quiroga, A. Kraskov, T. Kreuz, P. Grassberger, Performance of different synchronization measures in real data: a case study on electroencephalographic signals. Phys. Rev. E **65**(4), 041903 (2002)
150. K. Oshima, C. Carmeli, M. Hasler, State change detection using multivariate synchronization measure from physiological signals. J. Signal Process. **10**(4), 223–226 (2006)
151. M. Rosenblum, A. Pikovsky, J. Kurths, Phase synchronization in noisy and chaotic oscillators, in *Stochastic Dynamics* (1997), pp. 232–244
152. C. Schafer, M. Rosenblum, H. Abel, J. Kurths, Synchronization in the human cardiorespiratory system. Phys. Rev. E **60**(1), 857 (1999)
153. A. Pikovsky, G. Osipov, M. Rosenblum, M. Zaks, J. Kurths, Attractor-repeller collision and eyelet intermittency at the transition to phase synchronization. Phys. Rev. Lett. **79**(1), 47–50 (1997)
154. J. Zhang, X. Yu, D. Xie, Effects of mental tasks on the cardiorespiratory synchronization. Respiratory Physiology & Neurobiology **170**(1), 91–95 (2010)

155. M. Fukumoto, K. Matsuo, Effects of musical tempo on multiple subjective impressions. Int. J. Biom. **2**(2), 124–133 (2010)
156. L. Bialoskorski, J. Westerink, E. Broek, Mood swings: an affective interactive art system, in *Intelligent Technologies for Interactive Entertainment*, vol. 8 (2009), pp. 181–186
157. P. Lang, M. Bradley, B. Cuthbert, International affective picture system IAPS: digitized photographs, instruction manual and affective ratings. Technical Report A-6, University of Florida, 2005
158. C. Lisetti, F. Nasoz, Using noninvasive wearable computers to recognize human emotions from physiological signals. EURASIP J. Appl. Signal Process. **2004**, 1672–1687 (2004)
159. J. Janssen, E. Van den Broek, J. Westerink, Personalized affective music player, in *Affective Computing and Intelligent Interaction and Workshops, 2009. ACII 2009. 3rd International Conference on* (IEEE Press, New York, 2009), pp. 1–6
160. J. Wagner, J. Kim, E. André, From physiological signals to emotions: implementing and comparing selected methods for feature extraction and classification, in *2005 IEEE International Conference on Multimedia and Expo* (IEEE Press, New York, 2005), pp. 940–943
161. E. Van den Broek, M. Schut, J. Westerink, K. Tuinenbreijer, Unobtrusive sensing of emotions (USE). J. Ambient Intell. Smart Environ. **1**(3), 287–299 (2009)
162. E. Van den Broek, J. Westerink, Considerations for emotion-aware consumer products. Appl. Ergon. **40**(6), 1055–1064 (2009)
163. Z. Zeng, M. Pantic, G. Roisman, T. Huang, A survey of affect recognition methods: audio, visual, and spontaneous expressions. IEEE Trans. Pattern Anal. Mach. Intell. **31**(1), 39–58 (2008)
164. K. Poels, S. Dewitte, How to capture the heart? Reviewing 20 years of emotion measurement in advertising. J. Advert. Res. **46**(1), 18 (2006)
165. E. Leon, G. Clarke, V. Callaghan, F. Sepulveda, A user-independent real-time emotion recognition system for software agents in domestic environments. Eng. Appl. Artif. Intell. **20**(3), 337–345 (2007)
166. G. Chanel, J. Kierkels, M. Soleymani, T. Pun, Short-term emotion assessment in a recall paradigm. Int. J. Hum.-Comput. Stud. **67**(8), 607–627 (2009)
167. J. Healey, Affect detection in the real world: recording and processing physiological signals, in *Affective Computing and Intelligent Interaction and Workshops, 2009. ACII 2009. 3rd International Conference on* (IEEE Press, New York, 2009), pp. 1–6
168. J. Healey, R. Picard, Detecting stress during real-world driving tasks using physiological sensors. IEEE Trans. Intell. Transp. Syst. **6**(2), 156–166 (2005)
169. P. Lang, M. Bradley, B. Cuthbert, International affective picture system (IAPS): technical manual and affective ratings. NIMH Center for the Study of Emotion and Attention, 1997
170. P. Lang, M. Greenwald, M. Bradley, A. Hamm, Looking at pictures: affective, facial, visceral, and behavioral reactions. Psychophysiology **30**(3), 261–273 (1993)
171. P. Lang et al., Behavioral treatment and bio-behavioral assessment: computer applications, in *Technology in Mental Health Care Delivery Systems* (1980), pp. 119–137
172. S. Grimm, C. Schmidt, F. Bermpohl, A. Heinzel, Y. Dahlem, M. Wyss, D. Hell, P. Boesiger, H. Boeker, G. Northoff, Segregated neural representation of distinct emotion dimensions in the prefrontal cortex–an fMRI study. NeuroImage **30**(1), 325–340 (2006)
173. A. Hariri, V. Mattay, A. Tessitore, F. Fera, D. Weinberger, Neocortical modulation of the amygdala response to fearful stimuli. Biol. Psychiatry **53**(6), 494–501 (2003)
174. M. Swangnetr, D.B. Kaber, Emotional state classification in patient–robot interaction using wavelet analysis and statistics-based feature selection. IEEE Trans. Syst. Man Cybern. **43**(1), 63–75 (2012)
175. C. Katsis, N. Katertsidis, G. Ganiatsas, D. Fotiadis, Toward emotion recognition in car-racing drivers: a biosignal processing approach. IEEE Trans. Syst. Man Cybern., Part A, Syst. Hum. **38**(3), 502–512 (2008)
176. A. Chakraborty, A. Konar, U. Chakraborty, A. Chatterjee, Emotion recognition from facial expressions and its control using fuzzy logic. IEEE Trans. Syst. Man Cybern., Part A, Syst. Hum. **39**(4), 726–743 (2009)

177. G. Chanel, C. Rebetez, M. Bétrancourt, T. Pun, Emotion assessment from physiological signals for adaptation of game difficulty. IEEE Trans. Syst. Man Cybern., Part A, Syst. Hum. **41**(6), 1052–1063 (2011)
178. C. Lisetti, F. Nasoz, Using noninvasive wearable computers to recognize human emotions from physiological signals. EURASIP J. Appl. Signal Process. **2004**, 1672–1687 (2004)
179. A. Haag, S. Goronzy, P. Schaich, J. Williams, Emotion recognition using bio-sensors: first steps towards an automatic system, in *Affective Dialogue Systems* (2004), pp. 36–48
180. K. Kim, S. Bang, S. Kim, Emotion recognition system using short-term monitoring of physiological signals. Med. Biol. Eng. Comput. **42**(3), 419–427 (2004)
181. S. Yoo, C. Lee, Y. Park, N. Kim, B. Lee, K. Jeong, Neural network based emotion estimation using heart rate variability and skin resistance, in *Advances in Natural Computation* (2005), pp. 818–824
182. A. Choi, W. Woo, Physiological sensing and feature extraction for emotion recognition by exploiting acupuncture spots, in *Affective Computing and Intelligent Interaction* (2005), pp. 590–597
183. L. Li, J. Chen, Emotion recognition using physiological signals, in *Advances in Artificial Reality and Tele-Existence* (2006), pp. 437–446
184. P. Rani, C. Liu, N. Sarkar, E. Vanman, An empirical study of machine learning techniques for affect recognition in human–robot interaction. PAA Pattern Anal. Appl. **9**(1), 58–69 (2006)
185. P. Rainville, A. Bechara, N. Naqvi, A. Damasio, Basic emotions are associated with distinct patterns of cardiorespiratory activity. Int. J. Psychophysiol. **61**(1), 5–18 (2006)
186. J. Zhai, A. Barreto, Stress detection in computer users based on digital signal processing of noninvasive physiological variables, in *28th Annual International Conference of the IEEE Engineering in Medicine and Biology Society* (2006), pp. 1355–1358
187. C. Liu, K. Conn, N. Sarkar, W. Stone, Physiology-based affect recognition for computer-assisted intervention of children with autism spectrum disorder. Int. J. Hum.-Comput. Stud. **66**(9), 662–677 (2008)
188. G. Yannakakis, J. Hallam, Entertainment modeling through physiology in physical play. Int. J. Hum.-Comput. Stud. **66**(10), 741–755 (2008)
189. S. Johnson, J. Gruber, L. Eisner, Emotion and bipolar disorder, in *Emotion and Psychopathology: Bridging Affective and Clinical Science*, ed. by J. Rottenberg, S.L. Jonathan (Am. Psychol. Assoc., Washington, 2007)
190. L. Wang, K. LaBar, G. McCarthy et al., Mood alters amygdala activation to sad distractors during an attentional task. Biol. Psychiatry **60**(10), 1139–1146 (2006)
191. D. Radaelli, S. Poletti, S. Dallaspezia, C. Colombo, E. Smeraldi, F. Benedetti, Neural responses to emotional stimuli in comorbid borderline personality disorder and bipolar depression. Psychiatry Res. Neuroimaging **203**(1), 61–66 (2012)
192. R. Kessler, K. McGonagle, S. Zhao, C. Nelson, M. Hughes, S. Eshleman, H. Wittchen, K. Kendler, Lifetime and 12-month prevalence of DSM-III-R psychiatric disorders in the united states: results from the national comorbidity survey. Arch. Gen. Psychiatry **51**(1), 8 (1994)
193. H. Wittchen, F. Jacobi, Size and burden of mental disorders in Europe—a critical review and appraisal of 27 studies. European Neuropsychopharmacology **15**(4), 357–376 (2005)
194. S. Pini, V. de Queiroz, D. Pagnin, L. Pezawas, J. Angst, G. Cassano, H. Wittchen, Prevalence and burden of bipolar disorders in European countries. European Neuropsychopharmacology **15**(4), 425–434 (2005)
195. E. Vieta, M. Reinares, A. Rosa, Staging bipolar disorder. Neurotox. Res. **19**(2), 279–285 (2011)
196. A. Andreazza, M. Kauer-Sant'Anna, B. Frey, D. Bond, F. Kapczinski, L. Young, L. Yatham, Oxidative stress markers in bipolar disorder: a meta-analysis. J. Affective Disorders **111**(2), 135–144 (2008)
197. M. Phillips, E. Vieta, Identifying functional neuroimaging biomarkers of bipolar disorder: toward DSM-V. Schizophr. Bull. **33**(4), 893–904 (2007)

198. H. Stampfer, The relationship between psychiatric illness and the circadian pattern of heart rate. Australasian Psychiatry **32**(2), 187–198 (1998)
199. G. Iverson, H. Stampfer, M. Gaetz, Reliability of circadian heart pattern analysis in psychiatry. Psychiatr. Q. **73**(3), 195–203 (2002)
200. G. Iverson, M. Gaetz, E. Rzempoluck, P. McLean, W. Linden, R. Remick, A new potential marker for abnormal cardiac physiology in depression. J. Behav. Med. **28**(6), 507–511 (2005)
201. J. Taillard, P. Sanchez, P. Lemoine, J. Mouret, Heart rate orcadian rhythm as a biological marker of desynchronization in major depression: a methodological and preliminary report. Chronobiol. Int. **7**(4), 305–316 (1990)
202. J. Taillard, P. Lemoine, P. Boule, M. Drogue, J. Mouret, Sleep and heart rate circadian rhythm in depression: the necessity to separate. Chronobiol. Int. **10**(1), 63–72 (1993)
203. R. Carney, K. Freedland, M. Rich, A. Jaffe, Depression as a risk factor for cardiac events in established coronary heart disease: a review of possible mechanisms. Annals Behav. Med. **17**(2), 142–149 (1995)
204. A. Glassman, Depression, cardiac death, and the central nervous system. Neuropsychobiology **37**(2), 80–83 (1998)
205. L. Watkins, J. Blumenthal, R. Carney, Association of anxiety with reduced baroreflex cardiac control in patients after acute myocardial infarction. Am. Heart J. **143**(3), 460–466 (2002)
206. Special issues on nonlinearity on heart rate. Chaos **19** (2009)
207. A. Goldberger, C. Peng, L. Lipsitz, What is physiologic complexity and how does it change with aging and disease? Neurobiol. Aging **23**(1), 23–26 (2002)
208. M. Tulppo, A. Kiviniemi, A. Hautala, M. Kallio, T. Seppanen, T. Makikallio, H. Huikuri, Physiological background of the loss of fractal heart rate dynamics. Circulation **112**(3), 314 (2005)
209. J. Skinner, A. Goldberger, G. Mayer-Kress, R. Ideker, Chaos in the heart: implications for clinical cardiology. Nat. Biotechnol. **8**(11), 1018–1024 (1990)
210. G. Sugihara, W. Allan, D. Sobel, K. Allan, Nonlinear control of heart rate variability in human infants. Proc. Natl. Acad. Sci. USA **93**(6), 2608 (1996)
211. S. Leistedt, P. Linkowski, J. Lanquart, J. Mietus, R. Davis, A. Goldberger, M. Costa, Decreased neuroautonomic complexity in men during an acute major depressive episode: analysis of heart rate dynamics. Transl. Psychiatry **1**(7), e27 (2011)
212. R. Barbieri, E. Brown, Analysis of heartbeat dynamics by point process adaptive filtering. IEEE Trans. Biomed. Eng. **53**(1), 4–12 (2006)
213. Z. Chen, E. Brown, R. Barbieri, Assessment of autonomic control and respiratory sinus arrhythmia using point process models of human heart beat dynamics. IEEE Trans. Biomed. Eng. **56**(7), 1791–1802 (2009)
214. Z. Chen, E. Brown, R. Barbieri, Characterizing nonlinear heartbeat dynamics within a point process framework. IEEE Trans. Biomed. Eng. **57**(6), 1335–1347 (2010)
215. Z. Chen, P. Purdon, G. Harrell, E. Pierce, J. Walsh, E. Brown, R. Barbieri, Dynamic assessment of baroreflex control of heart rate during induction of propofol anesthesia using a point process method. Ann. Biomed. Eng. **39**(1), 260–276 (2011)
216. K. Kroenke, R. Spitzer, J. Williams, The PHQ-9. Journal of General Internal Medicine **16**(9), 606–613 (2001)
217. K. Gratz, M. Rosenthal, M. Tull, C. Lejuez, J. Gunderson, An experimental investigation of emotion dysregulation in borderline personality disorder. J. Abnorm. Psychology **115**(4), 850 (2006)
218. M. Bauer, C. Vojta, B. Kinosian, L. Altshuler, H. Glick, The internal state scale: replication of its discriminating abilities in a multisite, public sector sample. Bipolar Disorders **2**(4), 340–346 (2000)
219. D. McNair, M. Lorr, L. Droppleman, *POMS: Profile Of Mood States* (Educational and Industrial Testing Service Publisher, San Diego, 1971)
220. A. Rush, M. Trivedi, H. Ibrahim, T. Carmody, B. Arnow, D. Klein et al., The 16-item quick inventory of depressive symptomatology (QIDS), clinician rating (QIDS-C), and self-report

(QIDS-SR): a psychometric evaluation in patients with chronic major depression. Biol. Psychiatry **54**(5), 573–583 (2003)
221. R. Young, J. Biggs, V. Ziegler, D. Meyer, A rating scale for mania: reliability, validity and sensitivity. Br. J. Psychiatry **133**(5), 429–435 (1978)
222. L. Conti, *Repertorio delle Scale di Valutazione in Psichiatria* (SEE, Florence, 1999)
223. M. Farné, A. Sebellico, D. Gnugnoli, A. Corallo, *Profile of Mood States* (Giunti OS, Florence, 1991)
224. A. Mehrabian, E. O'Reilly, Analysis of personality measures in terms of basic dimensions of temperament. J. Pers. Soc. Psychol. **38**(3), 492 (1980)
225. D. De Rossi, F. Carpi, F. Lorussi, A. Mazzoldi, R. Paradiso, E. Scilingo, A. Tognetti, Electroactive fabrics and wearable biomonitoring devices. AUTEX Res. J. **3**(4), 180–185 (2003)
226. V. Pollak, Computation of the impedance characteristic of metal electrodes for biological investigations. Med. Biol. Eng. Comput. **12**(4), 460–464 (1974)
227. G. Heiman, *Research Methods in Psychology* (Houghton Mifflin, Boston, 1995)
228. B. Onaral, H. Schwan, Linear and nonlinear properties of platinum electrode polarisation. Part 1: frequency dependence at very low frequencies. Med. Biol. Eng. Comput. **20**(3), 299–306 (1982)
229. L. Freedman, A. Scerbo, M. Dawson, A. Raine, W. McClure, P. Venables, The relationship of sweat gland count to electrodermal activity. Psychophysiology **31**(2), 196–200 (1994)
230. L. Geddes, Historical evolution of circuit models for the electrode-electrolyte interface. Ann. Biomed. Eng. **25**(1), 1–14 (1997)
231. W. Chen, M. Er, S. Wu, Illumination compensation and normalization for robust face recognition using discrete cosine transform in logarithm domain. IEEE Trans. Syst. Man Cybern., Part B, Cybern. **36**(2), 458–466 (2006)
232. E. Land, J. McCann, Lightness and retinex theory. J. Opt. Soc. Am. **61**(1), 1–11 (1971)
233. A. Lanatà, E. Scilingo, E. Nardini, G. Loriga, R. Paradiso, D. De-Rossi, Comparative evaluation of susceptibility to motion artifact in different wearable systems for monitoring respiratory rate. IEEE Trans. Inf. Technol. Biomed. **14**(2), 378–386 (2010)
234. A. Jain, R. Mao, Statistical pattern recognition: a review. IEEE Trans. Pattern Anal. Mach. Intell. **22**(1), 4–37 (2000)
235. J. Webster et al., *Medical Instrumentation: Application and Design* (Wiley, New York, 1998)
236. J. Bailey, A. Berson, A. Garson Jr., L. Horan, P. Macfarlane, D. Mortara, C. Zywietz et al., Recommendations for standardization and specifications in automated electrocardiography: bandwidth and digital signal processing. Circulation **81**(2), 730 (1990)
237. B. Kohler, C. Hennig, R. Orglmeister, The principal of software QRS detection. IEEE Eng. Med. Biol. Mag. **6**(1), 42–57 (2002)
238. J. Pan, W. Tompkins, A real-time QRS detection algorithm. IEEE Trans. Biomed. Eng. **BME-32**(3), 230–236 (1985)
239. N. Lippman, K. Stein, B. Lerman, Nonlinear predictive interpolation. A new method for the correction of ectopic beats for heart rate variability analysis. J. Electrocardiol. **26**, 14 (1993)
240. N. Lippman, K. Stein, B. Lerman, Comparison of methods for removal of ectopy in measurement of heart rate variability. Am. J. Physiol., Heart Circ. Physiol. **267**(1), H411 (1994)
241. G. Berntson et al., Heart rate variability: origins, methods, and interpretive caveats. Psychophysiology **34**(6), 623–648 (1997)
242. M. Tarvainen, P. Ranta-Aho, P. Karjalainen, An advanced detrending method with application to HRV analysis. IEEE Trans. Biomed. Eng. **49**(2), 172–175 (2002)
243. R. Berger, S. Akselrod, D. Gordon, R. Cohen, An efficient algorithm for spectral analysis of heart rate variability. IEEE Trans. Biomed. Eng. **9**, 900–904 (2007)
244. A. Ishchenko, P. Shev'ev, Automated complex for multiparameter analysis of the galvanic skin response signal. Biomed. Eng. **23**(3), 113–117 (1989)
245. M. Benedek, C. Kaernbach, Decomposition of skin conductance data by means of nonnegative deconvolution. Psychophysiology **47**(4), 647–658 (2010)
246. D. Levinson, R. Edelberg, Scoring criteria for response latency and habituation in electrodermal research: a critique. Psychophysiology **22**(4), 417–426 (1985)

247. M. Benedek, C. Kaernbach, A continuous measure of phasic electrodermal activity. J. Neurosci. Methods **190**(1), 80–91 (2010)
248. E. Garrett, The Bateman function revisited: a critical reevaluation of the quantitative expressions to characterize concentrations in the one compartment body model as a function of time with first-order invasion and first-order elimination. J. Pharmacokinet. Pharmacodyn. **22**(2), 103–128 (1994)
249. R. Schneider, A mathematical model of human skin conductance. Psychophysiology **24**(5), 610 (1987)
250. F. Gustafsson, Determining the initial states in forward-backward filtering. IEEE Trans. Signal Process. **44**(4), 988–992 (1996)
251. S. Mitra, *Digital Signal Processing. A Computer-Based Approach* (McGraw-Hill, New York, 2000)
252. C. Karenbach, Ledalab—a software package for the analysis of phasic electrodermal activity. Technical report, Allgemeine Psychologie, Institut für Psychologie, 2005
253. W. Boucsein, *Electrodermal Acitivity* (Springer, Berlin, 2012)
254. H. Akaike, Fitting autoregressive models for prediction. Ann. Inst. Stat. Math. **21**(1), 243–247 (1969)
255. A. Boardman, F. Schlindwein, A. Rocha, A. Leite, A study on the optimum order of autoregressive models for heart rate variability. Physiol. Meas. **23**, 325 (2002)
256. B. Sayers, Analysis of heart rate variability. Ergonomics **16**(1), 17 (1973)
257. M. Ursino, E. Magosso, Role of short-term cardiovascular regulation in heart period variability: a modeling study. Am. J. Physiol., Heart Circ. Physiol. **284**(4), H1479 (2003)
258. J. Saul, R. Berger, P. Albrecht, S. Stein, M. Chen, R. Cohen, Transfer function analysis of the circulation: unique insights into cardiovascular regulation. Am. J. Physiol., Heart Circ. Physiol. **261**(4), H1231–H1245 (1991)
259. S. Koelstra, A. Yazdani, M. Soleymani, C. Mühl, J. Lee, A. Nijholt, T. Pun, T. Ebrahimi, I. Patras, Single trial classification of EEG and peripheral physiological signals for recognition of emotions induced by music videos, in *Brain Informatics* (2010), pp. 89–100
260. J. Mendel, Tutorial on higher-order statistics (spectra) in signal processing and system theory: theoretical results and some applications. Proc. IEEE **79**, 278–305 (1991)
261. C. Nikias, *Higher-Order Spectral Analysis: A Nonlinear Signal Processing Framework* (Prentice Hall International, Englewood Cliffs, 1993)
262. D.R. Brillinger, M. Rosenblatt, P. Petropulu, Computation and interpretation of *k*th order spectra, in *Spectral Analysis of Time Series* (Wiley, New York, 1967), pp. 189–232
263. T.N. Chang, S. Sun, Blind detection of photomontage using higher order statistics. Paper presented at the IEEE International Symposium on Circuits and Systems (ISCAS) Vancouver, Canada, 2004
264. K. Chua, V. Chandran, U. Acharya, C. Lim, Cardiac state diagnosis using higher order spectra of heart rate variability. J. Med. Eng. Technol. **32**(2), 145–155 (2008)
265. A. Lanatá, G. Valenza, C. Mancuso, E. Scilingo, Robust multiple cardiac arrhythmia detection through bispectrum analysis. Expert Syst. Appl. **38**(6), 6798–6804 (2011)
266. S. Zhou, J. Gan, F. Sepulveda, Classifying mental tasks based on features of higher-order statistics from EEG signals in brain–computer interface. Inf. Sci. **178**(6), 1629–1640 (2008)
267. S. Akselrod, Components of heart rate variability: basic studies, in *Heart Rate Variability* (1995), pp. 147–163
268. A. Malliani, Association of heart rate variability components with physiological regulatory mechanisms, in *Heart Rate Variability* (1995), pp. 173–188
269. S. Malpas, Neural influences on cardiovascular variability: possibilities and pitfalls. Am. J. Physiol., Heart Circ. Physiol. **282**(1), H6 (2002)
270. D. Forsyth, J. Ponce, *Computer Vision: A Modern Approach* (Prentice Hall Professional Technical Reference, 2002)
271. N. Bennett, R. Burridge, N. Saito, A method to detect and characterize ellipses using the Hough transform. IEEE Trans. Pattern Anal. Mach. Intell. **21**(7), 652–657 (2002)

272. A. Fitzgibbon, M. Pilu, R. Fisher, Direct least square fitting of ellipses. IEEE Trans. Pattern Anal. Mach. Intell. **21**(5), 476–480 (2002)
273. E. Maini, Robust ellipse-specific fitting for real-time machine vision, in *Brain, Vision, and Artificial Intelligence* (2005), pp. 318–327
274. H. Kantz, T. Schreiber, R. Mackay, *Nonlinear Time Series Analysis*, vol. 2000 (Cambridge University Press, Cambridge, 1997)
275. F. Takens, Detecting strange attractors in turbulence, in *Dynamical Systems and Turbulence*, Warwick, 1980 (1981), pp. 366–381
276. N. Marwan, M. Carmen Romano, M. Thiel, J. Kurths, Recurrence plots for the analysis of complex systems. Phys. Rep. **438**(5–6), 237–329 (2007)
277. A. Monk, A. Compton, Rev. Mod. Phys. **11**(3–4), 173–179 (1939)
278. J. Eckmann, S. Kamphorst, D. Ruelle, Recurrence plots of dynamical systems. Europhys. Lett. **4**, 973 (1987)
279. S. Schinkel, O. Dimigen, N. Marwan, Selection of recurrence threshold for signal detection. Eur. Phys. J. Spec. Top. **164**(1), 45–53 (2008)
280. J. Zbilut, C. Webber Jr., Recurrence quantification analysis, in *Wiley Encyclopedia of Biomedical Engineering* (Wiley Online Library, 2006)
281. C. Peng, S. Havlin, H. Stanley, A. Goldberger, Quantification of scaling exponents and crossover phenomena in nonstationary heartbeat time series. Chaos **5**(1), 82 (1995)
282. D. Ruelle, Sensitive dependence on initial condition and turbulent behavior of dynamical systems. Ann. N.Y. Acad. Sci. **316**(1), 408–416 (1979)
283. M. Casdagli, Nonlinear prediction of chaotic time series. Physica D **35**(3), 335–356 (1989)
284. A. Ellner et al., Convergence rates and data requirements for Jacobian-based estimates of Lyapunov exponents from data. Phys. Lett. A **153**(6–7), 357–363 (1991)
285. J. Farmer, J. Sidorowich, Predicting chaotic time series. Phys. Rev. Lett. **59**(8), 845–848 (1987)
286. S. Sato, M. Sano, Y. Sawada et al., Practical methods of measuring the generalized dimension and the largest Lyapunov exponent in high dimensional chaotic systems. Prog. Theor. Phys. **77**(1), 1–5 (1987)
287. A. Wolf, J. Swift, H. Swinney, J. Vastano, Determining Lyapunov exponents from a time series. Physica D **16**(3), 285–317 (1985)
288. W. Liebert, H. Schuster, Proper choice of the time delay for the analysis of chaotic time series. Phys. Lett. A **142**(2–3), 107–111 (1989)
289. Y. Fusheng, H. Bo, T. Qingyu, Approximate entropy and its application in biosignal analysis, in *Nonlinear Biomedical Signal Processing* (2000), p. 72
290. D.E. Lake, J.S. Richman, M.P. Griffin, J.R. Moorman, Sample entropy analysis of neonatal heart rate variability. Am. J. Physiol., Regul. Integr. Comp. Physiol. **283**(3), R789–R797 (2002)
291. J.C. Schouten, F. Takens, C.M. van den Bleek, Estimation of the dimension of a noisy attractor. Phys. Rev. E **50**(3), 1851 (1994)
292. C. Liu, C. Liu, P. Shao, L. Li, X. Sun, X. Wang, F. Liu, Comparison of different threshold values r for approximate entropy: application to investigate the heart rate variability between heart failure and healthy control groups. Physiol. Meas. **32**(2), 167 (2011)
293. P. Castiglioni, M. Di Rienzo, How the threshold r influences approximate entropy analysis of heart-rate variability, in *Computers in Cardiology, 2008* (IEEE Press, New York, 2008), pp. 561–564
294. S. Lu, X. Chen, J.K. Kanters, I.C. Solomon, K.H. Chon, Automatic selection of the threshold value r for approximate entropy. IEEE Trans. Biomed. Eng. **55**(8), 1966 (2008)
295. K. Chon, C. Scully, S. Lu, Approximate entropy for all signals. IEEE Eng. Med. Biol. Mag. **28**(6), 18–23 (2009)
296. J. Kelso, *Dynamic Patterns: The Self-Organization of Brain and Behavior* (MIT Press, Cambridge, 1995)
297. D. Hoyer, B. Pompe, H. Herzel, U. Zwiener, Nonlinear coordination of cardiovascular autonomic control. IEEE Eng. Med. Biol. Mag. **17**(6), 17–21 (1998)

298. C. Herzog, N. Abolmaali, J. Balzer, S. Baunach, H. Ackermann, S. Dogan, M. Britten, T. Vogl, Heart-rate-adapted image reconstruction in multidetector-row cardiac CT: influence of physiological and technical prerequisite on image quality. Eur. Radiol. **12**(11), 2670–2678 (2002)
299. D. Bloomfield, A. Magnano, J. Bigger, H. Rivadeneira, M. Parides, R. Steinman, Comparison of spontaneous vs. metronome-guided breathing on assessment of vagal modulation using RR variability. Am. J. Physiol., Heart Circ. Physiol. **280**(3), H1145 (2001)
300. B. Boashash, Estimating and interpreting the instantaneous frequency of a signal. I. Fundamentals. Proc. IEEE **80**(4), 520–538 (1992)
301. I. Jolliffe, *Principal Component Analysis* (Wiley Online Library, 2005)
302. R. Kohavi, F. Provost, Glossary of terms. Mach. Learn. **30**(June), 271–274 (1998)
303. H. Scheffe, *The Analysis of Variance*, vol. 72 (Wiley-Interscience, New York, 1999)
304. R. Duda, P. Hart, D. Stork, *Pattern Classification* (Wiley, New York, 2001)
305. W. KinneBrock, *Neural Networks* (Oldenburg, München, 1992)
306. C. Cortes, V. Vapnik, Support vector machine. Mach. Learn. **20**(3), 273–297 (1995)
307. T.S. Furey, N. Cristianini, N. Duffy, D.W. Bednarski, M. Schummer, D. Haussler, Support vector machine classification and validation of cancer tissue samples using microarray expression data. Bioinformatics **16**(10), 906–914 (2000)
308. C.W. Gardiner et al., *Handbook of Stochastic Methods*, vol. 3 (Springer, Berlin, 1985)
309. C. Granger, R. Joyeux, An introduction to long-memory time series models and fractional differencing. J. Time Ser. Anal. **1**(1), 15–29 (1980)
310. J. Le Caillec, R. Garello, Nonlinear system identification using autoregressive quadratic models. Signal Process. **81**(2), 357–379 (2001)
311. C. Nikias, J. Mendel, Signal processing with higher-order spectra. IEEE Signal Process. Mag. **10**(3), 10–37 (1993)
312. C. Nikias, A. Petropulu, *Higher-Order Spectra Analysis: A Nonlinear Signal Processing Framework* (PTR Prentice Hall, Englewood Cliffs, 1993)
313. Z. Chen, P. Purdon, E. Brown, R. Barbieri, A differential autoregressive modeling approach within a point process framework for non-stationary heartbeat intervals analysis, in *Engineering in Medicine and Biology Society (EMBC), 2010 Annual International Conference of the IEEE* (IEEE Press, New York, 2010), pp. 3567–3570
314. S. Billings, Identification of nonlinear system—a survey. Proc. IEEE **127**, 272–285 (1980)
315. J. Mendel, Tutorial on higher-order statistics (spectra) in signal processing and system theory: theoretical results and some applications. Proc. IEEE **79**, 278–305 (1991)
316. C. Loader, *Local Regression and Likelihood* (Springer, Berlin, 1999)
317. R. Tibshirani, T. Hastie, Local likelihood estimation. J. Am. Stat. Assoc. **82**(398), 559–567 (1987)
318. E. Brown, R. Barbieri, U. Eden, L. Frank, Likelihood methods for neural spike train data analysis, in *Computational Neuroscience: A Comprehensive Approach* (2003), pp. 253–286
319. D. Westwick, R. Kearney, Explicit least-squares methods, in *Identification of Nonlinear Physiological Systems*, vol. 7 (Wiley, New York, 2003)
320. L. Citi, E. Brown, R. Barbieri, A real-time automated point process method for detection and correction of erroneous and ectopic heartbeats. IEEE Trans. Biomed. Eng. **59**, 2828–2837 (2012)
321. M. Akay, *Nonlinear Biomedical Signal Processing Vol. II: Dynamic Analysis and Modeling* (Wiley, New York, 2000)
322. J. Jo, A. Blasi, E. Valladares, R. Juarez, A. Baydur, M. Khoo, A nonlinear model of cardiac autonomic control in obstructive sleep apnea syndrome. Ann. Biomed. Eng. **35**(8), 1425–1443 (2007)
323. P. Koukoulas, N. Kalouptsidis, Nonlinear system identification using Gaussian inputs. IEEE Trans. Signal Process. **43**(8), 1831–1841 (1995)
324. C. Nikias, M. Raghuveer, Bispectrum estimation: a digital signal processing framework. Proc. IEEE **75**(7), 869–891 (1987)

325. J. Nichols, C. Olson, J. Michalowicz, F. Bucholtz, The bispectrum and bicoherence for quadratically nonlinear systems subject to non-Gaussian inputs. IEEE Trans. Signal Process. **57**(10), 3879–3890 (2009)
326. D. Brillinger, An introduction to polyspectra. Ann. Math. Stat. **36**(5), 1351–1374 (1965)
327. J. Caillec, R. Garello, Asymptotic bias and variance of conventional bispectrum estimates for 2-D signals. Multidimens. Syst. Signal Process. **16**(1), 49–84 (2005)
328. D. Brillinger, The identification of polynomial systems by means of higher order spectra* 1. J. Sound Vib. **12**(3), 301–313 (1970)
329. M. Priestley, *Spectral Analysis and Time Series* (Academic Press, San Diego, 1981)
330. H. Lilliefors, On the Kolmogorov–Smirnov test for normality with mean and variance unknown. J. Am. Stat. Assoc. **62**(318), 399–402 (1967)
331. W. Kruskal, W. Wallis, Use of ranks in one-criterion variance analysis. J. Am. Stat. Assoc. **47**(260), 583–621 (1952)
332. P. McKight, J. Najab, Kruskal–Wallis test, in *Corsini Encyclopedia of Psychology* (Wiley Online Library, 2010)
333. F. van der Heiden, R. Duin, D. de Ridder, D. Tax, *Classification, Parameter Estimation, State Estimation: An Engineering Approach Using MatLab* (Wiley, New York, 2004)
334. A. Schlogl, *Time Series Analysis—A Toolbox for the Use with Matlab* (2002)
335. M. Garcia-Gonzalez, M. Fernández-Chimeno, J. Ramos-Castro, Errors in the estimation of approximate entropy and other recurrence-plot-derived indices due to the finite resolution of RR time series. IEEE Trans. Biomed. Eng. **56**(2), 345–351 (2009)
336. L. Citi, E.N. Brown, R. Barbieri, A point process local likelihood algorithm for robust and automated heart beat detection and correction, in *Proceedings of Computing in Cardiology*, Hangzhou (2011)
337. A. Barnett, R. Wolff, A time-domain test for some types of nonlinearity. IEEE Trans. Signal Process. **53**(1), 26–33 (2005)
338. F. Wilcoxon, Individual comparisons by ranking methods. Biom. Bull. **1**(6), 80–83 (1945)
339. G. Valenza, L. Citi, A. Lanatà, E.P. Scilingo, R. Barbieri, A nonlinear heartbeat dynamics model approach for personalized emotion recognition. Paper presented at the Proceeding of the IEEE Engineering in Medicine and Biology International Conference, 2013
340. B. Scholkopf, A. Smola, R. Williamson, P. Bartlett, New support vector algorithms. Neural Comput. **12**(5), 1207–1245 (2000)
341. G. Stavig, J. Gibbons, Comparing the mean and the median as measures of centrality. Int. Stat. Rev. **45**(1), 63–70 (1977)
342. R. Stratonovich, *Topics in the Theory of Random Noise: General Theory of Random Processes, Nonlinear Transformations of Signals and Noise*, vol. 1 (Gordon & Breach, New York, 1967)
343. M. Kearns, D. Ron, Algorithmic stability and sanity-check bounds for leave-one-out cross-validation. Neural Comput. **11**(6), 1427–1453 (1999)
344. A.P. Association, *Diagnostic and Statistical Manual of Mental Disorders: DSM-IV-TR®* (American Psychiatric Association, Washington, 2000)
345. R. Kohavi, F. Provost, Glossary of terms. Mach. Learn. **30**, 271–274 (1998)
346. W. KinneBrock, *Neural Networks* (Oldenburg, München, 1992)
347. K. Scherer, Emotions are emergent processes: they require a dynamic computational architecture. Philos. Trans. R. Soc. Lond. B, Biol. Sci. **364**(1535), 3459 (2009)
348. N. Fragopanagos, J. Taylor, Emotion recognition in human–computer interaction. Neural Netw. **18**(4), 389–405 (2005)
349. R. Cowie, E. Douglas-Cowie, K. Karpouzis, G. Caridakis, M. Wallace, S. Kollias, Recognition of emotional states in natural human–computer interaction, in *Multimodal User Interfaces* (2008), pp. 119–153
350. D. Grandjean, D. Sander, K. Scherer, Conscious emotional experience emerges as a function of multilevel, appraisal-driven response synchronization. Conscious. Cogn. **17**(2), 484–495 (2008)

351. H. Bettermann, D. von Bonin, M. Fruhwirth, D. Cysarz, M. Moser, Effects of speech therapy with poetry on heart rate rhythmicity and cardiorespiratory coordination. Int. J. Cardiol. **84**(1), 77–88 (2002)
352. C. Hamann, R. Bartsch, A. Schumann, T. Penzel, S. Havlin, J. Kantelhardt, Automated synchrogram analysis applied to heartbeat and reconstructed respiration. Chaos **19**, 015106 (2009)
353. S. Waldstein, W. Kop, L. Schmidt, A. Haufler, D. Krantz, N. Fox, Frontal electrocortical and cardiovascular reactivity during happiness and anger. Biol. Psychol. **55**(1), 3–23 (2000)
354. J. Saul, R. Cohen, Respiratory sinus arrhythmia, in *Vagal Control of the Heart: Experimental Basis and Clinical Implications* (1994), pp. 511–536
355. S. Kodituwakku, S. Lazar, P. Indic, E. Brown, R. Barbieri, Point process time-frequency analysis of respiratory sinus arrhythmia under altered respiration dynamics, in *Proc. of EMBC 2010, IEEE* (IEEE Press, New York, 2010), pp. 1622–1625
356. J. Jamšek, A. Stefanovska, P. McClintock, Nonlinear cardio-respiratory interactions revealed by time-phase bispectral analysis. Phys. Med. Biol. **49**, 4407 (2004)
357. J. Jeong, M. Joung, S. Kim, Quantification of emotion by nonlinear analysis of the chaotic dynamics of electroencephalograms during perception of $1/f$ music. Biol. Cybern. **78**(3), 217–225 (1998)
358. Y. Kuznetsov, P. Landa, A. Ol'Khovoi, S. Perminov, Relationship between the amplitude threshold of synchronization and the entropy in stochastic self-excited systems. Sov. Phys. Dokl. **30**, 221 (1985)
359. L. Kocarev, A. Shang, L. Chua, Transition in dynamical regime by driving: a method of control and synchronization of chaos. Electronics Research, Laboratory, College of Engineering, University of California, 1993
360. A. Isen, B. Means, The influence of positive affect on decision-making strategy. Social Cogn. **2**(1), 18–31 (1983)
361. J. Zhou, Feedback svalence, feedback style, task autonomy, and achievement orientation: interactive effects on creative performance. J. Appl. Psychol. **83**(2), 261 (1998)
362. A. Gaggioli, G. Pioggia, G. Tartarisco, G. Baldus, D. Corda, P. Cipresso et al., A mobile data collection platform for mental health research. Pers. Ubiquitous Comput. **17**(2), 241–251 (2013)
363. S. Pavlopoulos, E. Kyriacou, A. Berler, S. Dembeyiotis, D. Koutsouris, A novel emergency telemedicine system based on wireless communication technology-ambulance. IEEE Trans. Inf. Technol. Biomed. **2**(4), 261–267 (1998)
364. E. Jovanov, A. O'Donnell Lords, D. Raskovic, P. Cox, R. Adhami, F. Andrasik, Stress monitoring using a distributed wireless intelligent sensor system. IEEE Eng. Med. Biol. Mag. **22**(3), 49–55 (2003)
365. M. Orini, G. Valenza, L. Citi, R. Barbieri, Tetravariate point-process model for the continuous characterization of cardiovascular-respiratory dynamics during passive postural changes. Paper presented at the International Conference on Computing in Cardiology, 2012

Index

G. Valenza, E.P. Scilingo, *Autonomic Nervous System Dynamics for Mood and Emotional-State Recognition*, Series in BioEngineering,
DOI 10.1007/978-3-319-02639-8, © Springer International Publishing Switzerland 2014